Dynamics and Stability of Spinning Membranes

Thesis by

Mélanie Delapierre

In Partial Fulfillment of the Requirements

for the Degree of

Doctor of Philosophy

California Institute of Technology

Pasadena, California

2017

(Defended May 9, 2017)

To my family.

Acknowledgments

The work presented herein could not have been done without the help of many people that I would like to thank here. First and foremost I would like to thank my adviser, Prof. Pellegrino, for his support, and advice during those past four years. I thank you for your guidance, encouragement, enthusiasm, availability and the great work environment that you provide to the group. I would also like to thank the members of my committee: Prof. Daraio, Prof. Kochmann, and Prof. Meiron.

I would like to acknowledge my past and present colleagues from the Space Structures Laboratory. In particular I would like to thank you for the very insightful and useful comments you gave me during group meetings and each time I had to prepare a public presentation. I thank Manan Arya, Miguel Bessa, Stephen Bongiorno, Federico Bosi, Serena Ferraro, Terry Gdoutos, Ashish Goel, Christophe Leclerc, Ignacio Maqueda Jiménez, Xin Ning, Keith Patterson, Fabien Royer, Maria Sakovsky, John Steeves, Thibaud Talon, Yuchen Wei, and Lee Wilson. I really enjoyed working with all of you.

I had the chance to collaborate with engineers, and professors and students from other research groups and I would like to thank them here. First, many thanks to Prof. John E. Sader, for the discussions we had on the analytical formulation of wrinkling of spinning membranes. I would also like to thank Stefan Haegeli Lohaus for his help with the experiments on nonlinear vibrations. I would also like to thank all the members of the AAReST team that I had the chance to work with, and in particular John Baker, Dr. Greg Davis, Dr. Yunjin Kim, Anthony Freeman, and Dr. Daniel Scharf from JPL. This project taught me a lot about practical aerospace engineering and team work. In addition, I had the chance to participate in the Space Solar Power Initiative at Caltech. I would like to thank everybody from Prof. Atwater and Prof. Hajimiri's research groups. You taught me most of what I know about applied physics and electrical engineering during your bi-weekly presentations.

I thank the staff at GALCIT, specifically Petros Arakelian, Joe Haggerty, Kathleen Jackson, Dimity Nelson, and Christine Ramirez for the support and constant smiles.

I would like to thank the financial support of the Northrop Grumman Corporation and the Keck Institute for Space Studies. In particular I would like to thank Michele Judd from KISS for her support and all the great Space related events that she has organized on campus.

I would like to thank my Caltech friends for the great time we had in California. Finally, I would like to thank my family. In particular, my grandparents Jacques and Marie-Paule that initiated me to science aux Trois Cheminées.

Abstract

Many future space missions require large structures subject to stringent shape accuracy requirements. Spinning membrane-like structures are a cost effective solution for these applications. However, any small deflection of a spinning structure, due to maneuvers or solar radiation pressure, leads to geometrically nonlinear effects on its stability and dynamics. Accurate experiments, simulation tools, and models are required to ensure that buckling and vibrations will not affect mission objectives.

We first focus on the influence of transverse uniform loads on the dynamics and stability of spinning isotropic uniform membranes. A transverse uniform load models the effect of a transverse light beam on flat membranes with small deflections. We present experimental measurements of the angular velocities at which various membranes become wrinkled, and of the wrinkling mode transitions that occur upon spin down. A theoretical formulation to predict the critical angular velocities and critical transverse loads is also presented. The transition between bending dominated and in-plane dominated behavior is identified, and the wrinkling modes are obtained. Next, deflected, non-buckled membranes are further analyzed. Axisymmetric nonlinear oscillations are studied analytically, and a reduced-order model is presented. This model predicts that the deflection of the membrane introduces a hardening behavior at low angular velocities and a softening behavior at high angular velocities. This model is validated through experiments and FEM simulations.

Then, we relax the assumption of uniform membranes loaded by transverse light beams. We present an Abaqus model of foldable membranes and show that for particular types of hinges and at high angular velocities, these structures behave like uniform membranes. Finally, we derive an FEM model for solar radiation pressure for quadrilateral surface elements and 3D problems and present its implementation in Abaqus. We show that this follower load introduces an unsymmetric stiffness matrix and that instabilities known as solarelastic flutter can develop. This new FEM capability enables equilibrium and frequency-based stability analyses for a wide range of spacecraft.

Contents

List of Figures

List of Tables

Chapter 1

Introduction

1.1 Motivation

Membranes are widely used for deployable lightweight space structures as they can be packaged tightly for launch. For example, Figures 1.1a and 1.1b respectively show IKAROS Solar Sail in its deployed and packaged configurations. The 20 m diameter sails is packaged into a 1.6 m $\times$ 0.8 m cylinder to fit into a launch vehicle. Due to the emergence of thinner material films, structural architectures and miniaturized

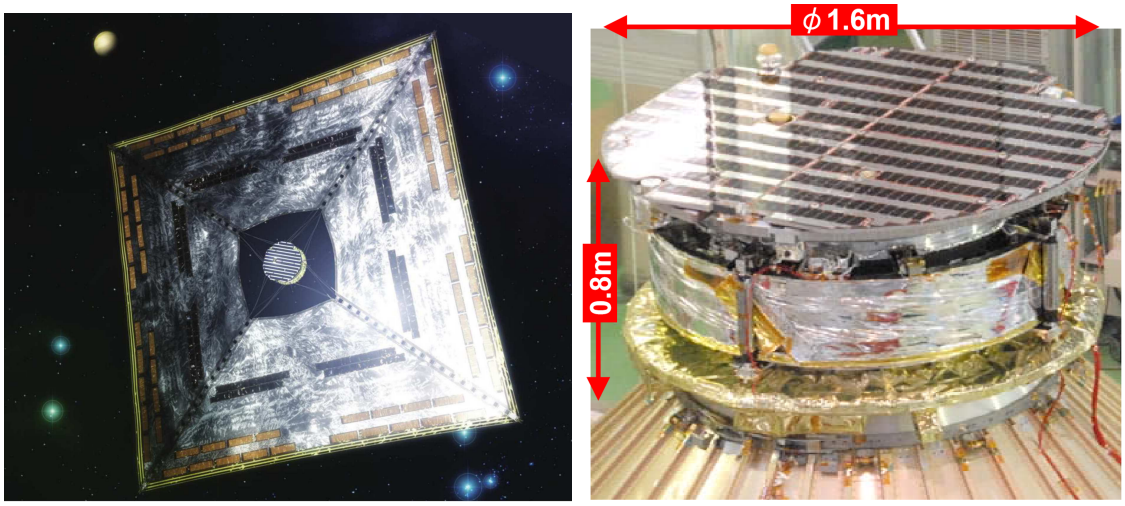

(a) IKAROS in its deployed configuration (20 m diam. 7.5 μm thick) (JAXA, 2010)

(b) IKAROS in its packaged configuration 1.6 m diam. 0.8 m height (Sawada et al., 2007)

Figure 1.1: Packaging of Membrane Structures.

electronics, membrane structures are becoming a new trend. For example, the Jet Propulsion Laboratory (Moussessian et al., 2011) has been developing membrane active phased array radar (see Figure 1.2a), opening the possibility for a new generation of large flexible antennas in space. Solar cells on large arrays such as the ones on the International Space Station (Figure 1.3) is another example of technology compatible with thin

structures. Finally, the Space Solar Power Initiative (SSPI) at Caltech is developing thin tiles that collect solar energy using photovoltaic cells, and beam it to Earth as radio frequency energy using patch antennas. Those tiles (Figure 1.2b) are very thin lightweight modular units attached to larger, flexible, and packageable modules.

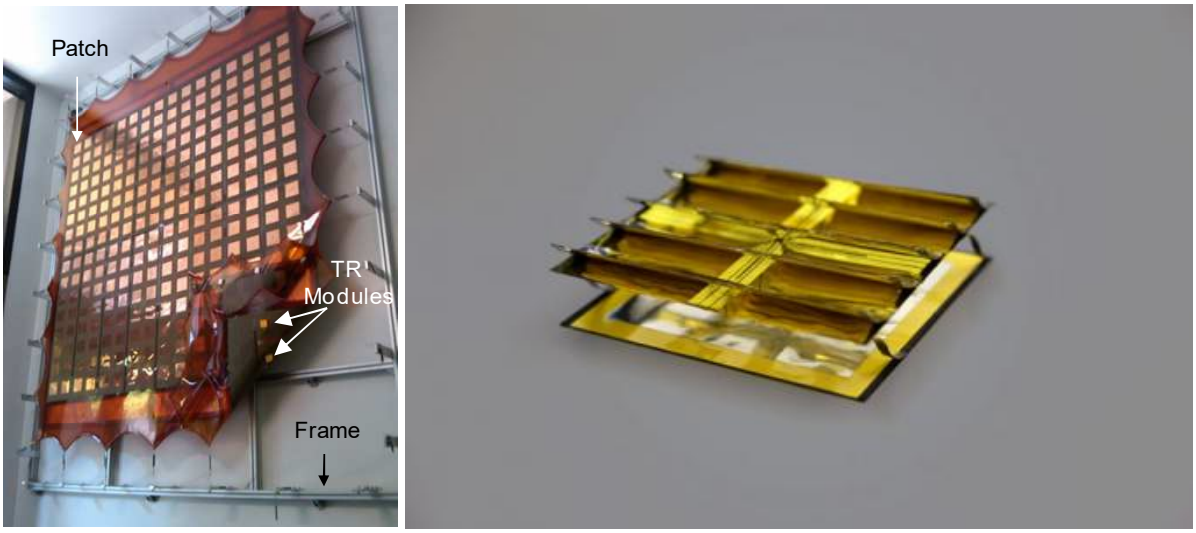

(a) 16x16 element active membrane array (Moussessian et al., 2011).

(b) SSPI tile mockup. A very light structure that integrates optical concentrators, solar cells and antennas (Caltech, 2015).

Figure 1.2: Advanced flexible technologies for space application.

Figure 1.3: Solar array wing on the International Space Station (NASA, 2006).

Other applications simply require a membrane with special surface properties. The James Webb Space Telescope includes tensioned reflective membranes forming a sunshield (Figure 1.4a) that protects the telescope from external sources of light and heat. This is a necessary condition to detect faint and very distant

objects. In addition, reflective membranes are widely considered for solar sailing. The principal of solar sails (or light sails or photon sails) is to use the radiation pressure exerted by sunlight on large mirrors as a propulsion system. Such a structure is illustrated in Figure 1.4b with the Sunjammer demonstrator led by the company L'Garde Inc. and NASA. Another application is space reflectors. The Russian Federal Space Agency has developed and tested the Znamya satellites (Figure 1.4c), a series of experimental orbital mirrors made to beam solar energy from space to some remote places of Russia. The project was abandoned after the failed deployment of the Znamya 2.5.

(a) Full-sized JWST sunshield post deployment test. Credit: Northrop Grumman (NASA, 2015).

(b) Sunjammer ground demonstrator (Johnson et al., 2010).

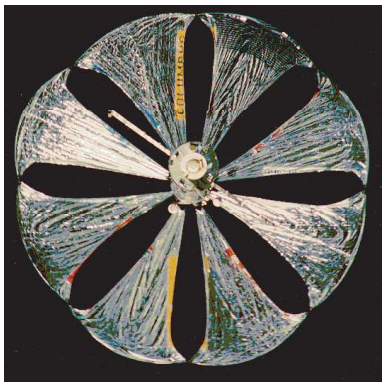

(c) Znamya concept (Melnikov and Koshelev, 1998).

Figure 1.4: Example of reflective membrane structure applications.

The low bending stiffness of membranes, which is advantageous for packaging, also requires them to be put into a state of prestress, after deployment, to stabilize their deployed shape. Pre-stressing can be done by applying edge forces through a set of deployable booms as in the ATK (Johnson et al., 2010) and Sunjammer (Figure 1.4b) Solar Sail concepts or the James Webb sunshield (Clampin, 2008). Nevertheless there is an

increasing interest in a lighter and potentially simpler approach, in which prestressing is achieved through the use of centrifugal action. This approach was recently demonstrated in the IKAROS solar sail (Sawada et al., 2007), shown in Figure 1.1a, during which, however, unexpected shape deviations were observed (Satou et al., 2015).

Several missions or mission concepts have used centrifugal force to prestress flexible structures. We already have mentioned the IKAROS and Znamya satellites but it is also a popular idea in the area of mesh reflectors. Kyser (1965) has studied a concept for an isotensional disk for space applications such as a rotating wing for re-entry deceleration. Later, the Furoshiki was introduced (Nakasuka et al., 2006). The Furoshiki concept (Figure 1.5b) is a large membrane or net in space extended by satellites that hold each corner. In addition, ESA advanced concept team (Gunnar and Gärdsback, 2009) has studied the concept of a large web in space. Another membrane example is Heliogyro (Figure 1.5a), a solar sailing mission that was first introduced by MacNeal (1967). It is made of flexible spinning blades that can be actuated and rotated for altitude control. The main advantage is the easy storage and deployment of the system. Other examples of spinning spacecraft formed and deployed using centrifugal forces are reported on the book by McInnes (1999) and Melnikov and Koshelev (1998). Figure 1.5c and Figure 1.5d show two other missions where the spinning structure is curved. The applications are a parabolic concentrator (Nakasuka et al., 2006) and large-aperture paraboloidal reflector low-frequency telescope, LOFT (Large low-frequency orbiting radio telescope) (Schuerch and Hedgepeth, 1968).

Many research projects have focused on the deployment of such structures in space. In the context of spin deployment of mesh structures we can refer to the previously introduced report (Gunnar and Gärdsback, 2009; Gärdsback and Tibert, 2009). When it comes to membrane structures there is extensive literature in the context of IKAROS that includes (Tatematsu et al., 2017; Mori et al., 2012; Sakamoto et al., 2011; Zhao et al., 2013; Yamazaki and Miyazaki, 2011). Although deployment is a key aspect to the success of a mission, in this thesis we focus on the less studied post deployment behavior of spinning membrane structures.

For many of the previously cited applications shape accuracy is a key requirement. For phased array antennas, for example, a flatness error of $\frac{\lambda}{30}$ (where λ is the wavelength) leads to a 5% loss in transmission in the main beam (for very large arrays). A flat shape also increases the propulsive action for solar sailing or the total absorption in photovoltaic membranes. Some of the disturbances that can alter the flatness of the structure post deployment include gravity gradient, maneuvers, thermal gradient and solar radiation pressure. In this thesis we focus on transverse translation maneuvers and solar radiation pressure.

Overall very flexible space structures are a recent promising development that necessitates new high fidelity models, as well as experimental methods and simulations techniques with the aim of understanding their dynamics and stability in space in order to ensure that they are able to provide the required performance.

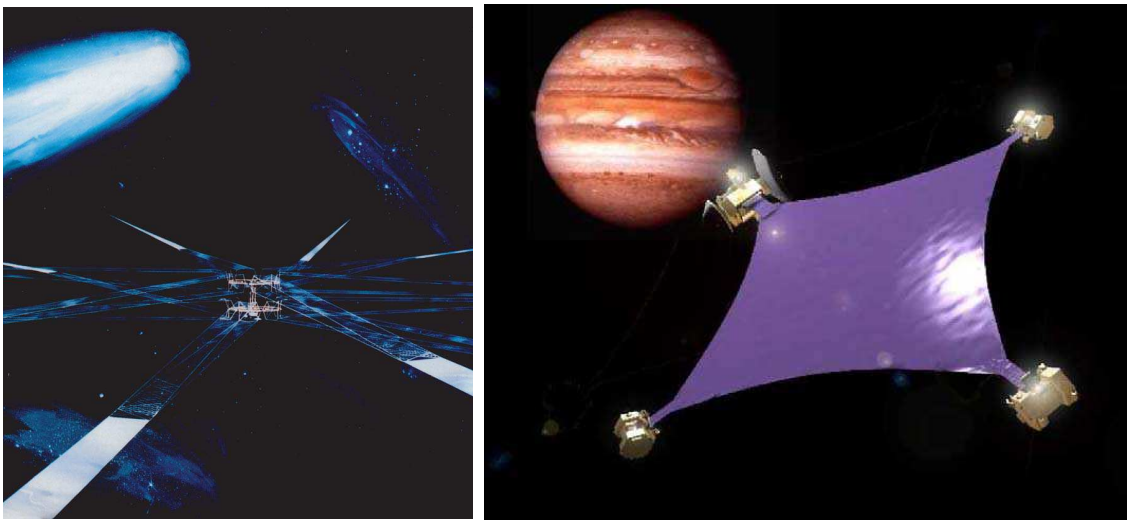

(a) Heliogyro concept (Wilkie et al., 2015). (b) Concept of Furoshiki Satellite (Nakasuka et al., 2006).

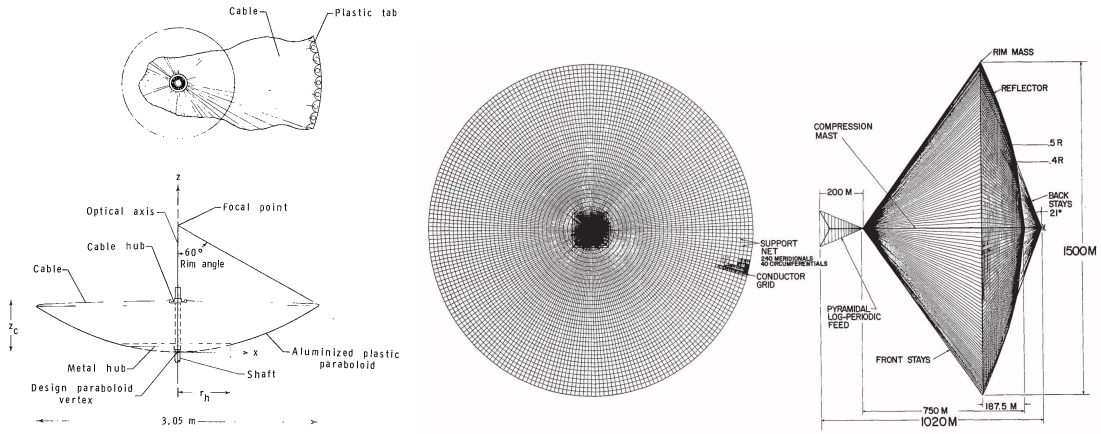

(c) Sketch of whirling-membrane solar concentrator (Jerke and Heuth, 1968). (d) The baseline design of the LOFT concept (Schuerch and Hedgepeth, 1968).

Figure 1.5: Existing mission concepts using spinning, flexible structures.

1.2 Goals and Outline

The first goal of this thesis is to understand how a uniform load, such as the load imposed by a transverse light beam and as approximated by gravity, affects the dynamics and stability of a spinning membrane. Two fundamental problems were analyzed. First, the wrinkling of spinning membranes under transverse uniform loads was studied. The objective was to determine the minimal angular velocity at which a flexible structure needs to be spun up in order to maintain a flat or near flat axisymmetric shape. Then, the influence of the axisymmetric, pre-buckled deflection on the membrane nonlinear dynamics was studied, focusing on axisymmetric resonance. For both cases we have approximated a spinning space structure using a thin, circular, clamped-free, isotropic, linear elastic annulus. An experimental setup was developed and will be

presented in Chapters 2 and 3. In this setup the sample spins horizontally in vacuum, with two degrees of freedom controlled at the hub: the rotation around the axis of revolution and the normal translation. Two different data acquisition systems have been used. Digital image correlation (DIC) measures the shape of the membrane while a scanning vibrometer acquires its vibration. Several analytical models based on the von Kármán plate equations were developed. Nonlinear static and dynamic simulations in Abaqus/Standard are presented and tested against analytical models and experiments. Additionally, the work performed here help in understanding the effects of gravity on laboratory experiments on spinning membranes.

The second goal of this thesis is to implement generic simulation tools to study realistic space structures, and to improve the current state-of-the-art of FEM modeling of solar radiation pressure. Origami is a promising method for packaging large flat space structures for launch, but the use of this technique alters the properties of the structure from those of a uniform sheet to those of hinged uniform plates. FEM models of origami structures were used to study the influence of hinges on the linear dynamics of spinning structures and how they compare to the behavior of uniform membranes. Then, we focused on solar radiation pressure and its implementation in FEM. This load is often neglected when it comes to the deformation of stiff spacecraft. As more flexible space structures are developing, solar radiation pressure can become the dominant load and can affect the flatness or even stability of the structure through what is known as solarelastic flutter. When the light beam is transverse to the spinning flat structure it is equivalent to a uniform pressure (for small amplitude of deformation), and the previously discusses studies on wrinkling and nonlinear vibrations apply to that case. When the beam is at an angle, however, the situation is very different and special treatment is required. These conditions are difficult to reproduce on Earth, therefore reliable and efficient simulation tools need to be developed. A finite element implementation of solar radiation pressure for the three types a surface properties, reflective, absorbent, and diffuse is derived and implemented for 3D problems with quadrilateral surface elements in Abaqus/Standard.

Several research projects have studied the dynamics of spinning thin annulus with stationary concentrated force in the context of computer memory disks (Nayfeh et al., 2001; Benson and Bogy, 1978; Benson, 1983; Cole and Benson, 1988; Raman and Mote, 1999; Renshaw, 1998; Renshaw and Mote, 1996). The present analysis differs from this previous work for two reasons. First, the load is either uniformly distributed, in the case of gravity, or deformation-dependent, in the case of solar pressure, as opposed to stationary concentrated loads. Secondly, we consider very flexible disks. Even small loads create large deflections that influence wrinkling and nonlinear vibrations. Several studies focused on the deformation and instabilities induced by solar radiation pressure, especially in the context of solar sailing (McInnes, 1999; MacNeal, 1971). However, most of that work focused on solving the exact PDEs, limiting their application to simple cases. Little work exist on generic FEM formulations of solar radiation pressure that could be used for realistic space structures.

This thesis is composed of four independent chapters. Each chapter has its own introduction, literature review, and conclusion. We present them here.

Chapter 2 presents a complete study of the wrinkling of spinning circular membranes under a transverse, uniform load[1]. A clamped-free annular spinning membrane, subjected to a transverse uniform load, may buckle due to the geometrically nonlinear generation of compressive circumferential stress along the edge of the membrane, resulting from deflections that may be larger than the membrane thickness. Experimental measurements of the angular velocities at which different membranes become wrinkled, and of the wrinkling mode transitions that occur upon spin down, are presented. We experimentally measured the wavelength of the wrinkling pattern of a variety of samples at different angular velocities. A theoretical formulation of the problem is presented, in which pairs of critical angular velocity and critical transverse loads are determined. We analyzed this problem using nonlinear von Kármán plate theory. The results are compared to a previous theory that used a membrane approximation, to FEM simulations, and to experiments. The present formulation is in terms of a dimensionless load and angular velocity, and the transition from bending dominated behavior to in-plane dominated behavior depends on the ratio of the inner to outer radius of the membrane. The wrinkling mode of the membrane can be determined by examining the variation of the eigenvalues with the angular velocity, and the critical mode corresponds to the eigenvalue that reaches zero first. Once the membrane has wrinkled, the wrinkling mode changes as the angular velocity is decreased.

The results from this chapter answer a fundamental question: at what minimum angular velocity should spacecraft rotate in transverse solar radiation pressure to avoid wrinkling?

Chapter 3 studies the transverse vibrations of an annular isotropic, homogeneous membrane spinning at constant angular velocity and deflected by uniform transverse loading[2]. The membrane is clamped at the inner edge and free at the outer edge. The perturbation is axisymmetric. The equilibrium of the membrane under normal load and its natural frequencies are first calculated using the von Kármán plate equations. Next, the Galerkin procedure is used to determine the reduced order model describing the weakly nonlinear vibrations of the axisymmetric modes. It is shown that the vibrations are represented by a single degree of freedom Helmholtz-Duffing oscillator. A given membrane exhibits softening or hardening behavior, jump phenomena or hysteresis depending on the angular velocity, transverse load amplitude, amplitude of excitation, and damping ratio. The results are in excellent agreement with dynamic implicit finite element simulations in Abaqus/Standard. To experimentally validate the results, a experimental apparatus was built. Both digital image correlation and laser vibrometry are used to measure mode shapes and nonlinear vibrations, and good agreement between theory and experiments is observed.

[1]The work in this chapter was performed in collaboration with Prof. John Elie Sader and Dr. Chakraborty from University of Melbourne.

[2]The work in this chapter was performed in collaboration with S. Haegeli Lohaus visiting student from ETH Zurich.

This chapter answers the fundamental question: what is the influence of membrane deflection caused by a uniform load on the linear and nonlinear dynamics of spinning membranes? Generally, the results illustrate how a small deflection of the structure can modify its nonlinear dynamics. This is a characteristic of the novel very flexible structures that we consider in this research. In addition, the results from this chapter can be used to scale experiments on Earth to limit the influence of gravity on nonlinear dynamics.

In Chapter 4, FEM models of creased structure in Abaqus/Standard are presented. We focus on the implementation of the hinges or creases using distributed connector elements. Some origami packageable IKAROS-like structures (Sawada et al., 2007) are analyzed further in terms of stress distribution and frequency analysis. A wide range of results are presented for various plate thicknesses and properties, geometries, topologies and angular velocities. We have considered two types of hinges between the plates, fixed hinges with one degree of freedom and sliding hinges. We compare the linear behavior of those structure with the one of uniform strictures and derived criteria at which the spinning membrane behavior is recovered.

Results from this chapter justify the membrane model for origami packageable structures for appropriate angular velocities. It can also be used as a starting point to implement more realistic FEM models of spacecraft including creases.

Chapter 5 presents a finite element derivation and implementation for solar radiation pressure. This derivation and implementation was performed for the case of quadrilateral surface elements and 3D problems. We used isoparametric mapping and derived explicit formulations of the nodal forces and element submatrices for the three surface types: reflective, absorbent, and diffuse. It is shown that the external force stiffness is unsymmetric. We introduce a method to implement such loads in Abaqus/Standard using an UEL subroutine and a tie constraint. This subroutine was implemented for static (linear and nonlinear) analysis and complex frequency evaluation. This model was tested on benchmark problem for which an explicit PDE was formulated and solved for comparison. A perfect agreement between the two approaches is shown.

This chapter introduces a practical and general way to study the influence of solar radiation pressure on the shape and stability of very flexible structures. It also presents an example of implementation of deformation-dependent load in Abaqus/Standard. This can be used as a generic method to study solar radiation effects on complex space structures.

Finally, Chapter 6 presents the conclusion along with areas of future research.

Chapter 2

Wrinkling of Spinning Membranes Under Transverse Uniform Load

2.1 Introduction

Membranes are widely used in deployable space structures, as they allow tight packaging for launch. Their low bending stiffness, which is so advantageous for efficient packaging, requires that the deployed shape is stabilized by applying a state of prestress, which is often done by applying edge forces through a set of deployable booms (as in the James Webb sunshield (Clampin, 2008)). There is increasing interest in a lighter and potentially simpler approach, in which prestressing is achieved through the use of centrifugal action. It was recently demonstrated in the IKAROS solar sail (Sawada et al., 2007), during which, however, unexpected shape deviations were observed (Satou et al., 2015). Spinning membranes are also of interest for future, ultralight space-based solar power satellites. Both solar sails and solar power satellites require ultralight structures that can remain flat under the load of an incident light beam from the sun. Maintaining a flat shape is important to increase the propulsive action for solar sailing or the total absorption of concentrated photovoltaics.

It is known that thin membranes sheets, as they can carry very little compression, are susceptible to wrinkling. Many wrinkling problem have been studied in the past. Wong and Pellegrino (1999a, 2006, 1999b) have considered the wrinkling of initially flat, linear-elastic and isotropic thin foils subject to in-plane loads, and studied this problem experimentally, analytically, and numerically. Other wrinkling configurations have been studied such as thin sheets under boundary confinement (Vandeparre et al., 2011) for example.

A transverse uniform loading on a spinning membrane can significantly alter the flatness of the structure, causing it to deform into an axisymmetric shallow "cone" that, at sufficiently large transverse loads, buckles into a wrinkled surface. Simmonds (1962a) first studied this transition from axisymmetric to wrinkled, using a stress based wrinkling criterion that neglects the bending stiffness of the membrane. In a pure membrane, i.e., a structure with zero bending stiffness, the onset of compression initiates wrinkling. Simmonds noted

that circumferential compression first occurs on the outer edge of a spinning membrane loaded by gravity, and thus evaluated the load at which the circumferential stress on the outer edge becomes negative. He assumed this load to be equal to the critical buckling load of the membrane. Okuizumi (2007) has carried out experiments in a vacuum chamber on thin, spinning membranes loaded by gravity and vibrating under axisymmetric excitationOkuizumi (2009, 2014). He used the same stress criterion as Simmonds criterion to predict buckling. Chen and Fang (2011) also studied this problem using the von Kármán plate equation with bending and plate stress components in another context: to prove the existence of several equilibrium solutions of a static heavy disk in gravity. They theoretically and experimentally found the equilibrium shape of a rotating heavy disk for one level of dimensionless gravity load and observed wave numbers smaller than 4. Benson and Bogy (1978); Benson (1983); Cole and Benson (1988) studied the deflection of a floppy disk under a stationary, concentrated transverse load. Their solutions include the coupling effects of bending stiffness and in-plane forces.

Here we present a complete study of the wrinkling of circular membranes under a transverse, uniform load, without assuming any particular wrinkling criterion. We begin by measuring the angular velocities and buckling (wrinkling) modes of membranes with different properties and geometries, and we also observe buckling mode transitions that occur upon spin down. We then formulate the buckling problem analytically and obtain a complete numerical solution that provides the critical angular velocities and critical loads, as well the buckled shapes of a spinning membrane. This theory predicts that the shape of the wrinkled membrane varies depending on the angular velocity; we study the link between this result and the experimentally observed mode transitions. Comparison of our results to the previous theory for the buckling of spinning membranes shows that neglecting the bending stiffness of the membrane is quite inaccurate for certain regimes. Also, the buckling modes were not predicted by this theory.

In the first part of the paper we present our experimental setup for spinning membranes loaded by gravity, and we present specific results for three test samples. Then, we introduce an analytical model to evaluate the critical transverse loads and angular velocities, and the waviness, of a spinning membrane using the von Kármán plate equations. We also report the theory developed by Simmonds. Next, we compare the results from our theory with membrane theory, experiments, and finite element simulations. We then present some results during spin down. Finally, we present an application to a spinning solar power collecting membrane in space.

2.2 Experiments

2.2.1 Setup

We developed a setup that horizontally spins a membrane in a transparent vacuum chamber, at controlled angular velocities of up to 1200 rpm, as shown in Fig. 2.1. Digital image correlation (Vic 3D, by Correlated Solutions) was used to measure the equilibrium shapes. The maximum edge velocity of the membrane was 25 m s^{-1}; to avoid blurring, we set the cameras to an exposure time of 13 μs. A uniform transverse load on the membrane was provided by Earth's gravity. A closed loop motor with Hall sensors from Maxon, model

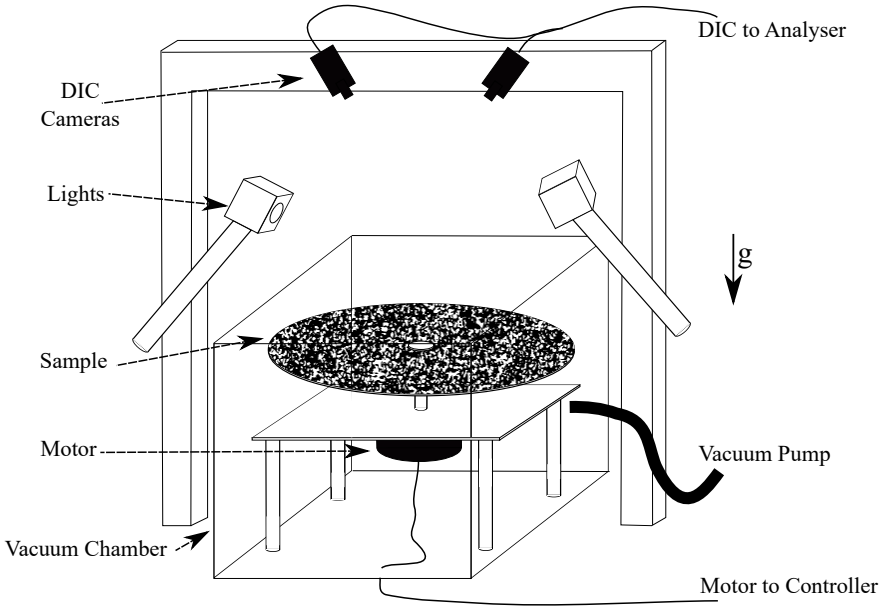

Figure 2.1: Mechanical test setup.

EC 90, flat, brushless, 90 Watt was used. The controller is a ESCON 50/5, 4-Q Servocontroller. The motor voltage profile is prescribed though NI Signal Express and a digital-to-analog converter is used to input the profile to the controller. The rotation at the hub is measured and found to perfectly follow the imposed profile as seen Fig. 2.3 despite the various component in rotation and the change in shape of the membrane. It is necessary to use a vacuum chamber for those experiments for two reasons. First, it is difficult to spin up the membrane in air as it tends to stick the the lower plate. Second, the surrounding air would perturb the membrane equilibrium shape while the membrane in spinning, by dynamically exciting it or create flutter instabilities. We have used a custom made acrylic jar of 125×10^3 cm^{-3}. The fully transparent jar enables to illuminate the sample from the outside and to image through the top lid. An aluminum rack holds the cameras about 70 cm above the acrylic jar. This distance is prescribed by the required field of view (size of the sample) and the optical lenses that were used. More details are provided in Section 2.2.2. The jar lies on

a thick aluminum plate through which we run the connections to the motor. We used a roughing pump from Welch. Overall we reached a steady vacuum level 0.06 atm. We show the global setup in Fig. 2.2 from the input voltage to the motor controller in the lower right to the measured 3D shape of a spinning membrane in the upper right.

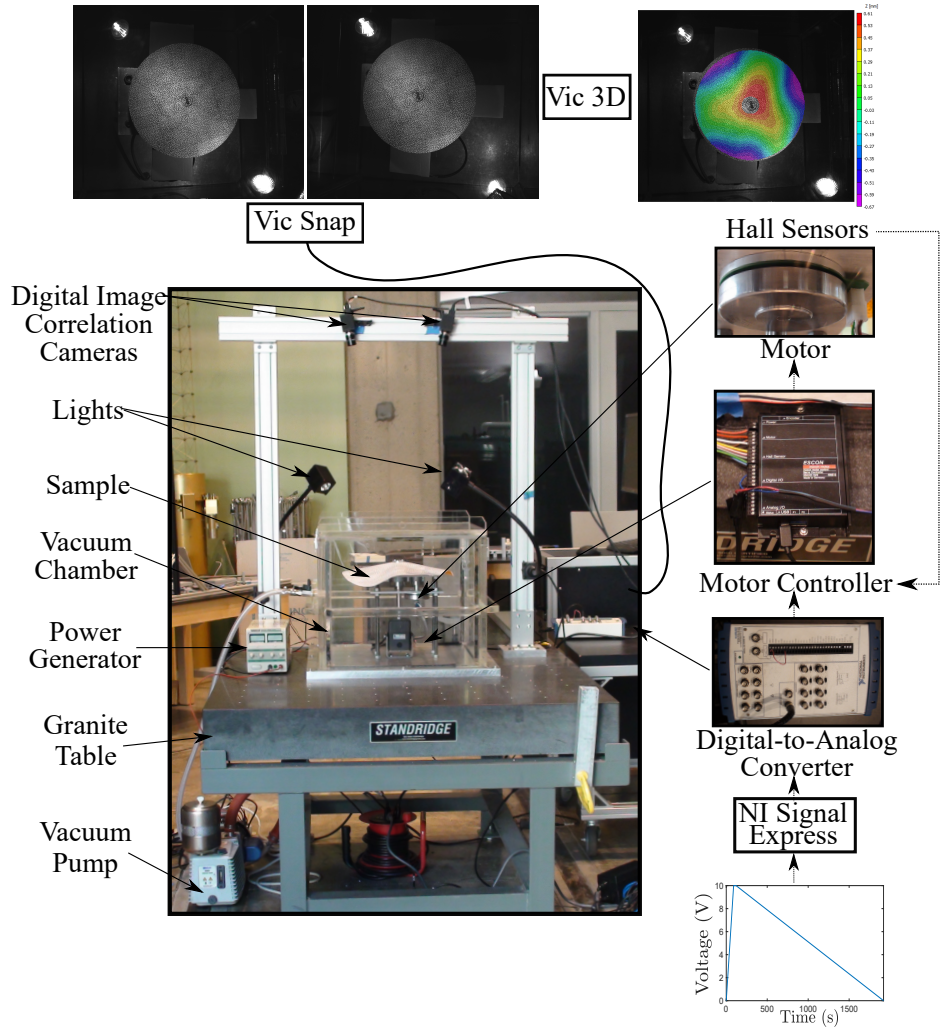

Figure 2.2: Overall test setup.

2.2.2 Measurement Technique

Stereo Digital Image Correlation was used to measure the shapes of the sample (the displacement wasn't used). Our stereo DIC system consists of two Point Grey Grasshopper cameras (GRAS-50S5M-C) with a resolution of 2448 $\times$ 2048, 3.45 μm pixel size and a gain range between 0 dB and 24 dB. We used lenses with a focal length of 12 mm to image our sample. The stereo angle was about 25°. We used the commercial

software VIC-Snap and VIC-3D by Correlated Solutions to respectively acquire synchronized images at a certain rate and to correlate them. The biggest membrane is 40 cm in diameter and the field of view is about 50 cm which corresponds to a pixel size of 200 μm. We drew speckles about 2 mm wide (10 px) on the membrane with black ink and a roller rubber stamp after spraying a very thin layer of white paint.

The parameters used for the correlation are a subset of 29 pixels (corresponding to a square side length of 0.58 cm) and density of 7 pixels. Choosing a large subset decreases the noise but also decreases spatial resolution by averaging the deformation linearly within a subset during matching. We overall obtained 51372 data points for a spatial resolution of about 5 mm. We have used the following parameters in the software: the shape functions assume linear deformation within subset with Gaussian weights, the pixel interpolation uses 8-tap splines, the minimization algorithm used a zero-normalized square difference (unaffected by offset plus scale change is lighting). In

The membrane spins at an angular velocity up to 1200 rpm. To reduce the blur on the outer edge, we used a short exposure time. The DIC system is able to achieve sub pixel resolution and the exposure time should be chosen such as to keep motion below 0.01 px. We took images at 13 μs, which corresponds to a motion of 160 μm (0.8 px) on the very edge. This explains that even if no blur is noticeable on the images, the noise is higher at high angular velocity and towards the edges. In addition some optical distortion is introduced by the lid of the vacuum chamber. More details on measurements noise and bias can be found in Appendix B. Overall it is found that they will not affect our estimate of the waviness of the equilibrium shape which is the main measure of the experiments.

2.2.3 Results

The membrane was attached at the center to a rigid hub connected to the axis of the motor. Under these initial, static conditions, the membrane took up a smooth cylindrical shape resting on the plate supporting the motor. The test procedure consisted in spinning up each membrane to the maximum angular velocity (1200 rpm); at this speed all tested membranes had reached a fully axisymmetric shape. For the first two test samples (aluminum plates Al-13 and Al-20, see Table 2.1), we decreased the angular velocity in steps of 50 rpm, waited 1 min for any transient dynamic effects to dissipate, and then took pairs of images with the DIC cameras. We repeated this sequence until the shape was no longer axisymmetric. For the third test sample (Kapton membrane Ka-20, see Table 2.1) we decreased the angular velocity at a rate of 1 rpm s^{-1} and took a pair of images every 10 seconds (see Fig. 2.3).

After completing these tests, we used the Vic3D software to compute a set of shapes of the membrane at each angular velocity with rigid body motion components removed. For the aluminum samples the wave number is small and could be estimated directly from the images. For Ka-20, we decomposed each of these experimentally obtained shapes using the computed vibration mode shapes of the membrane as a basis (as

Sample	Al-13	Al-20	Ka-20
Young's modulus E (GPa)	69	69	2.5
Poisson's ratio ν	0.34	0.34	0.34
Density ρ (kg m^{-3})	2700	2700	1420
Thickness h (μm)	152	152	50
Outer radius b (cm)	13	20	20
Inner radius a (cm)	1.3	2	2

Table 2.1: Properties and dimensions of the three samples.

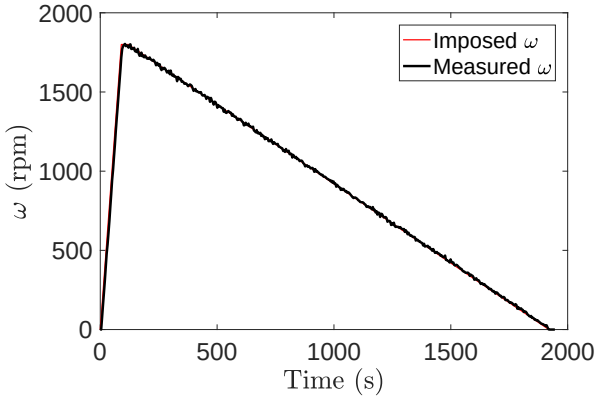

Figure 2.3: Measured angular velocity at motor axis (Angular velocity at the hub is $\frac{2}{3}$ because of gears).

explained Appendix A). At all angular velocities we measured a significant $n = 0$ component, corresponding to the axisymmetric, gravity induced deformation. Components in the range $n = 1, \ldots 6$ were considered to be the effects of initial non-flatness of the membrane. The membrane was considered to have buckled if a buckling mode shape with amplitude greater than h and $n \geq 6$ could be observed, in which case the membrane was assumed to have buckled into the corresponding mode shape.

An analysis of the membrane shapes at each angular velocity showed that at a critical angular velocity the axisymmetric (pre-buckling) shape transitions to an n-fold symmetric buckled (wrinkled) wavy shape, where the particular value of n depends on the specific properties of the membrane. At lower angular velocities further transitions occur to buckled shapes with smaller values of n.

It will be shown in the next section (2.3.2) that, for given Poisson's ratio and hub to outer radius ratio, this buckling problem can be described by two non-dimensional parameters: the equivalent gravity and the equivalent angular velocity. The three test samples in Table 2.1 span the parameter range by means of different bending stiffnesses and membrane diameter. Their axisymmetric, pre-buckling shapes and their buckled shapes are shown in Figure 2.4. We notice that the experimental pre-buckling shapes aren't perfectly axisymmetric. We attribute those discrepancies to material imperfections.

Figure 2.5 is a plot of the amplitude corresponding to each value of n for decreasing angular velocity, for

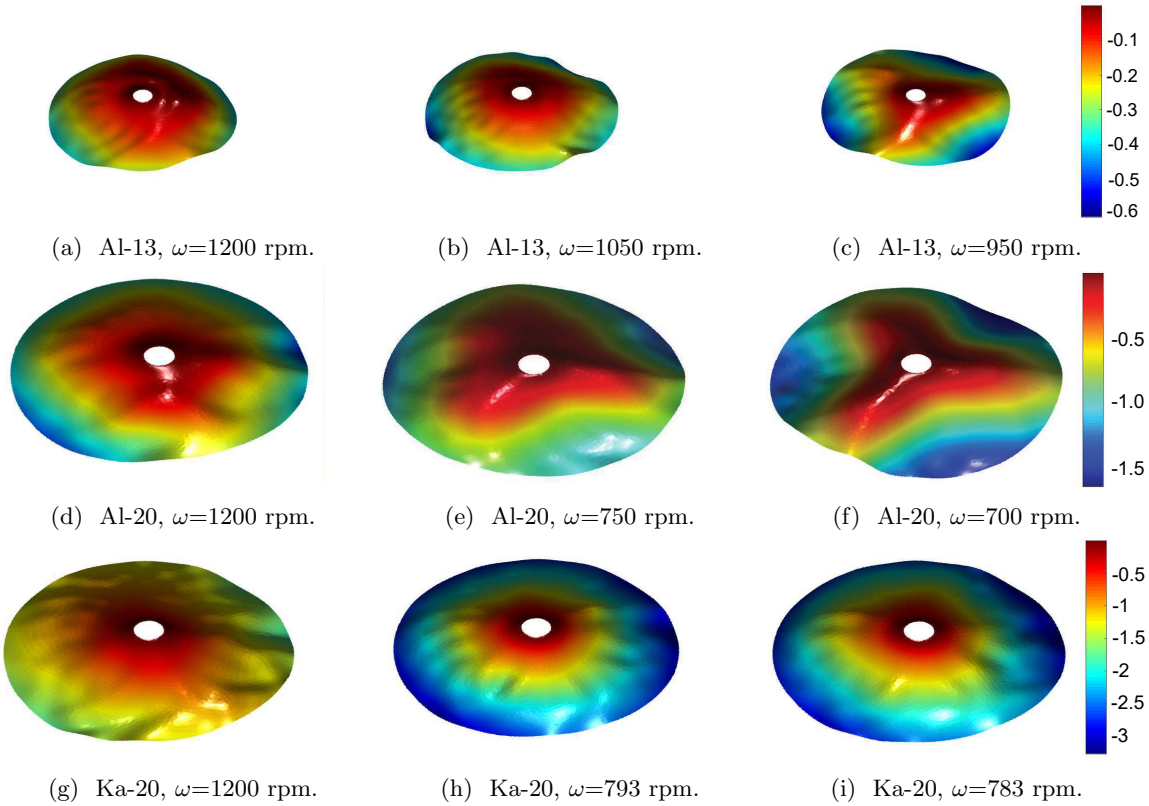

(a) Al-13, ω=1200 rpm. (b) Al-13, ω=1050 rpm. (c) Al-13, ω=950 rpm.

(d) Al-20, ω=1200 rpm. (e) Al-20, ω=750 rpm. (f) Al-20, ω=700 rpm.

(g) Ka-20, ω=1200 rpm. (h) Ka-20, ω=793 rpm. (i) Ka-20, ω=783 rpm.

Figure 2.4: Axisymmetric shapes (a, d, g), pre-buckling (b, e, h), and buckled (c,f,i) equilibrium shapes of tested membranes. Deflection units are mm.

the Kapton membranes. The critical velocities were found to be 1100 rpm for Al-13, 800 rpm for Al-20, and 793 rpm for Ka-20. The wrinkling wavelengths, just after buckling, were three waves for Al-13, 3 for Al-20, and 12 for Ka-20.

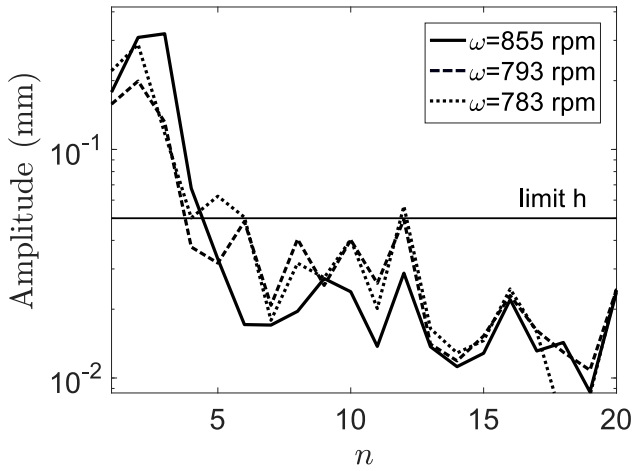

Figure 2.5: Experimentally derived wave numbers for Ka-20 test sample, at ω = 855, 793 , and 783 rpm. h=50 μm corresponds to the membrane thickness.

2.3 Theory

In order to explain these interesting experimental observations theoretical models are proposed. We formulate in this part the analytical formulation of the problem. First, we present Simmonds's theory that neglects the bending stiffness followed by the von Kármán plate formulation that includes both bending stiffness and in plane stress due to centrifugal force. We will compare the two approaches in Section 2.4. Some results in terms of buckling loads and buckling shapes are presented for a wide range of dimensionless parameters. Finally we present FEM results in Abaqus/Standard and introduce a search algorithm to derive buckling limits on nonlinear loading path in Abaqus/Standard. The geometry and loading parameters are presented Figure 2.6.

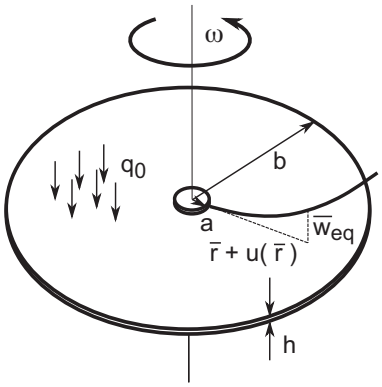

Figure 2.6: Definition of geometry and loading parameters.

2.3.1 Membrane Theory

When the bending stiffness of the plate is neglected there is a simple relation between angular velocity and transverse load. This model was first derived by Simmonds (1962a) and is summarized here for the case of clamped-free boundary conditions. This theory uses the Föppl's equations. The basic equations governing this system are as follows:
In-plane equilibrium:

$$\frac{d}{dr}\left(r\sigma_r\right) - \sigma_\theta + \rho r^2 \omega^2 = 0 \tag{2.1}$$

with σ_r and σ_θ being the radial and hoop stresses. Out-of-plane equilibrium:

$$2hr\sigma_r \frac{dW}{dr} = -q_0\left(b^2 - r^2\right) \tag{2.2}$$

where W is the equilibrium axisymmetric deflection.

Stress-Strain relation:

$$Ee_r = \sigma_r - \nu\sigma_\theta \tag{2.3}$$

$$Ee_\theta = \sigma_\theta - \nu\sigma_r \tag{2.4}$$

Compatibility equation:

$$\frac{dre_\theta}{dr} - e_r + \frac{1}{2}\left(\frac{dW}{dr}\right)^2 = 0 \tag{2.5}$$

Then a stress function F is introduced:

$$r\sigma_r = F \tag{2.6}$$

$$\sigma_\theta = \frac{dF}{dr} + \rho r^2\omega^2 \tag{2.7}$$

Combining Equations 2.2 and 2.6, one obtains:

$$\frac{dW}{dr} = -\frac{q_0\left(b^2 - r^2\right)}{2hF} \tag{2.8}$$

Combining Equations 2.1, 2.6, and 2.7, the following nonlinear differential equation was derived:

$$\frac{d}{dr}\left(r\frac{dF}{dr}\right) - \frac{F}{r} + \frac{Eq_o^2\left(b^2 - r^2\right)^2}{8h^2F^2} + (3+\nu)\rho r^2\omega^2 \tag{2.9}$$

The outer edge of the membrane is stress free. The inner edge fixed restraint requires that $e_\theta = 0$. Using Equations 2.4, 2.6, and 2.7 the boundary conditions in terms of the stress function F are:

$$F(b) = 0 \tag{2.10}$$

$$\frac{dF}{dr}\Big|_{r=a} + \rho a^2\omega^2 - \frac{\nu F(a)}{a} = 0 \tag{2.11}$$

A stress criterion is used to derive the buckling limits. The membrane buckles when the hoop stress on the outer edge becomes negative:

$$\sigma_\theta(b) = 0 \tag{2.12}$$

The following dimensionless parameters are introduced:

$$\xi = \left(\frac{r}{b}\right)^2 \tag{2.13}$$

$$f = \frac{8rF}{(3+\nu)\,\rho b^4 \omega^2} \tag{2.14}$$

$$\tag{2.15}$$

and Equation 2.9 becomes:

$$\frac{d^2 f}{d\xi^2} + \left[\frac{k\,(1-\xi)^2}{f^2}\right] + 2 = 0 \tag{2.16}$$

with k given by:

$$k = \frac{16 E q_0^2}{(3+\nu)^3\, h^2 \rho^3 b^4 \omega^6} \tag{2.17}$$

We can derive the associated dimensionless boundary conditions:

$$f(1) = 0 \tag{2.18}$$

$$f(\sqrt{\alpha}) - \frac{2\alpha}{1+\nu}\left(\frac{df}{d\xi}\Big|_{\xi=\sqrt{\alpha}} + \frac{4\alpha}{3+\nu}\right) = 0 \tag{2.19}$$

and rewrite the buckling criterion 2.12:

$$2\frac{df}{dr}\Big|_{r=b} + \frac{8}{3+\nu} = 0 \tag{2.20}$$

Purely by this dimensional analysis Simmonds found that the buckling criterion depends on three dimensionless parameters k, α and ν. The buckling condition is:

$$k \geq k_{crit}\,(\alpha, \nu) \tag{2.21}$$

We can express this buckling condition according to the dimensionless parameters G, Ω, α and ν that are going to be introduced in the next section (Equation 2.51). We find that G is proportional to the cube of Ω as:

$$G = \sqrt{\frac{k_{crit}\,(\alpha,\nu)\,(3+\nu)^3}{192\,(1-\nu^2)}}\,\Omega^3 \tag{2.22}$$

Estimating $k_{critic}\,(\alpha, \nu)$ requires solving a boundary value problem of one second order ODE (Equation 2.16)

with boundary conditions Equations 2.18 and 2.19 for many different k, up to the criterion Equation 2.20. We will show some results using this theory in Section 2.4. In the next section we solve the same problem, including the bending stiffness and using the von Kármán plate theory.

2.3.2 Thin Plate Theory

2.3.2.1 Nonlinear Equations for Spinning Plates

The theory presented here investigates the stability of the deflected membrane by analyzing the sign of the eigenvalues of the stiffness operator. The membrane will buckle when at least one eigenvalue reaches zero and the wrinkled configuration corresponds to the waviness of the unstable mode. We derive the geometrically nonlinear axisymmetric equilibrium configuration of a spinning plate. Then, we derive the eigenvalue problem and solve it at fixed angular velocities for a wide range of gravity amplitudes, for a wide range of eigenmodes, until negative eigenvalues are obtained.

First we re-derive the equations governing the dynamics of spinning disks as summarized by Nayfeh (2000) but originally derived by Nowinski (1964). The natural frequencies of the in-plane modes are assumed to be large compared to the frequencies of the transverse modes so that we can neglect the radial and hoop accelerations $\frac{\partial^2 u}{\partial t^2}$ and $\frac{\partial^2 v}{\partial t^2}$. Nowinski derived the governing equations for spinning disks. Adding a forcing term q_0 we have:

$$\frac{\partial N_r}{\partial \bar{r}} + \frac{1}{\bar{r}}\frac{\partial N_{r\theta}}{\partial \theta} + \frac{N_r - N_\theta}{\bar{r}} + \rho h \omega^2 \bar{r} = 0 \tag{2.23}$$

$$\frac{1}{\bar{r}}\frac{\partial N_\theta}{\partial \theta} + \frac{\partial N_{r\theta}}{\partial \bar{r}} + \frac{2N_{r\theta}}{\bar{r}} = 0 \tag{2.24}$$

$$\begin{aligned}\rho h \frac{\partial^2 \bar{w}}{\partial \bar{t}^2} + D\nabla^4 \bar{w} = {} & \frac{1}{\bar{r}}\frac{\partial}{\partial \bar{r}}\left(\bar{r} N_r \frac{\partial \bar{w}}{\partial \bar{r}}\right) + \frac{1}{\bar{r}^2}\frac{\partial}{\partial \theta}\left(N_\theta \frac{\partial \bar{w}}{\partial \theta}\right) \\ & + \frac{1}{\bar{r}}\frac{\partial}{\partial \theta}\left(N_{r\theta}\frac{\partial \bar{w}}{\partial \bar{r}}\right) + \frac{1}{\bar{r}}\frac{\partial}{\partial \bar{r}}\left(N_{r\theta}\frac{\partial \bar{w}}{\partial \theta}\right) + q_0\left(\bar{r}, \theta, \bar{t}\right)\end{aligned} \tag{2.25}$$

where ρ is the density (kg m^{-3}), E the Young's modulus (Pa), ν the Poisson's ratio, and $D = \frac{Eh^3}{12(1-\nu^2)}$ the bending stiffness of the membrane. Also, ω is the angular velocity (rad s^{-1}), $\bar{w}$ the vertical deflection component (m) and $q_0(r, \theta)$ the transverse load (Pa) applied to the membrane. The overbars correspond to dimensional quantities, opposed to the non dimensional quantities that will be introduced Section 2.3.2.2.

We introduce the stress function $\bar{\Phi}$ (Nm) defined by N_r the radial force, N_θ the hoop force, and $N_{r\theta}$ the

shear force and considering in-plane centrifugal body force as:

$$N_r = \frac{1}{\bar{r}}\frac{\partial \bar{\Phi}}{\partial \bar{r}} + \frac{1}{\bar{r}^2}\frac{\partial^2 \bar{\Phi}}{\partial \theta^2} - \frac{1}{2}\rho h \omega^2 \bar{r}^2 \tag{2.26}$$

$$N_\theta = \frac{\partial^2 \bar{\Phi}}{\partial \bar{r}^2} - \frac{1}{2}\rho h \omega^2 \bar{r}^2 \tag{2.27}$$

$$N_{r\theta} = -\frac{1}{\bar{r}}\frac{\partial^2 \bar{\Phi}}{\partial \bar{r}\partial \theta} + \frac{1}{\bar{r}^2}\frac{\partial \bar{\Phi}}{\partial \theta} \tag{2.28}$$

Substituting Equations 2.26, 2.27, and 2.28 into 2.25, one obtains:

$$\begin{aligned}\rho h \frac{\partial^2 \bar{w}}{\partial \bar{t}^2} + D\nabla^4 \bar{w} + \frac{1}{2}\rho h \omega^2 \bar{r}^2 \nabla^2 \bar{w} + \rho h \omega^2 \bar{r} \frac{\partial \bar{w}}{\partial \bar{r}} = \\ \frac{\partial^2 \bar{w}}{\partial \bar{r}^2}\left(\frac{1}{\bar{r}}\frac{\partial \bar{\Phi}}{\partial \bar{r}} + \frac{1}{\bar{r}^2}\frac{\partial^2 \bar{\Phi}}{\partial \theta^2}\right) + \frac{\partial^2 \bar{\Phi}}{\partial \bar{r}^2}\left(\frac{1}{\bar{r}}\frac{\partial \bar{w}}{\partial \bar{r}} + \frac{1}{\bar{r}^2}\frac{\partial^2 \bar{w}}{\partial \theta^2}\right) \\ - 2\left(\frac{1}{\bar{r}}\frac{\partial^2 \bar{\Phi}}{\partial \bar{r}\partial \theta} - \frac{1}{\bar{r}^2}\frac{\partial \bar{\Phi}}{\partial \theta}\right)\left(\frac{1}{\bar{r}}\frac{\partial^2 \bar{w}}{\partial \bar{r}\partial \theta} - \frac{1}{\bar{r}^2}\frac{\partial \bar{w}}{\partial \theta}\right) + q_0\left(\bar{r}, \theta, \bar{t}\right)\end{aligned} \tag{2.29}$$

The compatibility equation in polar coordinates is:

$$\begin{aligned}\frac{\partial^2 e_r}{\partial \theta^2} - \frac{\partial^2\left(\bar{r} e_{r\theta}\right)}{\partial \bar{r}\partial \theta} + \frac{\partial}{\partial \bar{r}}\left(\bar{r}^2 \frac{\partial e_\theta}{\partial \bar{r}}\right) - \bar{r}\frac{\partial e_r}{\partial \bar{r}} = \\ \left(\frac{\partial^2 \bar{w}}{\partial \bar{r}\partial \theta} - \frac{1}{\bar{r}}\frac{\partial \bar{w}}{\partial \theta}\right)^2 - \frac{\partial^2 \bar{w}}{\partial \bar{r}^2}\left(\bar{r}\frac{\partial \bar{w}}{\partial \bar{r}} + \frac{\partial^2 \bar{w}}{\partial \theta^2}\right)\end{aligned} \tag{2.30}$$

Assuming a Hookean isotropic material, the in-plane forces are related to the strains e_r, e_θ, and $e_{r\theta}$ of the midplane as:

$$N_r = \frac{Eh}{1-\nu^2}\left(e_r + \nu e_\theta\right) \tag{2.31}$$

$$N_\theta = \frac{Eh}{1-\nu^2}\left(e_\theta + \nu e_r\right) \tag{2.32}$$

$$N_{r\theta} = \frac{Eh}{2\left(1+\nu\right)} e_{r\theta} \tag{2.33}$$

Using Equations 2.31, 2.32, 2.33, 2.26, 2.27, and 2.28 we can express the strain according to the stress function.

$$e_r = \frac{1}{Eh}\left(\frac{1}{\bar{r}}\frac{\partial \bar{\Phi}}{\partial \bar{r}} + \frac{1}{\bar{r}^2}\frac{\partial^2 \bar{\Phi}}{\partial \theta^2} - \nu\frac{\partial^2 \bar{\Phi}}{\partial \bar{r}^2} - \frac{1}{2}(1-\nu)\rho h \omega^2 \bar{r}^2\right) \tag{2.34}$$

$$e_\theta = \frac{1}{Eh}\left(\frac{\partial^2 \bar{\Phi}}{\partial \bar{r}^2} - \nu\left(\frac{1}{\bar{r}}\frac{\partial \bar{\Phi}}{\partial \bar{r}} + \frac{1}{\bar{r}^2}\frac{\partial^2 \bar{\Phi}}{\partial \theta^2}\right) - \frac{1}{2}(1-\nu)\rho h \omega^2 \bar{r}^2\right) \tag{2.35}$$

$$e_{r\theta} = \frac{2(1+\nu)}{Eh}\left(\frac{1}{\bar{r}^2}\frac{\partial \bar{\Phi}}{\partial \theta} - \frac{1}{\bar{r}}\frac{\partial^2 \bar{\Phi}}{\partial \bar{r}\partial \theta}\right) \tag{2.36}$$

Using Equations 2.34, 2.35, and 2.36 with the compatibility Equation 2.30, we obtain:

$$\nabla^4\bar{\Phi} - 2\left(1-\nu\right)\rho h\omega^2 = Eh\left[\left(\frac{1}{\bar{r}}\frac{\partial^2\bar{w}}{\partial\bar{r}\partial\theta} - \frac{1}{\bar{r}^2}\frac{\partial\bar{w}}{\partial\theta}\right)^2 - \frac{\partial^2\bar{w}}{\partial\bar{r}^2}\left(\frac{1}{\bar{r}}\frac{\partial\bar{w}}{\partial\bar{r}} + \frac{1}{\bar{r}^2}\frac{\partial^2\bar{w}}{\partial\theta^2}\right)\right] \tag{2.37}$$

Let us now look into the boundary conditions:

At the clamped edge we have

$$\bar{w} = 0,\ \frac{\partial\bar{w}}{\partial\bar{r}} = 0,\ u = 0, \text{ and } v = 0 \tag{2.38}$$

The midplane strains are related to the transverse displacements w, the radial displacement u, and the hoop displacement v by:

$$e_r = \frac{\partial u}{\partial\bar{r}} + \frac{1}{2}\left(\frac{\partial\bar{w}}{\partial\bar{r}}\right)^2 \tag{2.39}$$

$$e_\theta = \frac{u}{\bar{r}} + \frac{1}{\bar{r}}\frac{\partial v}{\partial\theta} + \frac{1}{2\bar{r}^2}\left(\frac{\partial\bar{w}}{\partial\theta}\right)^2 \tag{2.40}$$

$$e_{r\theta} = \frac{1}{\bar{r}}\frac{\partial u}{\partial\theta} + \frac{\partial v}{\partial\bar{r}} - \frac{v}{\bar{r}} + \frac{1}{\bar{r}}\frac{\partial\bar{w}}{\partial\bar{r}}\frac{\partial\bar{w}}{\partial\theta} \tag{2.41}$$

It follows that:

$$e_\theta = 0, \text{ and } \frac{\partial}{\partial\bar{r}}\left(\bar{r}e_r\right) - e_r - \frac{\partial}{\partial\theta}\left(e_{r\theta}\right) = 0 \tag{2.42}$$

Using Equations 2.34, 2.35, 2.36, and 2.42 we obtain conditions on the displacements u, v written in terms of the stress function:

$$\begin{aligned}\frac{\partial^2\bar{\Phi}}{\partial\bar{r}^2} - \nu\left(\frac{1}{\bar{r}}\frac{\partial\bar{\Phi}}{\partial\bar{r}} + \frac{1}{\bar{r}^2}\frac{\partial^2\bar{\Phi}}{\partial\theta^2}\right) - \frac{(1-\nu)}{2}\omega^2\bar{r}^2 = 0\\ \frac{\partial^3\bar{\Phi}}{\partial\bar{r}^3} + \frac{1}{\bar{r}}\frac{\partial^2\bar{\Phi}}{\partial\bar{r}^2} - \frac{1}{\bar{r}^2}\frac{\partial\bar{\Phi}}{\partial\bar{r}} + \frac{2+\nu}{\bar{r}^2}\frac{\partial^3\bar{\Phi}}{\partial\bar{r}\partial\theta^2} - \frac{3+\nu}{\bar{r}^3}\frac{\partial^2\bar{\Phi}}{\partial\theta^2}\\ - \left(1-\nu\right)\omega^2\bar{r} = 0\end{aligned} \tag{2.43}$$

At the free edge we have:

$$N_r = 0,\ N_{r\theta} = 0,\ M_r = 0, \text{ and } Q_r + \frac{1}{\bar{r}}\frac{\partial M_{r\theta}}{\partial\theta} = 0 \tag{2.44}$$

The moments and traverse shear forces are related to w by:

$$M_r = -D\left(\frac{\partial^2 \bar{w}}{\partial \bar{r}^2} + \frac{\nu}{\bar{r}}\frac{\partial \bar{w}}{\partial \bar{r}} + \frac{\nu}{\bar{r}^2}\frac{\partial^2 \bar{w}}{\partial \theta^2}\right) \tag{2.45}$$

$$M_\theta = -D\left(\frac{1}{\bar{r}}\frac{\partial \bar{w}}{\partial \bar{r}} + \frac{1}{\bar{r}^2}\frac{\partial^2 \bar{w}}{\partial \theta^2} + \nu\frac{\partial^2 \bar{w}}{\partial \bar{r}^2}\right) \tag{2.46}$$

$$M_{r\theta} = -D\left(1-\nu\right)\left(\frac{1}{\bar{r}}\frac{\partial^2 \bar{w}}{\partial \bar{r}\partial \theta} - \frac{1}{\bar{r}^2}\frac{\partial \bar{w}}{\partial \theta}\right) \tag{2.47}$$

$$Q_r = -D\frac{\partial}{\partial \bar{r}}\left(\nabla^2 \bar{w}\right) \tag{2.48}$$

$$Q_\theta = -\frac{D}{\bar{r}}\frac{\partial}{\partial \theta}\left(\nabla^2 \bar{w}\right) \tag{2.49}$$

Thus combining Equations 2.26, 2.28, 2.45, 2.47, and 2.48 we obtain:

$$\begin{aligned}
\frac{\partial}{\partial \bar{r}}\left(\nabla^2 \bar{w}\right) + \frac{(1-\nu)}{\bar{r}^2}\frac{\partial^2}{\partial \theta^2}\left(\frac{\partial \bar{w}}{\partial \bar{r}} - \frac{\bar{w}}{\bar{r}}\right) &= 0 \\
\frac{\partial^2 \bar{w}}{\partial \bar{r}^2} + \nu\left(\frac{1}{\bar{r}}\frac{\partial \bar{w}}{\partial \bar{r}} + \frac{1}{\bar{r}^2}\frac{\partial^2 \bar{w}}{\partial \theta^2}\right) &= 0 \\
\frac{1}{\bar{r}}\frac{\partial \bar{\Phi}}{\partial \bar{r}} + \frac{1}{\bar{r}^2}\frac{\partial^2 \bar{\Phi}}{\partial \theta^2} - \frac{1}{2}\omega^2 \bar{r}^2 &= 0 \\
-\frac{1}{\bar{r}}\frac{\partial^2 \bar{\Phi}}{\partial \bar{r}\partial \theta} + \frac{1}{\bar{r}^2}\frac{\partial \bar{\Phi}}{\partial \theta} &= 0
\end{aligned} \tag{2.50}$$

Equations 2.29 and 2.37 with the boundary conditions Equations 2.38, 2.43, and 2.50 are the starting point of our analysis. They are equivalent to considering the leading term of the expansion of a three-dimensional, nonlinear elastic solid (Ciarlet, 1980), for the case of large displacements and small strains.

2.3.2.2 Buckling Equations

The following dimensionless parameters, defined in terms of the geometry and loading parameters in Figure 2.6, are introduced:

$$\begin{aligned}
r &= \frac{\bar{r}}{b} & \alpha &= \frac{a}{b} \\
w_{eq} &= \frac{\bar{w}_{eq}}{h} & \Phi_{eq} &= \frac{\bar{\Phi}_{eq}}{D} \\
\Omega &= \sqrt{\frac{\rho h}{D}} b^2 \omega & G &= \frac{b^4}{Dh} q_0
\end{aligned} \tag{2.51}$$

The subscript eq denotes the pre-buckling equilibrium configuration.

Within the von Kármán's plate theory, a solar pressure normal to the membrane is equivalent to a uniformly distributed vertical force. In the first case q_0 is the magnitude of the pressure and in the second case $q_0 = \rho g h$ with g the acceleration due to gravity.

From Equations 2.29 and 2.37 we obtained the axisymmetric equilibrium equations in terms of the non-dimensional deflection and non-dimensional stress function:

$$\begin{aligned}\nabla^4 w_{eq} + \Omega^2 \left(\frac{1}{2} r^2 \nabla^2 w_{eq} + r \frac{\partial w_{eq}}{\partial r}\right) - L(w_{eq}, \Phi_{eq}) &= G \\ \nabla^4 \Phi_{eq} + 6\left(1-\nu^2\right) L(w_{eq}, w_{eq}) - 2\left(1-\nu\right)\Omega^2 &= 0\end{aligned} \tag{2.52}$$

where the operator L is defined as:

$$\begin{aligned}L(w,\Phi) = \frac{\partial^2 w}{\partial r^2}\left(\frac{1}{r}\frac{\partial \Phi}{\partial r} + \frac{1}{r^2}\frac{\partial^2 \Phi}{\partial \theta^2}\right) + \frac{\partial^2 \Phi}{\partial r^2}\left(\frac{1}{r}\frac{\partial w}{\partial r} + \frac{1}{r^2}\frac{\partial^2 w}{\partial \theta^2}\right) \\ - 2\left(\frac{1}{r}\frac{\partial^2 \Phi}{\partial r \partial \theta} - \frac{1}{r^2}\frac{\partial \Phi}{\partial \theta}\right)\left(\frac{1}{r}\frac{\partial^2 w}{\partial r \partial \theta} - \frac{1}{r^2}\frac{\partial w}{\partial \theta}\right)\end{aligned} \tag{2.53}$$

The boundary conditions for this problem are free on the outer edge ($r = 1$) and clamped on the inner edge ($r = \alpha$). They are the same as Equations 2.38, 2.43, and 2.50 replacing ω by its dimensionless expression Ω.

The axisymmetric equilibrium shape is obtained from a subset of these equations. The fourth Equation 2.50 is identically satisfied and can be neglected. The remaining Equations 2.52 - 2.50 define a boundary value problem made of two coupled 4th order ODEs that we have solved in Matlab using the built in function bvp4c.

We derived the eigenvalue problem by considering a small perturbation (buckling mode), w, from the axisymmetric equilibrium configuration. We substituted this buckled configuration into Equation 2.52 and linearized the equations. We then obtained the stiffness operator around the axisymmetric equilibrium. The eigenvalues λ and eigenmodes (w,Φ) of the stiffness operator are the solutions of the following boundary value problem:

$$\begin{aligned}-\lambda w + \nabla^4 w + \Omega^2 \left(\frac{1}{2} r^2 \nabla^2 w + r \frac{\partial w}{\partial r}\right) \\ = L(w, \Phi_{eq}(G,\Omega)) + L(w_{eq}(G,\Omega), \Phi) \\ \nabla^4 \Phi = -12\left(1-\nu^2\right) L(w_{eq}(G,\Omega), w)\end{aligned} \tag{2.54}$$

The boundary conditions for the buckling mode are the same as the conditions on w_{eq} in Equations 2.38 - 2.50; we only need to replace Ω by zero.

We look at the modes by separation of variables:

$$\begin{aligned}w(r,\theta) &= W(r)\exp(in\theta) \\ \Phi(r,\theta) &= \Phi(r)\exp(in\theta)\end{aligned} \tag{2.55}$$

where n is an integer (due to periodicity in θ) and i the imaginary unit. The mode shapes end up being real values.

2.3.3 Results

Figure 2.7a shows this nonlinear axisymmetric solution for Ω=200, and for increasing G up to buckling. We also plot the relative deflection at buckling in Figure 2.7b. This curve doesn't cross zero because static thick plates can deform up to 80% of the thickness before buckling. This number becomes 5.5 $\times 10^3$% at Ω=200.

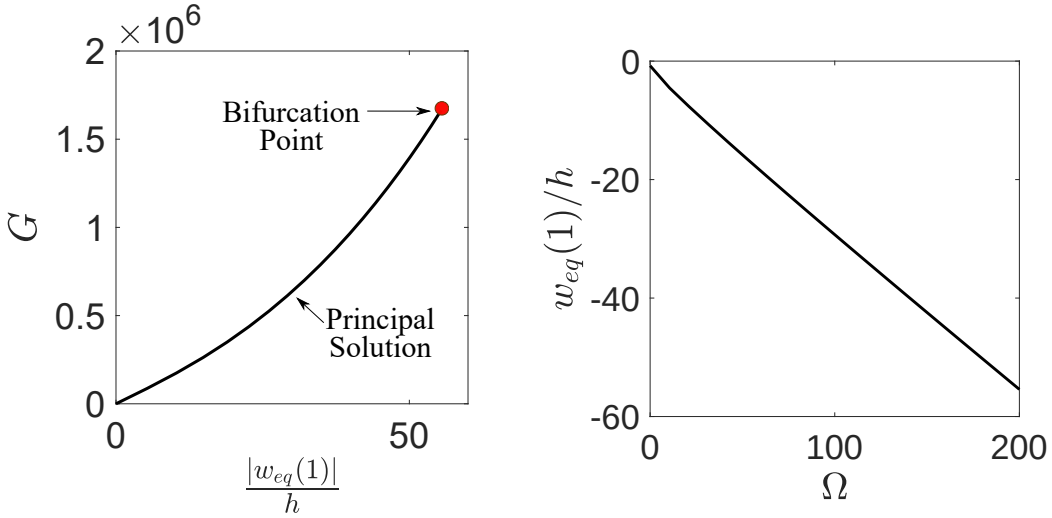

(a) Nonlinear loading path for Ω=200. (b) Deflection at buckling point.

Figure 2.7: Axisymmetric equilibrium of heavy rotating disk.

For a given Ω, α and ν we found the nondimensional critical buckling load, G_{crit}, by computing the eigenvalues for increasing G until the lowest eigenvalue became equal to zero. The corresponding value of G is G_{crit}. The buckling modes have one nodal circle and n radial wrinkles. In Figure 2.8 we have plotted the values of λ for modes with one nodal circle and several values of n and for increasing values of G, keeping Ω=200 throughout. The membrane geometry is defined by α=0.1 and the Poisson's ratio is ν=0.34.

For the first two values $n = 0, 1$ the eigenvalue increases monotonically with Ω and hence it never becomes zero. For all other modes, the eigenvalue reaches zero at some value of G, hence providing the buckling load associated with each particular value of n. For each value of Ω, the critical value of G corresponds to the lowest intersection with the axis $\lambda = 0$. As such, $G_{crit} = 1.66 \times 10^6$ and $n_{crit} = 22$.

Figure 2.9a and Figure 2.9b show two additional cases at Ω=0 and Ω=64. We can notice the inversion of the curves as we increase Ω. We find that the critical gravity level and wave numbers are 40 and 2 for Ω=0 and 6.6$\times 10^4$ and 10 for Ω=64.

Finally the critical wave numbers for two different membrane geometries, $\alpha = 0.1$ and $\alpha = 0.7$, and

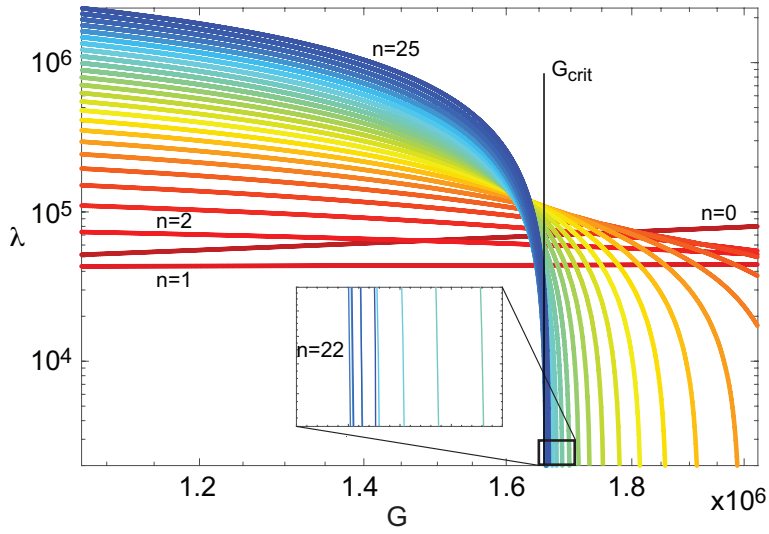

Figure 2.8: Variation of eigenvalues with G, for Ω=200, α=0.1, and ν=0.34. Note that $G_{crit} = 1.66 \times 10^6$ and $n_{crit} = 22$.

$\nu = 0.34$ have been plotted in Figure 2.10, and the buckling mode shape for each value of Ω is also shown. The corresponding values of Ω_{crit} are not shown. Note that the waviness of the critical buckling mode increases with increasing Ω.

2.3.4 Discussion

A physical interpretation of the buckling behavior of thin membranes can be obtained from simple energy arguments. Consider a rigid bar pinned at the top and loaded by gravity. If the support starts rotating at uniform angular velocity about a vertical axis, the bar is in equilibrium at an angle to the vertical. The value of this angle is determined by the balance between gravity and centrifugal (D'Alembert) forces. Next, consider a thin circular membrane, held at the center and spinning around a vertical axis through this point. In analogy to the rigid bar, it wants to take up an axisymmetric, near-conical configuration, which provides stationary potential energy due to centrifugal force and gravity. This configuration requires the outer perimeter of the membrane to get shorter, and this shortening induces in-plane strain energy in the membrane. When this energy is too high, the membrane can find an alternative equilibrium shape around the cone, by creating a wavy configuration with lower energy. The waves in the buckled configuration increase the bending energy of the membrane while releasing some of the in-plane energy. Because the bending energy of the wrinkled membrane increases with both bending stiffness and wave number, membranes with higher bending stiffness need fewer waves to achieve the same amount of internal energy, which explains why at lower Ω the wave number is smaller.

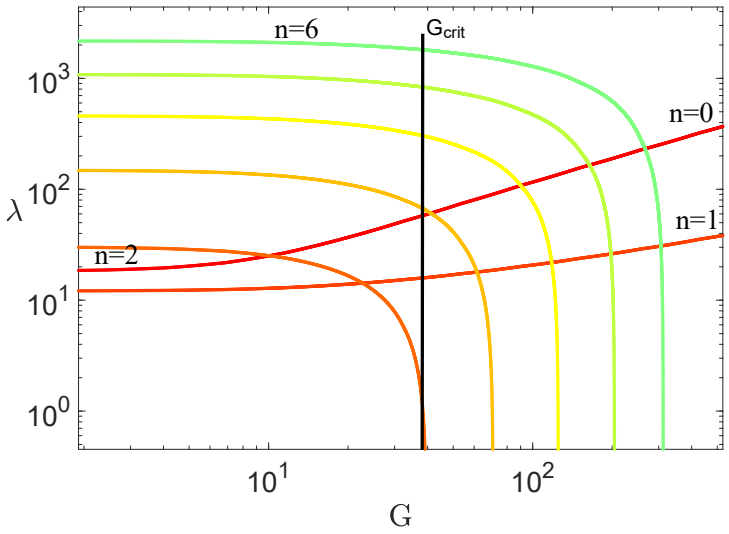

(a) Eigenvalues at Ω=0 and for increasing G.

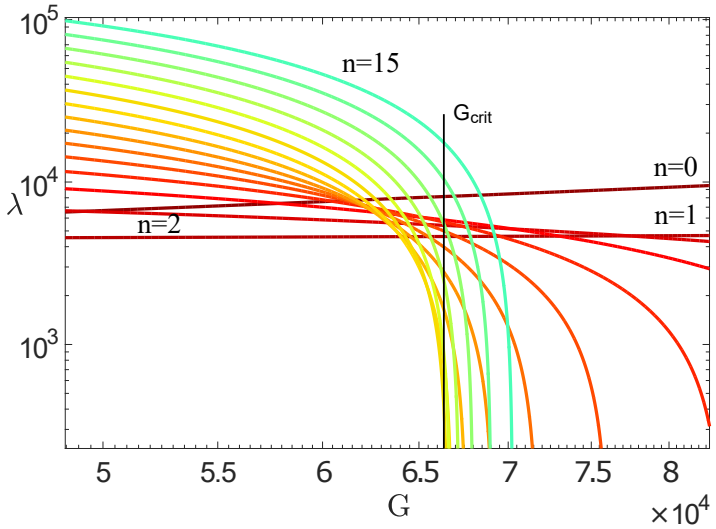

(b) Eigenvalues at Ω=64 and for increasing G.

Figure 2.9: Eigenvalues inversion.

In Figure 2.8 it is important to note that the eigenvalue vs. loading curves become tightly bunched and hence there are many values of n close to G_{crit}. It can be expected that it will be more difficult to identify a single buckling mode shape experimentally.

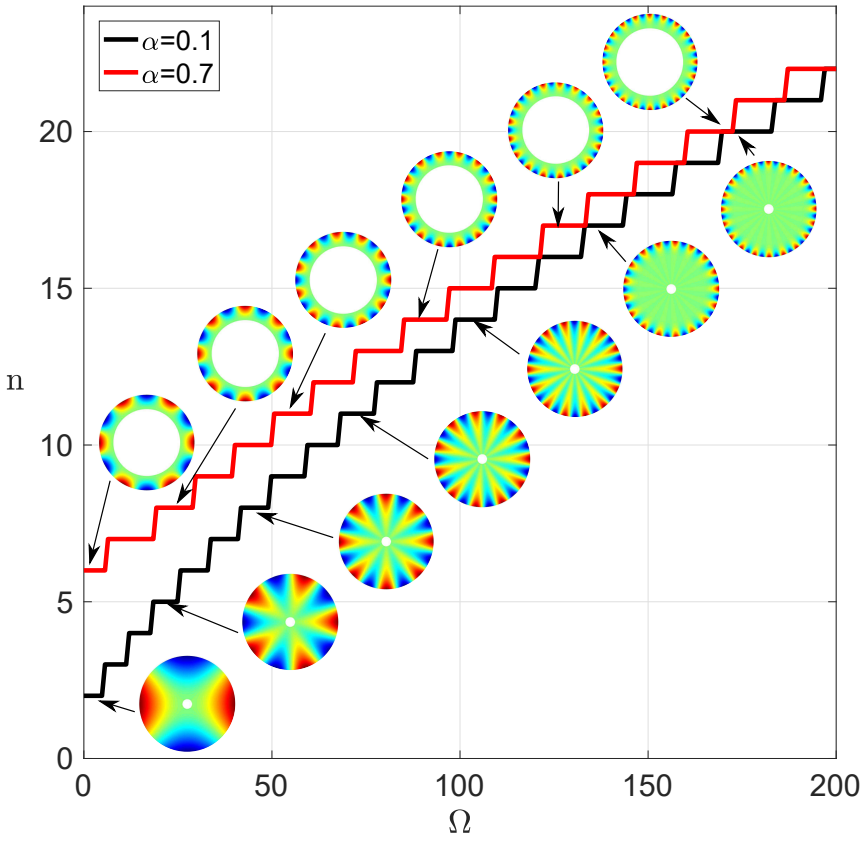

Figure 2.10: Variation of critical mode wave number and mode shapes with normalized angular velocity, for $\nu = 0.34$, and for α=0.1, and $\alpha = 0.7$.

2.3.5 Parametric Analysis

We have presented so far results for a wide range of Ω and G but fixed α and ν. In this section, we present results for various α and ν, to study the influence of these parameters on the stability of the spinning membrane.

We wrote a Python script in Abaqus that computes the critical loads and wave numbers. A similar technique can be used to estimate the buckling of many problems that requires a nonlinear loading path. Abaqus has a built-in buckle option, but it is a linear perturbation analysis that doesn't follow the nonlinear loading path. We have used this script to develop results on a wide range of dimensionless G and Ω.

The membrane is simulated with a linear elastic material with the properties of Kapton film. The simulation is carried out with S4R elements: 4-node doubly curved thin shell elements with reduced integration, hourglass control, finite membrane strains, 5 thickness integration points elements. They are numerically efficient elements based on the Kirchhoff shell theory. We simulate the central hub by rigidly constraining

the nodes along the inner edge. As the wrinkling is triggered by to compression at the outer edge where the wrinkles are localized at high angular velocity, it is important to have a fine mesh at that edge. A dense mesh was used with 1000 nodes on the outer edge and 1000α on the inner edge. The simulation runs in two steps. First, a nonlinear static step evaluates the axisymmetric equilibrium of the membrane under centrifugal force and gravity. Then, a frequency analysis is performed. A secant method algorithm was used to determine the gravity load that leads to the first zero eigenvalue for each Ω. The wrinkle wave number is automatically computed using the Fourier transform of the outer edge deflection of the first mode. The results from this script and the MATLAB code were compared for α=0.1 and ν=0.34 and gave the exact same results for the full range Ω=[0...200].

With this script we evaluated the master curves shown in Figure 2.11. We have looked into the depen-

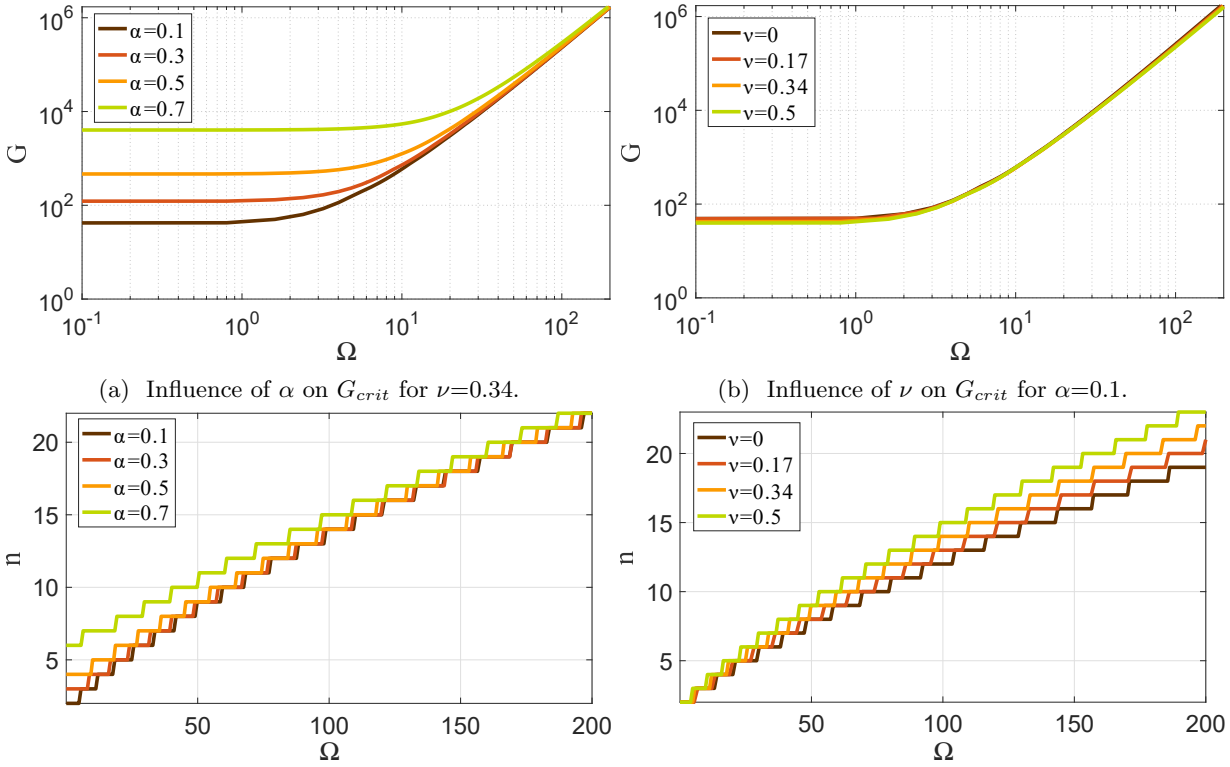

(a) Influence of α on G_{crit} for ν=0.34.

(b) Influence of ν on G_{crit} for α=0.1.

(c) Influence of α on n_{crit} for ν=0.34.

(d) Influence of ν on n_{crit} for α=0.1.

Figure 2.11: Influence of α for ν=0.34, and of ν for α=0.1 on critical loads (G,Ω).

dence of the critical load on geometric parameters and material properties, using nonlinear finite element simulations to compute the relationship between G_{crit}, n_{crit} and Ω_{crit}. Figure 2.11a and Figure 2.11b plot the influence of α (for ν=0.34) and ν for (α=0.1) on G_{crit}. These plots show that ν has little influence on the critical load, while increasing α has the effect of increasing G_{crit} for given Ω, or decreasing Ω_{crit} for given G. Figure 2.11d shows the influence of ν on critical wave number for α=0.1. Increasing Poisson's ratio

ν increases the wave number for a given Ω. Increasing α at constant ν (Figure 2.11c) increases the wave number as well but at higher Ω the wave numbers converge to each other.

2.4 Comparison of Present Theory with Membrane Theory, Nonlinear Simulations, and Experiments

Figure 2.12 shows a comparison of results from the present theory with the membrane theory by Simmonds (1962a), nonlinear finite element simulations, and the experimental results obtained in the present study. According to the pure membrane wrinkling theory (Section 2.3.1) G_{crit} is proportional to Ω^3, and the

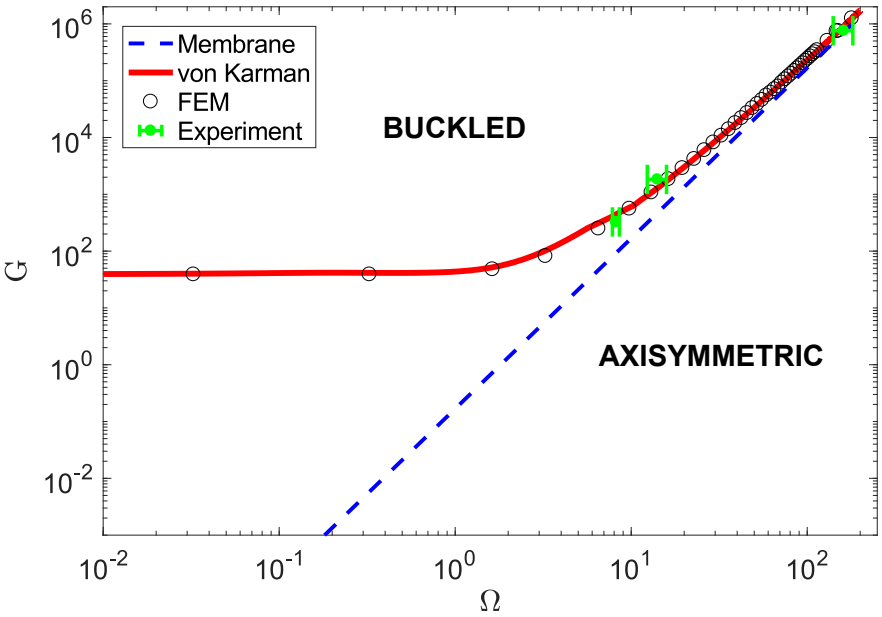

Figure 2.12: Comparison between buckling theory introduced in this paper, membrane theory derived by Simmonds, finite element simulations and experiments.

coefficient of proportionality decreases with both α and ν. This theory does not resolve the waviness of the buckled mode shape. Figure 2.12 shows that the two theories converge at high values of Ω, which was expected since the effect of the bending stiffness of the membrane tend to become negligible.

Our collaborators, Prof. John Elie Sader and Dr. Debadi Chakraborty, have performed nonlinear static finite element simulations using a COMSOL model consisting of three-dimensional elements. The full 3D membrane was modeled in the finite element software COMSOL Multiphysics using its nonlinear static solver. An incremental gravitational load is applied on a clamped-free membrane, which is rotating at a fixed speed. Then the critical value of G as a function of Ω is calculated by monitoring the buckling point of the spinning membrane. They use the same boundary conditions as used in the analytical model. The reported results

for the spinning membrane consist of 6873 tetrahedral solid elements. The membrane was first loaded with a centrifugal force field, then gravity was applied in small increments up to the loss of stability. They started from different angular velocities and computed the corresponding gravity amplitudes that lead to instability. The results of this analysis are plotted as black circles in Figure 2.12, and they practically coincide with the results from the present theory, across the full range of Ω. It is interesting to note that even if the von Kármán equations are an approximation to the three-dimensional nonlinear elastic model, and are normally assumed to be valid for deflections on the order of the plate thickness, in the present case they give excellent results for large deflections. For $\Omega = 10,\ 200$ the edge deflections just before buckling are respectively $4.5h$, $55\ h$.

We have also plotted, in green in Figure 2.12, the critical pairs (G, Ω) for our three experiments. There is excellent agreement between the critical angular velocities from experiments and theory. However, the theoretical buckling wave numbers are 3, 4, and 18 respectively for Al-13, Al-20, and Ka-20, whereas our experiments gave the values 3, 3, and 12 (see Table 2.2). As noticed in Section 2.3.3 the buckling limits tend to become quite close at higher values of Ω, and it is conjectured that this effect, in combination with initial curvature of the Kapton membrane, may explain why the theoretically obtained wave number is less accurate for the dimensions of the test sample Ka-20.

Sample	Al-13	Al-20	Ka-20
n number exp.	3	3	12
n number theo.	3	4	18
ω_{crit} exp. (rpm)	1100	800	783
ω_{crit} simu. (rpm)	1050	921	730

Table 2.2: Comparison between experiments and theory.

2.5 Spin Down

Upon further spin down, each experiment showed additional shape transitions of the membranes, to lower values of n. Select shapes are shown in Figure 2.13 for Ka-20, Figure 2.14 for Al-20, and Figure 2.15 for Al-13.

A very interesting observation is that the buckling mode transitions seen in the experiments, upon spin down, resemble the theoretical staircase pattern in Figure 2.10. Therefore, it is natural to ask if there might be an exact correspondence between the angular velocities at which the mode transitions occur. To investigate this point, we compared the experimentally observed velocities of the various transitions for Ka-20 to the theoretical. We can see Figure 2.16 a clear discrepancy between the two results.

To determine whether the discrepancy might be due to experimental errors, we also carried out a FEM

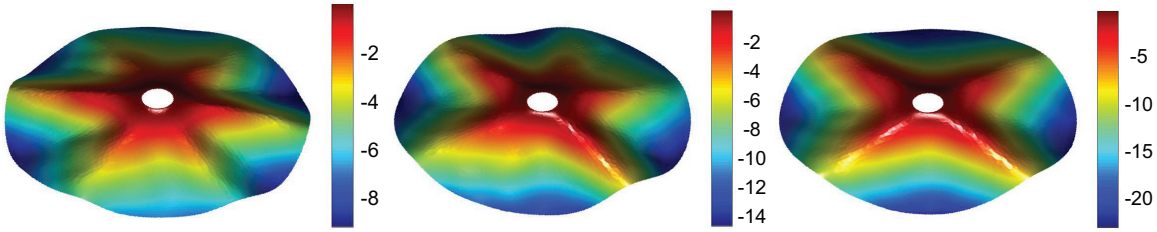

(a) Ka-20, ω=356 rpm. (b) Ka-20, ω=289 rpm. (c) Ka-20, ω=230 rpm.

Figure 2.13: Selected spin-down shapes of Ka-20 membrane. Deflection units are mm.

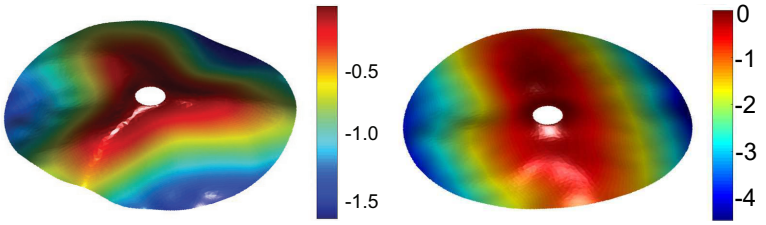

(a) Al-20, ω=700 rpm. (b) Al-20, ω=255 rpm.

Figure 2.14: Selected spin-down shapes of Al-20 membrane. Deflection units are mm.

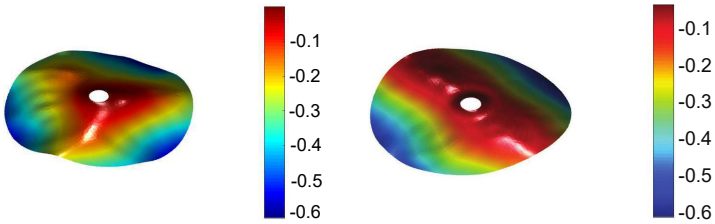

(a) Al-13, ω=950 rpm. (b) Al-13, ω=650 rpm.

Figure 2.15: Selected spin-down shapes of Al-13 membrane. Deflection units are mm..

simulation of the spin-down process for a membrane with perfect geometry. The simulation was performed in Abaqus/Standard and the membrane model is similar to the one Section 2.3.5. Nonlinear dynamic implicit integrations was performed in a membrane-mounted (spinning) reference frame. In order to simulate the slow spin down, we run a quasi-static simulation with centrifugal load. As the deceleration is slow we neglect the rotary acceleration fictitious force. Finally as the material displacement is mainly out of plan and thus parallel to the axis of rotation, Coriolis force is neglected as well. We used the Euler-Backward integration scheme. The simulation is performed in three steps. First, we add centrifugal force corresponding to a spin rate of 1000 rpm in a nonlinear static step. Once the structure is stiff enough to sustain gravity we add a gravity load of amplitude 9.81 $m.s^{-2}$ in another nonlinear static step. Finally we perform a quasi-static simulation by linearly decreasing the centrifugal force up to 0 rpm with a maximum time increment of 0.5 rpm to have a small enough resolution in angular velocity. The results are presented in Figure 2.16.

The same qualitative dynamic behavior as the one observed experimentally is seen. It is characterized

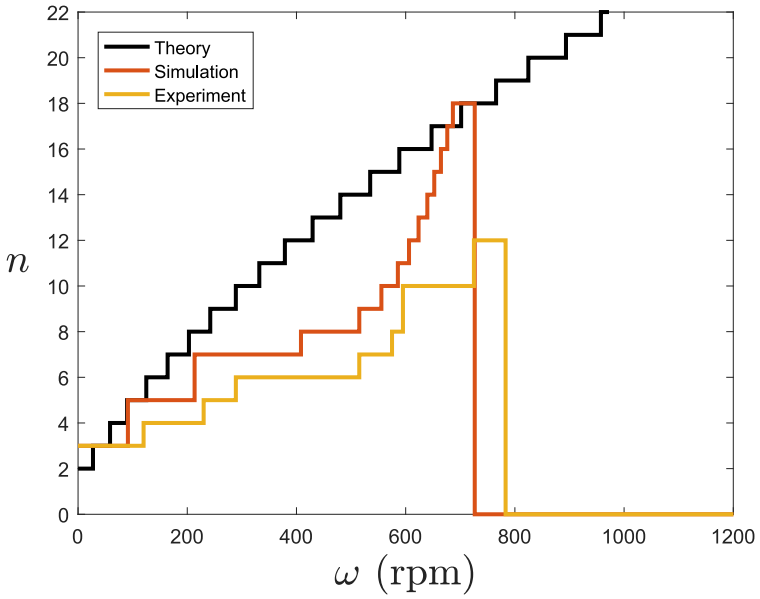

Figure 2.16: Comparison of mode shape wave number predicted by buckling theory, with mode transitions from spin down experiments and numerical simulations.

by a series of successive shape instabilities, as the membrane surface is deformed into a wavy shape with an increasing number of rotationally symmetric waves. We show some of the simulated equilibrium shapes in Figure 2.17. We find a perfect match both in terms of critical wave number and critical buckling Ω between theory and simulation for the first critical speed, which is the only one we intended to describe exactly. We again found that the shape transitions upon spin down do not occur at the critical angular velocities. The full spin down prediction requires some additional work to estimate the post-buckling equilibrium and its successive bifurcations, that is not the purpose of this study. For example Chen and Fang (2011) has derived such analytical solutions. In particular, the authors show that spin up and down exhibit some hysteresis and overall the equilibrium shapes post buckling are path dependent.

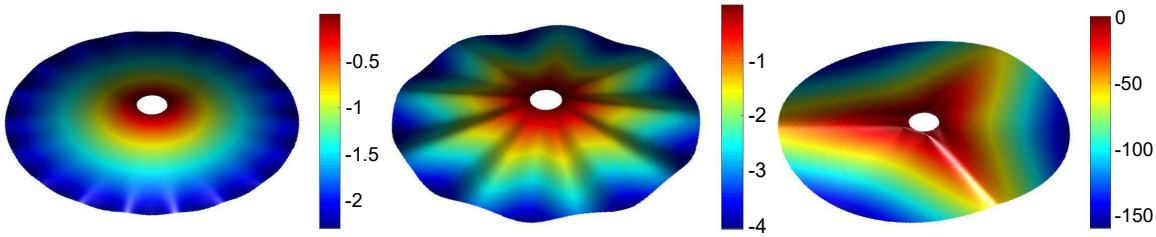

(a) Ω= 707 rpm. (b) Ω= 525 rpm. (c) Ω= 0 rpm.

Figure 2.17: Selected post buckling equilibrium shapes. Deflection units are mm.

2.6 Application to Spinning Spacecraft

Our theory can be used to analyze novel designs of ultralight spacecraft. Consider a circular spinning membrane in space with a perfectly absorbent surface that is pointed to the sun, in geostationary orbit. It provides an ideal light-collecting surface to gather solar energy.

Let the radius be $r = 10$ m, the thickness $h = 100$ μm, and the Young's modulus and Poisson's ratio be identical to Kapton (see Table 2.1). This choice is made for simplicity, since the photovoltaic material has not been specified. The magnitude of the solar pressure in geostationary orbit is $q_0 = 4.57 \times 10^{-6}$ Pa.

For these properties, $G = 1.2 \times 10^5$ and then the minimum non-dimensional rotation speed to avoid buckling is Ω_{crit}=79 which corresponds to $\omega = 1.3$ rpm.

2.7 Conclusion

Transverse uniform body forces acting on a spinning membrane induce deflections much greater than the membrane thickness, and these deflections are associated with a compressive hoop stress around the edge of the membrane. This hoop stress can buckle the membrane, resulting in a series of azimuthal wrinkles.

A general formulation of the problem has been presented, in terms of the dimensionless load G and dimensionless angular velocity Ω, defined in Equation 2.51, and the critical values of G and Ω have been plotted in Figure 2.12. For $\Omega < 1$, G_{crit} depends only on the bending stiffness of the membrane (bending dominated behavior), and hence it is constant with G. For $\Omega > 10$, we recover the results of the membrane theory, namely, wrinkling depends only on the mid-plane stress, and hence G increases with the cube of Ω (in-plane dominated behavior). Both of these specific numerical limits increase if the ratio between inner and outer radius of the membrane, α, is increased.

The buckling eigenvalues and the corresponding eigenmodes of the spinning membrane have been plotted for a specific value of Ω in Figure 2.8. The figure shows that all eigenvalues for $n \geq 2$ decrease when Ω increases. The wrinkling mode of the membrane is determined by which eigenvalues reaches zero first. The variation of the azimuthal wave number of the critical buckling mode for a specific value of Ω has been plotted in Figure 2.10. It has been observed, both in experiments and through numerical simulations, that the wrinkling mode changes during spin down of the membrane. This behavior, plotted in Figure 2.16, qualitatively resembles the critical mode variation corresponding to different Ω.

Chapter 3

Nonlinear Vibration at Axisymmetric Resonance of Deflected Spinning Plates

3.1 Introduction

Membranes structures are a promising concept for large space structures, as they are light and allow for tight packaging for launch. For many applications, surface flatness is a key design parameter and understanding the dynamics of such very flexible structures is a prerogative to the success of a mission. In this chapter we study the influence a transverse uniform load induced deflection of the spinning membrane on its dynamics. In particular we focus on the nonlinear vibration at a resonance frequency of an axisymmetric mode.

Extensive work has been performed on the mathematical description of thin spinning disks. The linear vibration modes have been studies by Eversman (1968); Simmonds (1962b); Barasch and Chen (1972). Nowinski (1964) formulated the problem analytically using von Kármán plate equations. In the context of spinning disks with a stationary concentrated transverse load (memory disk drives), Renshaw and Mote (1996); Renshaw (1998) presented some results on the critical speed and the stability of spinning disks near critical speeds. Additionally, Renshaw and Mote (1995) investigated the stability of the deflected flexible disk due to a stationary concentrated transverse load and provided a mathematical derivation. The nonlinear vibration of the structure excited by a concentrated stationary load were analyzed by Nayfeh (2000) as well as Raman and Mote (1999); Torii and Yasuda (1998); Tobias and Arnold (1957) and a reduced order model was proposed.

In the context of spinning heavy disks, some work has been performed on the equilibrium deflection and buckling limits, as reported in the literature review of Chapter 2. To our knowledge there is no work on the nonlinear vibration of deflected membranes under transverse uniform load and excited axisymmetrically. This work studies the fundamentals of the influence of the deflection on the equivalent spinning membrane

oscillator. It describes the response to the spinning system to a periodic excitation at a frequency matching the natural axisymmetric frequencies of the structure.

Limited experimental studies have been performed on membrane-like structures for space applications. Linear vibration measurements were performed by Okuizumi (2014). Most of the experimental work found in the literature was performed on spinning memory disks by exciting them it a fixed point in space with electromagnetic actuators, as presented by Raman and Mote (1999, 2001).

A circular isotropic clamped-free membrane stabilized by its spinning motion is studied here. Its response to external excitations is analyzed using a reduced order model, simulations, and experiments. Deflections have important effects on the nonlinear behavior of the membrane measured in the experiments. A reduced order model that includes the effects of deflection is discussed in this chapter. The influence of a transverse uniform load can be studied by spinning the membrane about a vertical axis at various angular velocities in Earth gravity. A softening nonlinear behavior is observed at lower angular velocities, while hardening appears at higher angular velocities. In the first part of this chapter, we derive the full theoretical model and reduced order model, then present results for a wide range of parameters. In the second part we present full finite element nonlinear dynamic simulations in Abaqus/Standard and compare with theory. Finally, we present an experimental setup and some results on frequency sweep and compare with theory. Figure 3.1 introduces the notation used in this chapter and shows the studied configuration.

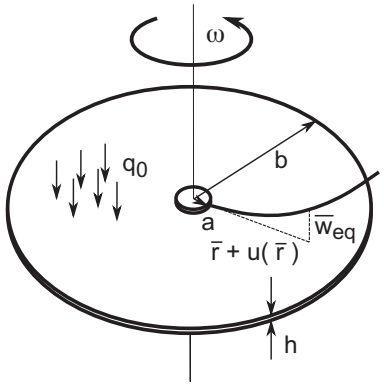

Figure 3.1: Notations

3.2 Theory

In this section we develop a reduced order model for the nonlinear vibration of lightly damped, lightly excited spinning membranes deflected by a transverse uniform load, and excited at a resonant frequency of an axisymmetric mode shape. To study the influence of the transverse uniform load induced deformation on the dynamical behavior of the structure, we compare the behavior of the membrane with and without

deflection, for a wide range of non-dimensional parameters. First we formulate the problem, describe the hypothesis, and formulate the equilibrium and perturbation equations. Then we introduce a reduced order model to describe the nonlinear oscillator due to excitations at axisymmetric resonance frequencies. We find that in those conditions the spinning membrane behaves like a Helmholtz-Duffing oscillator.

3.2.1 Problem Formulation

Nowinski (1964) derived the von Kármán-type plate equations for axisymmetric circular rotating plates. They assume an isotropic elastic plate and are based on the von Kármán plate theory that requires small stretch and moderate rotation. The deflection $\bar{w}$ and stress function $\bar{\Phi}$ must satisfy the following coupled nonlinear equations:

$$\begin{aligned} \rho h \frac{\partial^2 \bar{w}}{\partial \bar{t}^2} + D\nabla^4 \bar{w} &= L(\bar{w}, \bar{\Phi}) - \bar{c}\frac{\partial \bar{w}}{\partial \bar{t}} - \omega^2 \rho h (\frac{1}{2}\bar{r}^2 \nabla^2 \bar{w} + \bar{r}\frac{\partial \bar{w}}{\partial \bar{r}}) + \bar{q}(\bar{r}, \theta, \bar{t}) \\ \nabla^4 \bar{\Phi} &= -\frac{1}{2} EhL(\bar{w}, \bar{w}) + 2\rho h(1-\nu)\omega^2 \end{aligned} \tag{3.1}$$

where $\bar{q}(\bar{r}, \theta, \bar{t})$ is a transverse load, $\bar{c}$ is the damping coefficient, ρ is the density, E is the Young's modulus, ν is Poisson's ratio, and the rest of the quantities are defined Figure 3.1. The operator L is defined as:

$$L(\bar{w}, \bar{\Phi}) = \frac{\partial^2 \bar{w}}{\partial \bar{r}^2}(\frac{1}{\bar{r}}\frac{\partial \bar{\Phi}}{\partial \bar{r}} + \frac{1}{\bar{r}^2}\frac{\partial^2 \bar{\Phi}}{\partial \theta^2}) + \frac{\partial^2 \bar{\Phi}}{\partial \bar{r}^2}(\frac{1}{\bar{r}}\frac{\partial \bar{w}}{\partial \bar{r}} + \frac{1}{\bar{r}^2}\frac{\partial^2 \bar{w}}{\partial \theta^2}) - 2(\frac{1}{\bar{r}}\frac{\partial^2 \bar{\Phi}}{\partial \bar{r}\partial \theta} - \frac{1}{\bar{r}^2}\frac{\partial \bar{\Phi}}{\partial \theta})(\frac{1}{\bar{r}}\frac{\partial^2 \bar{w}}{\partial \bar{r}\partial \theta} - \frac{1}{\bar{r}^2}\frac{\partial \bar{w}}{\partial \theta}) \tag{3.2}$$

The boundary conditions are free on the outer edge and clamped on the inner edge (written in nondimensional form in Equations 3.6, 3.8, 3.9, and 3.10).

We are interested in studying the fundamental question: how will the axisymmetric deflection of the membrane due to transverse uniform load affect the nonlinear axisymmetric oscillations of the structure?

We write the external load $\bar{q}(\bar{r}, \theta, \bar{t})$ as the sum of a uniform transverse load $\bar{q}_0 = \rho g h$ and a perturbation $\bar{q}(r, \theta, t) = \bar{q}_0 + \bar{p}(r, \theta, t)$. Let us consider a deflection and stress function $\left(\bar{w}_{eq} + \bar{w}, \bar{\Phi}_{eq} + \bar{\Phi}\right)$ as the sum of the equilibrium $\left(\bar{w}_{eq}, \bar{\Phi}_{eq}\right)$, and a perturbation $\left(\bar{w}, \bar{\Phi}\right)$ due to a perturbation force $\bar{p}(\bar{r}, \theta, \bar{t})$. Then we introduce the dimensionless parameters Equation 3.3. These differ from the ones introduced by Nayfeh (2000) as, in our case of a very thin membrane, the prestress due to centrifugal force dominates over the bending stiffness. For the equilibrium quantities we use the same dimensionless parameters as the ones introduced in Chapter 2.

Equilibrium:

$$\begin{aligned} r &= \frac{\bar{r}}{b} & \alpha &= \frac{a}{b} \\ w_{eq} &= \frac{\bar{w}_{eq}}{h} & \Phi_{eq} &= \frac{\bar{\Phi}_{eq}}{D} \\ \Omega &= \sqrt{\frac{\rho h}{D}} b^2 \omega & G &= \frac{b^4}{Dh} \bar{q}_0 \end{aligned} \tag{3.3}$$

Perturbation:

$$\begin{aligned} c &= \frac{b^3 \bar{c}}{2\sqrt{\rho h^3 D}} & w &= \frac{\bar{w}}{h\Omega} \sqrt{\frac{b}{h}} \\ \Phi &= \frac{\bar{\Phi} b}{Dh\Omega^2} & p &= \frac{b^4 \bar{p}}{Dh\Omega^3} \left(\frac{b}{h}\right)^{3/2} \end{aligned} \tag{3.4}$$

We are looking for solutions that approximate the exact solution for very thin plates and thus in the case where $\frac{h}{b}$ tends to zero. All the non dimensional parameters Equations 3.3 and 3.4 are assumed to be $\mathcal{O}(1)$. This is going to be compared against experimental results in Section 3.4.4.2.

3.2.1.1 Equilibrium

The dimensionless equilibrium equations are:

$$\begin{aligned} \nabla^4 w_{eq} &= L(w_{eq}, \Phi_{eq}) - \Omega^2 (\frac{1}{2} r^2 \nabla^2 w_{eq} + r \frac{\partial w_{eq}}{\partial r}) + G \\ \nabla^4 \Phi_{eq} &= -6\left(1-\nu^2\right) L(w_{eq}, w_{eq}) + 2(1-\nu)\Omega^2 \end{aligned} \tag{3.5}$$

In non dimensional form, the boundary conditions leads to:
Clamped at r=α:

$$w_{eq} = 0 \qquad \frac{\partial w_{eq}}{\partial r} = 0 \tag{3.6}$$

$$u = 0 \qquad v = 0; \tag{3.7}$$

The two last conditions on the displacement u and v can be written in terms of the stress function following

Nayfeh (2000):

$$\frac{\partial^2\Phi_{eq}}{\partial r^2}-\nu(\frac{1}{r}\frac{\partial\Phi_{eq}}{\partial r}+\frac{1}{r^2}\frac{\partial^2\Phi_{eq}}{\partial\theta^2})-\frac{(1-\nu)}{2}\Omega^2r^2=0$$
$$\frac{\partial^3\Phi_{eq}}{\partial r^3}+\frac{1}{r}\frac{\partial^2\Phi_{eq}}{\partial r^2}-\frac{1}{r^2}\frac{\partial\Phi_{eq}}{\partial r}+\frac{2+\nu}{r^2}\frac{\partial^3\Phi_{eq}}{\partial r\partial\theta^2}-\frac{3+\nu}{r^3}\frac{\partial^2\Phi_{eq}}{\partial\theta^2}-(1-\nu)\Omega^2r=0 \tag{3.8}$$

Free at r=1:

$$\frac{\partial}{\partial r}\nabla^2w_{eq}+\frac{(1-\nu)}{r^2}\frac{\partial^2}{\partial\theta^2}(\frac{\partial w_{eq}}{\partial r}-\frac{w_{eq}}{r})=0 \qquad \frac{\partial^2w_{eq}}{\partial r^2}+\nu(\frac{1}{r}\frac{\partial w_{eq}}{\partial r}+\frac{1}{r^2}\frac{\partial^2w_{eq}}{\partial\theta^2})=0 \tag{3.9}$$
$$\frac{1}{r}\frac{\partial\Phi_{eq}}{\partial r}+\frac{1}{r^2}\frac{\partial^2\Phi_{eq}}{\partial\theta^2}-\frac{1}{2}\Omega^2r^2=0 \qquad -\frac{1}{r}\frac{\partial^2\Phi_{eq}}{\partial r\partial\theta}+\frac{1}{r^2}\frac{\partial\Phi_{eq}}{\partial\theta}=0 \tag{3.10}$$

The equilibrium shape of spinning membranes under uniform normal load has been previously studied by Simmonds (1962a), and Okuizumi (2007). Both the authors used the membrane approximation, whereas we use the full nonlinear plate equations 3.1. We only consider here the vibration around axisymmetric equilibrium shapes that do not hold when buckling occurs. As shown in Chapter 2, when the membrane deflects due to gravity loading a compressing stress develops at the outer edge and leads to wrinkles. The dimensionless critical load G depends on the dimensionless angular velocity Ω, the Poisson's ratio ν, and hub to membrane ratio α. The higher the Ω parameter, the higher the buckling load G. This imposes a minimal angular velocity:

$$\Omega > f_b(G,\alpha,\nu) \tag{3.11}$$

The other limit of the approach is plasticity. For high angular velocities some plastic deformation can occur. If we consider the stress due to centrifugal load only and following the Von Mises criteria for plane stress, the plasticity limits depend on the dimensionless yield strength, ν and α. This imposes an upper bound for the angular velocity:

$$\Omega < \sqrt{\sigma_y}f(\alpha,\nu) \tag{3.12}$$

where σ_y is the dimensionless yield strength of the material.

3.2.1.2 Perturbation

We first derive the perturbation equations with dimensions. After introducing the perturbation in the spinning plate dynamic Equations 3.1, taking into account that L is a bi-linear symmetric operator, and

simplifying using the equilibrium Equation 3.5, we obtain:

$$\rho h\frac{\partial^2\bar{w}}{\partial\bar{t}^2}+D\nabla^4\bar{w}+\rho h\omega^2\left(\frac{1}{2}\bar{r}^2\nabla^2\bar{w}+\bar{r}\frac{\partial\bar{w}}{\partial\bar{r}}\right)-L(\bar{w},\bar{\Phi}_{eq})=L(\bar{w}_{eq},\bar{\Phi})+L(\bar{w},\bar{\Phi})-c\frac{\partial\bar{w}}{\partial\bar{t}}+\bar{p}(\bar{r},\theta,\bar{t})$$

$$\nabla^4\bar{\Phi}=-\frac{1}{2}Eh(2L\left(\bar{w}_{eq},\bar{w}\right)+L\left(\bar{w},\bar{w}\right)) \tag{3.13}$$

Using the dimensionless quantities Equations 3.3 and 3.4, we obtain:

$$\frac{\partial^2 w}{\partial t^2}+\nabla^4 w+\Omega^2\left(\frac{1}{2}r^2\nabla^2 w+\bar{r}\frac{\partial w}{\partial r}\right)-L(w,\Phi_{eq})=$$

$$\Omega\sqrt{\epsilon}L(w_{eq},\Phi)+\Omega^2\epsilon L(w,\Phi)-2c\epsilon\frac{\partial w}{\partial t}+\Omega^2\epsilon p(r,\theta,t) \tag{3.14}$$

$$\nabla^4\Phi=-\frac{6\left(1-\nu^2\right)}{\Omega}\left(\frac{2}{\sqrt{\epsilon}}L\left(w_{eq},w\right)+\Omega L\left(w,w\right)\right) \tag{3.15}$$

where ϵ naturally appears as a small perturbation parameter:

$$\epsilon=\frac{h}{b} \tag{3.16}$$

Let us write:

$$\Phi=-\frac{6\left(1-\nu^2\right)}{\Omega}\left(\frac{2}{\sqrt{\epsilon}}\Phi_1+\Omega\Phi_2\right) \tag{3.17}$$

with:

$$\nabla^4\Phi_1=L\left(w_{eq},w\right)$$

$$\nabla^4\Phi_2=L(w,w) \tag{3.18}$$

then equation 3.14 simplifies to:

$$\frac{\partial^2 w}{\partial t^2}+\nabla^4 w+\Omega^2(\frac{1}{2}r^2\nabla^2 w+r\frac{\partial w}{\partial r})-L(w,\Phi_{eq})+12\left(1-\nu^2\right)L(w_{eq},\Phi_1)=$$

$$-6\left(1-\nu^2\right)\Omega\sqrt{\epsilon}\left(L(w_{eq},\Phi_2)+2L(w,\Phi_1)\right)-6\left(1-\nu^2\right)\Omega^2\epsilon L(w,\Phi_2)-2\epsilon c\frac{\partial w}{\partial t}+\epsilon\Omega^2 p(r,\theta,t) \tag{3.19}$$

where the left hand side is the linear part, the term multiplied by $\sqrt{\epsilon}$ is the quadratic part, and the term multiplied by ϵ is cubic. The boundary conditions for the perturbed deflection w are the same as before. The boundary conditions for the perturbed stress function Φ are:

in r=α

$$\frac{\partial^2\Phi}{\partial r^2} - \nu(\frac{1}{r}\frac{\partial\Phi}{\partial r} + \frac{1}{r^2}\frac{\partial^2\Phi}{\partial\theta^2}) = 0$$
$$\frac{\partial^3\Phi}{\partial r^3} + \frac{1}{r}\frac{\partial^2\Phi}{\partial r^2} - \frac{1}{r^2}\frac{\partial\Phi}{\partial r} + \frac{2+\nu}{r^2}\frac{\partial^3\Phi}{\partial r\partial\theta^2} - \frac{3+\nu}{r^3}\frac{\partial^2\Phi}{\partial\theta^2} = 0 \tag{3.20}$$

in r=1:

$$\frac{1}{r}\frac{\partial\Phi}{\partial r} + \frac{1}{r^2}\frac{\partial^2\Phi}{\partial\theta^2} = 0$$
$$-\frac{1}{r}\frac{\partial^2\Phi}{\partial r\partial\theta} + \frac{1}{r^2}\frac{\partial\Phi}{\partial\theta} = 0 \tag{3.21}$$

In the next part we apply a Galerkin procedure similar to that presented by Nayfeh et al. (2001); Raman and Mote (1999) to derive the reduced order model of weakly nonlinear oscillations on axisymmetric modes. In those references the authors consider a spatially fixed harmonic load. They find that the primary resonance of the asymmetric modes follows two nonlinear coupled second-order equations with cubic stiffness. They find that the long-term response is a traveling wave. Here we consider a deflected membrane and an axisymmetric excitation where the response has one degree of freedom. We will show that the response follows the Helmholtz-Duffing oscillator. We first write the perturbation equations around the equilibrium, then solve the eigenvalue problem, and finally incorporate a one degree of freedom ansatz in the nonlinear perturbation equations to derived the reduced order model of the membrane oscillations.

3.2.1.3 Nonlinear Behavior and Reduced Order Model

We consider a transverse perturbation at the hub:

$$p(r,\theta,t) = p_0 cos(2\pi f t) \tag{3.22}$$

Assuming no internal resonance between the directly excited mode and any other mode (Nayfeh et al., 2001; Raman and Mote, 1999), and in the presence of damping (material damping in space and remaining air in the vacuum chamber during our experiments, for example), all the other modes will decay with time. The long term response consists of the directly excited mode and takes the form:

$$w = \eta(t)W(r) \tag{3.23}$$

where $W(r)$ is the principal mode shape that satisfies the following equations obtained from the linear part of equations 3.19 and 3.15:

$$-\left(2\pi f_0\right)^2 W + \nabla^4 W + \Omega^2(\frac{1}{2}r^2\nabla^2 W + r\frac{\partial W}{\partial r}) = L(W,\Phi_{eq}) - 12\left(1-\nu^2\right)L(w_{eq},\Psi_1)$$
$$\nabla^4\Psi_1 = L\left(w_{eq},W\right) \tag{3.24}$$

where ω_0 is the non dimensional natural frequency, W and Ψ_1, respectively, satisfy the boundary conditions 3.6 , 3.9 and 3.20, 3.21, and W is normalized as:

$$\int_\alpha^1 rW^2 dr = 1 \tag{3.25}$$

Inserting 3.23 into 3.18, we obtain:

$$\Phi_1 = \eta\Psi_1$$
$$\Phi_2 = \eta^2\Psi_2 \tag{3.26}$$

with

$$\nabla^4\Psi_2 = L(W,W) \tag{3.27}$$

Inserting 3.23 into 3.19 and using the frequency equations 3.24 we obtain:

$$\ddot{\eta}W + \eta\left(2\pi f_0\right)^2 W = -\eta^2 6\left(1-\nu^2\right)\Omega\sqrt{\epsilon}\left(L\left(w_{eq},\Psi_2\right) + 2L\left(W,\Psi_1\right)\right) -$$
$$\eta^3 6\left(1-\nu^2\right)\Omega^2\epsilon L\left(W,\Psi_2\right) - 2\epsilon c\dot{\eta}W + \epsilon\Omega^2 p\left(r,\theta,t\right) \tag{3.28}$$

Then, we project this equation onto W and simplify using equation 3.25. We also rescale the time with $2\pi f_0$ such that $t = 2\pi f_0 t$ and introduce the damping ratio ξ such that $c = \xi 2\pi f_0$. This leads to the following second order ODE that corresponds to the Helmholtz-Duffing oscillator.

$$\ddot{\eta} + 2\xi\epsilon\dot{\eta} + \eta + \sqrt{\epsilon}c_2\eta^2 + \epsilon c_3\eta^3 = \epsilon\phi p_0 cos(\Lambda t) \tag{3.29}$$

with the coefficients given by:

$$\begin{aligned}
\Lambda &= \frac{f}{f_0} \\
\xi &= \frac{c}{2\pi f_0} \\
c_2 &= \frac{6\left(1-\nu^2\right)\Omega}{\left(2\pi f_0\right)^2}\int_\alpha^1 \left(L\left(w_{eq},\Psi_2\right)+2L\left(W,\Psi_1\right)\right) rW dr \\
c_3 &= \frac{6\left(1-\nu^2\right)\Omega^2}{\left(2\pi f_0\right)^2}\int_\alpha^1 L(W,\Psi_2) rW dr \\
\phi &= \frac{\Omega^2}{\left(2\pi f_0\right)^2}\int_\alpha^1 rW dr
\end{aligned} \tag{3.30}$$

Overall, these coefficients depend on four dimensionless parameters: Ω, G, ν and α. Here, we consider α=0.1 and ν=0.34. In Figure 3.2 we show the influence of Ω on the coefficients c_2, c_3, ϕ and the frequency f_0 without transverse load G=0 and for G=1.35×10^5 (corresponding to the experimental case). It shows that the influence of gravity decreases with the angular velocity as the structure gets flatter. In addition, Figure 3.3 shows the influence of $G \in \left[0, 6.5\times10^5\right]$ and $\Omega \in [87, 400]$ for α=0.1 and ν=0.34. The blank region is the buckled region (see Chapter 2). As mentioned earlier, at high angular velocity the coefficients are not affected by gravity.

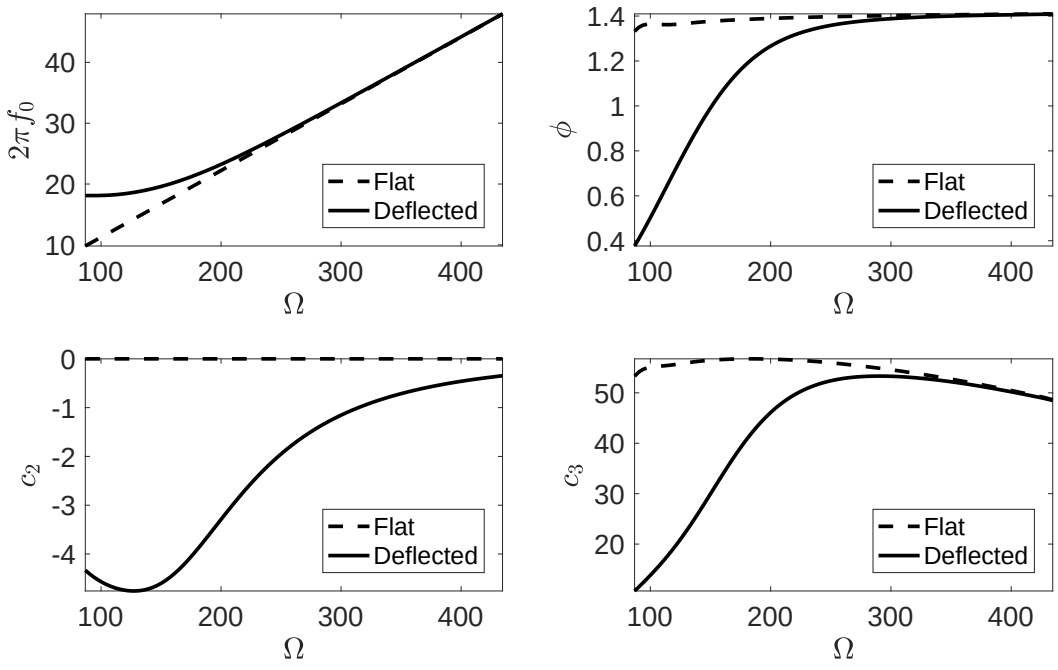

Figure 3.2: Nonlinear coefficients according to Ω for G=0, G=1.35×10^5, α=0.1 and ν=0.34.

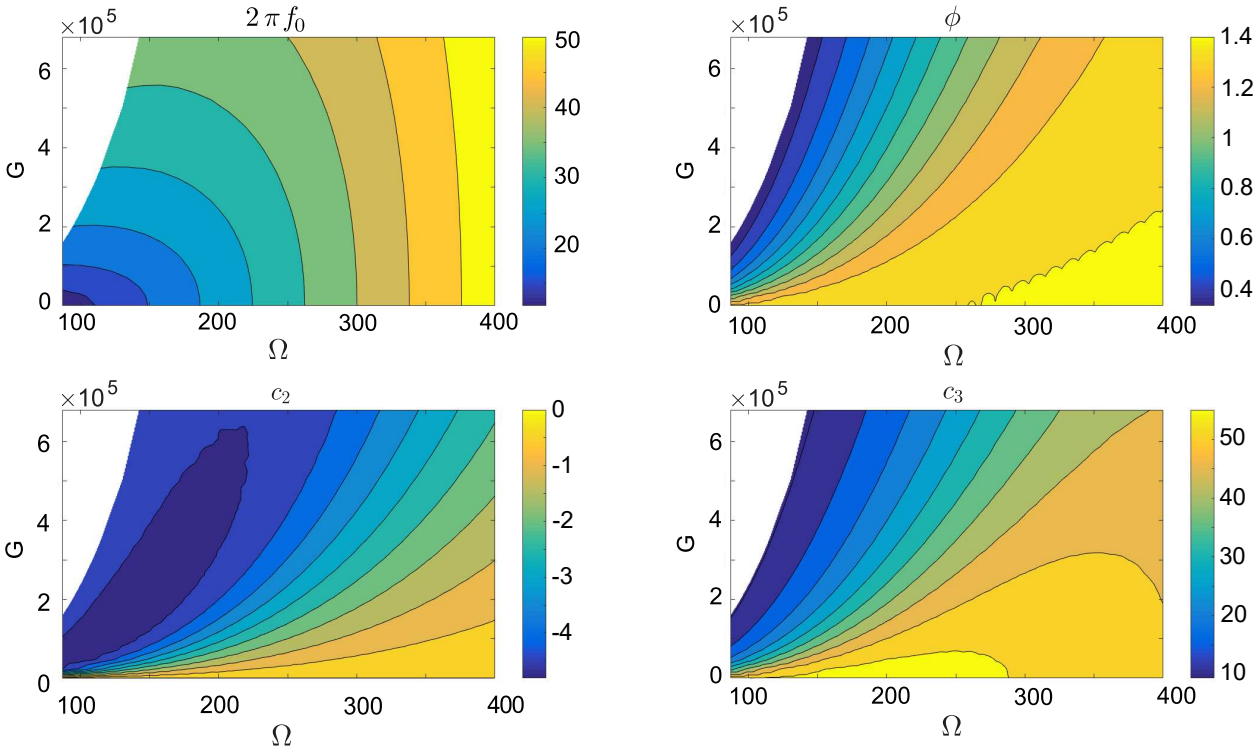

Figure 3.3: Influence of G and Ω on the coefficients f_0, ϕ, c_2, and c_3 for α=0.1 and ν=0.34. The white region corresponds to the buckled region.

3.2.2 Results from the Reduced Order Model

The Helmholtz-Duffing oscillator 3.29 has a restoring force with linear, quadratic, and cubic terms. The results from Nayfeh (2000), and Raman and Mote (1999) for a flat spinning plate, extended to the case of axisymmetric excitation, predict a Duffing oscillator (analysed by Holmes and Rand (1976) for example) with a linear and a quadratic term in the restoring form. Figure 3.2 shows that the coefficient of the quadratic term c_2 tends to zero as we increase the angular velocity and thus decreases deflection. The spinning membrane oscillator discussed here converges toward a Duffing oscillator, which is in agreement with the extension of the results of Nayfeh (2000), and Raman and Mote (1999).

Benedettini and Rega (1987); Rega et al. (1984) have extensively analyzed the solutions of the Helmholtz-Duffing oscillator in the context of elastic deflected cables under planar excitation. Studies on these oscillators are also reported by Kovacic and Brennan (2011). The equilibrium points of a general Helmholtz-Duffing oscillator 3.29 are η=0, and η=$\frac{-c_2 \pm \sqrt{c_2^2 - 4c_3}}{\sqrt{\epsilon} 2c_3}$. From the coefficients in the range shown in Figure 3.3 we find that the only physical solution is η=0 as $c_2^2 - 4c_3 < 0$. The deflected spinning membrane around axisymmetric resonance is thus described by a single-well potential and is referred to as a single-well Helmholtz-Duffing (SWHD) oscillator.

In the next two subsections we present the general solutions for the free and forced vibration and apply

them to a laboratory scale case. We then compare those results with FEM simulations (Section 3.3) and experimental results (Section 3.4). We consider a thin Kapton membrane in Earth gravity with dimensions and properties shown in Table 3.1, excited at the first axisymmetric frequency.

Young's modulus E	2.5 GPa
Poisson's ratio ν	0.34
Density ρ	1420 kg m^{-3}
Thickness h	50 μm
Outer radius b	13 cm
Inner radius a	1.3 cm
Gravity g	9.81 m.s^{-2}

Table 3.1: Membrane dimensions and material properties.

With these parameters, condition 3.11 becomes:

$$98 \text{ rad.}s^{-1} < \Omega < 4227 \text{ rad.}s^{-1} \tag{3.31}$$

3.2.2.1 Free Vibration

Benedettini and Rega (1987) derived the long term solutions of Helmholtz-Duffing oscillators using a fourth-order multiple scale perturbation method in the case of primary resonance, i.e., excitation close to the natural frequency. The steady state solution is characterized by an amplitude of vibration that depends on the excitation frequency (along with the phase that is not discussed here). They obtained the following equation for the backbone curve that describes the undamped free vibration at different initial amplitudes:

$$\Lambda_{bc} = 1 - c_4 a^2 - c_7 a^4 \tag{3.32}$$

where a is the amplitude of oscillation and c_4 and c_7 are defined as:

$$c_4 = \frac{5}{12}c_2^2 - \frac{3}{8}c_3 \tag{3.33}$$

$$c_7 = \frac{485}{1728}c_2^4 - \frac{173}{192}c_2^2 c_3 + \frac{15}{156}c_3^2 \tag{3.34}$$

At low amplitude of vibration, two behaviors characterize the vibration: hardening and softening. For hardening behavior the amplitude of vibration increases with increasing excitation frequency around resonance. For softening behavior the amplitude of vibration decreases with increasing excitation frequency. In particular, from Equation 3.32, we can estimate that, at small amplitudes of vibration, softening is observed for $c_4 > 0$, and hardening otherwise. Figure 3.4 shows the hardening and softening domains for a wide range of G and Ω, for α=0.1 and ν=0.34.

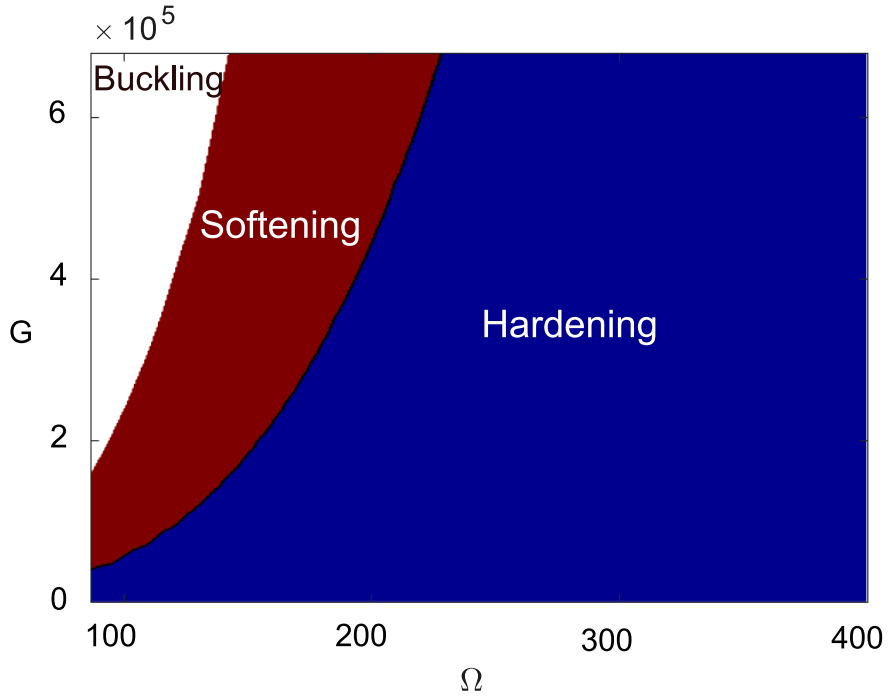

Figure 3.4: Softening (red) and hardening (blue) regions according to Ω and G for α=0.1 and ν=0.34.

Figures 3.5 and 3.6 show numerical solutions for the dimensions of the experiment (Table 3.1) and different angular velocities with and without deflection. Figure 3.5, corresponding to angular velocities close to the buckling point, shows the transition between softening at low angular velocities and hardening at high angular velocities. This effect is due to the quadratic stiffness term in the oscillator that comes from the deflection and thus the transverse load. At higher angular velocities (Figure 3.6), and low amplitude of deflection we notice that the transverse uniform load mainly influences the frequencies but the nonlinear behaviors are similar.

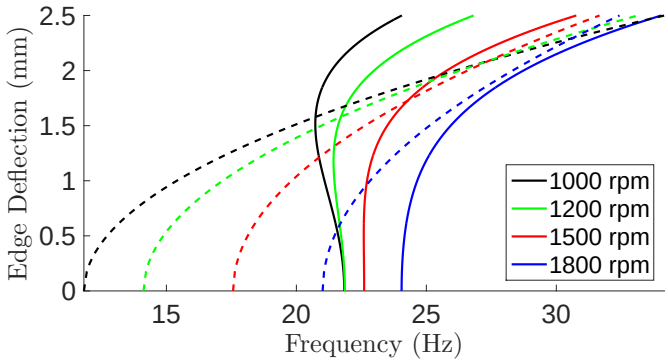

Figure 3.5: Backbone curves at "low angular velocities" (dashed line=without gravity, solid line=with gravity)

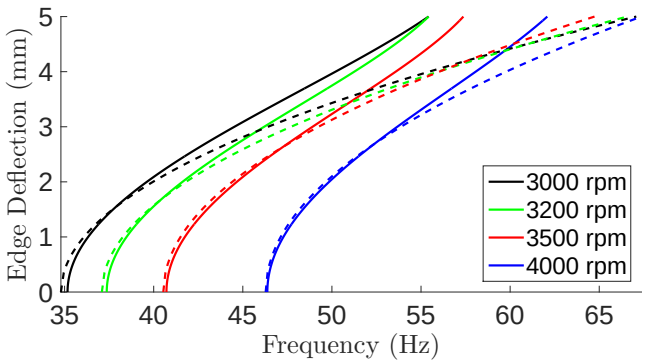

Figure 3.6: Backbone curves at "high angular velocities" (dashed line=without gravity, solid line=with gravity)

3.2.2.2 Forced Vibration

Similarly, Benedettini and Rega (1987) evaluated the steady-state solutions to forced excitations and derived the frequency-response relation:

$$\Lambda = 1 - c_4 a^2 \mp \frac{1}{2}\left(1 + c_4 a^2\right)\sqrt{\frac{F^2}{a^2} - 4c^2} - c_7 a^4 - \frac{c^2}{2} - \frac{F^2}{8a^2} \pm \sqrt{\frac{c^2 F^2}{4a^2} + \frac{c_2^4 F^2 a^2}{81} - 4c_6 c^2 a^4} \tag{3.35}$$

where $F = \phi p_0$ is the amplitude of excitation from Equation 3.22 and with c_6 defined as:

$$c_6 = \frac{19}{72}c_2^2 - \frac{3}{16}c_3 \tag{3.36}$$

We now focus on a spinning membrane with dimensions shown in Table 3.1 at various angular velocities. Figure 3.7 shows the frequency-response curves for increasing angular velocities. We notice a transition between softening behavior at 1000 rpm and hardening behavior at 1650 rpm. We also notice that, for a given frequency of excitation, several amplitudes of vibration can exist. The stability of each branch is also represented (unstable branches are dashed). Figure 3.8 shows more details of the frequency-response curves at 1000 rpm, 1300 rpm and 1650 rpm. At 1000 rpm there are up to three steady state solutions with different amplitudes of oscillation, two are stable (solid lines) and one is unstable (dashed line). In addition during forward frequency sweeps (green arrows), the amplitude of oscillation is characterized by a jump at about 21.6 Hz and a sudden increase of amplitude of vibration. During backward sweeps (red arrows) the jump occurs at about 20.7 Hz. The vibration is thus path dependent and will depend on the initial conditions for a given frequency of excitation. At 1650 rpm the opposite happens and the membrane presents an hardening behavior. At 1300 rpm and for a frequency of excitation of about 21.8 Hz, we notice five steady state solutions, three stable and two unstable. Overall the solutions will depend on the initial conditions.

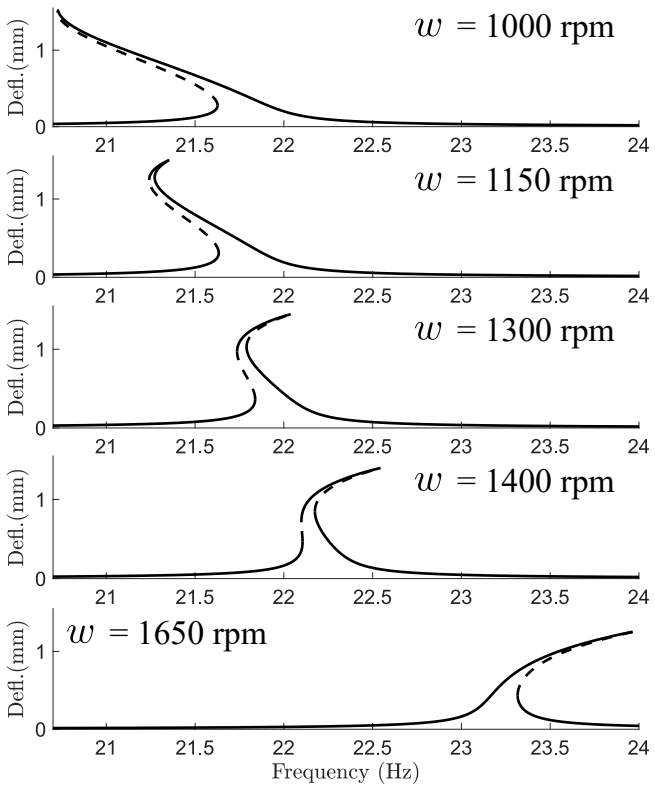

Figure 3.7: Frequency-response curves for increasing angular velocities for an amplitude of excitation A=50 mm.s^{-2} and a damping ratio of 0.12%.

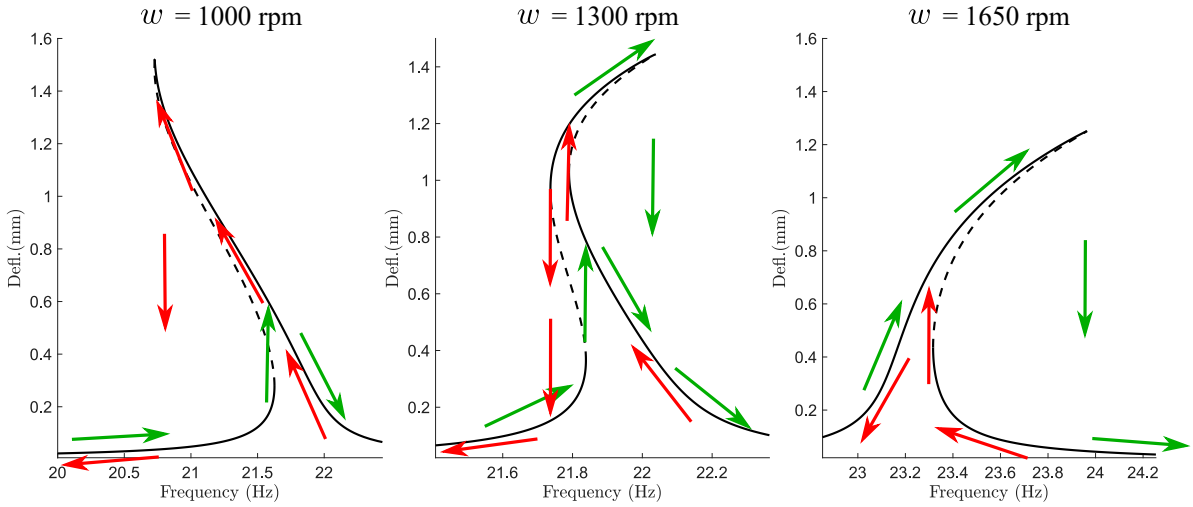

Figure 3.8: Jump phenomena for an amplitude of excitation A=50 mm.s^{-2} and a damping ratio of 0.12%

Finally, the influence of damping and amplitude of excitation at two different angular velocities, 1000 rpm and 5000 rpm, are presented. In Figure 3.9*a* the damping ratio is fixed at 0.3% and the transverse

acceleration amplitude increases from 5 mm.s^{-2} to 150 mm.s^{-2}. In Figure 3.9*b*, the transverse acceleration amplitude is fixed at 150 $mm.s^{-2}$ and the damping ratio increases from 0% to 1%.

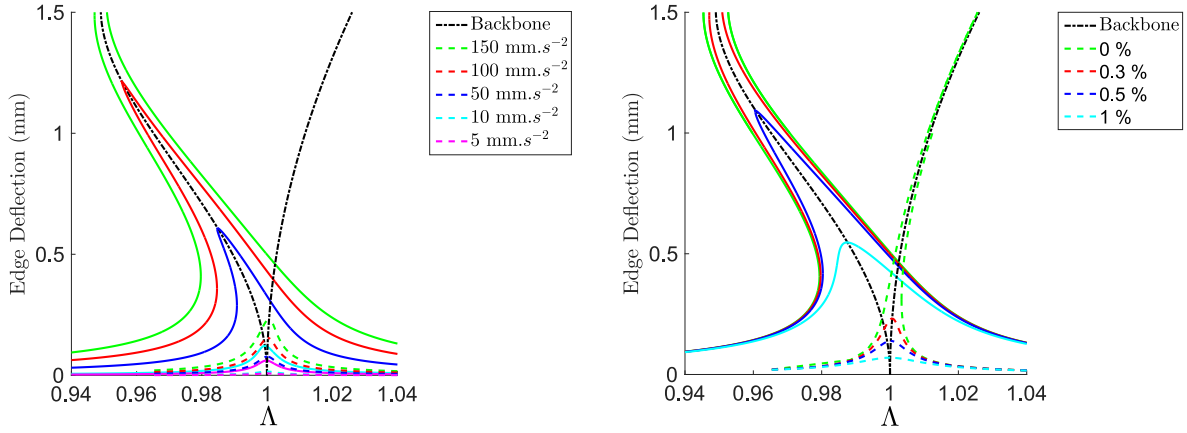

(a) Frequency-response curves (0.3 % damping) at different acceleration amplitudes (solid=1000 rpm, dashed=5000 rpm).

(b) Frequency-response curves (150 mm.s^{-2} acceleration amplitude) at different damping ratios (solid=1000 rpm, dashed=5000 rpm).

Figure 3.9: Frequency-response curves for increasing damping and amplitude of excitation.

We notice that the higher the damping the lower the response and that for high enough damping, the jump phenomenon and hysteresis disappear. In both cases we notice that the amplitude of the response for a given hub acceleration level decreases with the angular velocity and thus the amount of stretching in the structure.

3.3 Nonlinear Dynamic Simulation using Finite Element Method

We compare the analytical backbone curves with results from finite element simulations using Abaqus to estimate the validity of the reduced order model. There are several techniques to simulate the geometrically nonlinear vibrations of spinning membranes and estimate their characteristic parameters. One can run a dynamic simulation with a forcing term that sweeps in increasing and decreasing frequencies that would estimate all the coefficients that describe the nonlinear behavior: w_0, c_2, c_3, and ϕ. However, as we are only interested in the nonlinear coefficients c_2 and c_3, we can estimate these directly from the backbone curves that are independent of amplitude of excitation and damping.

3.3.1 Implementation in Abaqus/Standard

We use Abaqus/Standard to simulate the backbone curves of the oscillator. The simulations are performed in the rotating frame of reference such that the hub is fixed. As this frame rotates at constant angular velocity,

the centrifugal force and the Coriolis force are added to the simulations. First, we find the equilibrium of a spinning membrane deflected by gravity is calculated. Then, the membrane is deformed according to the first axisymmetric mode of vibration. Finally, a nonlinear dynamic simulation of the free vibration of the membrane with little stiffness proportional damping is performed. This is similar to the technique described by Soares and Gonçalves (2012).

We consider a linear elastic material. The membrane is modeled with S4R shell elements: 4-node doubly curved thin shell elements with reduced integration, hourglass control, finite membrane strains, and 5 thickness integration points elements. The mesh contains 2,151 nodes. We follow the steps summarized in Figure 3.10. We first apply a centrifugal and Coriolis loads (step 1) with angular velocity ω to stiffen the membrane. Then gravity g is added (step 2) to obtain the equilibrium deflected shape. For those two steps we use a linear "static" step (Newton's method). From this equilibrium we can evaluate the mode shapes and natural frequencies in a linear perturbation step (step 2') and introduce this as an initial perturbation in a "static" step (step 3). To introduce this initial perturbation we impose the appropriate displacement as boundary conditions to each node of the membrane using a Python script. As Abaqus imposes boundary conditions relative to the initial shape (flat and unstressed) the imposed displacements are the equilibrium plus a chosen amplitude A multiplied by the mode shape. Finally we run a nonlinear dynamic implicit simulation (step 4) with small stiffness proportional damping. This damping is necessary to decrease the amplitude of oscillation and to be able to monitor the associated change in frequency. Too high damping damps the oscillations too fast to precisely estimate the backbone curve, whereas too little damping unnecessarily increases the time of the simulation.

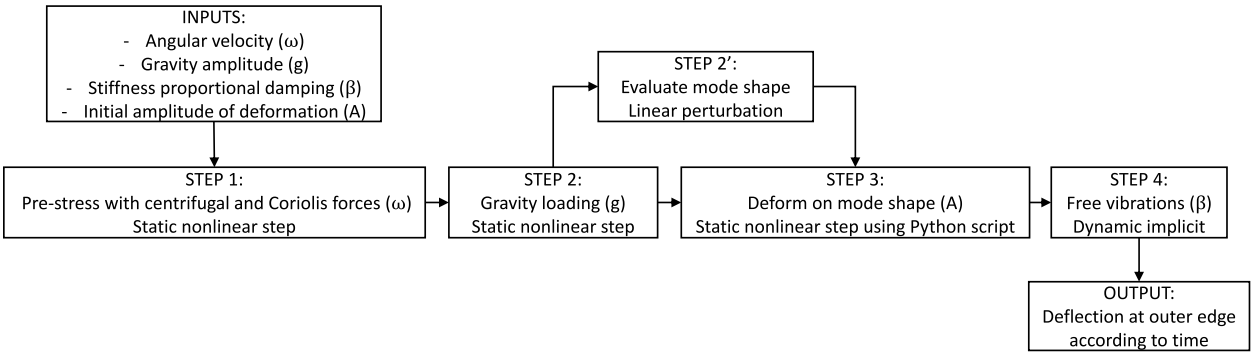

Figure 3.10: Steps of FEM simulation.

We ran simulations at two angular velocities: 1200 rpm and 4000 rpm. 1200 rpm is close to the buckling angular velocity and 4000 rpm to the maximum speed of the motor in the experimental setup detailed in part 3.4. In this step we use the Hilber-Hughes-Taylor integration scheme with no numerical damping (α=0) and small time step (half increment residual). A small time step is necessary to obtain accurate results. Large time steps would for example change the apparent resonant frequency of oscillation of the membrane. A

convergence analysis was carried out to estimate a proper time step and a maximum time step was imposed. The time step was tuned to obtain accurate natural frequency at low amplitude of oscillation (linear system). We found that the parameters shown in Table 3.2 give accurate results. Figures 3.11 and 3.11a show the time response at a point on the outer edge for the two simulations.

ω (rpm)	1200	4000
g (m.s^{-2})	9.81	9.81
β (s)	4 $\times 10^{-5}$	5 $\times 10^{-5}$
A (mm)	0.5	1
δt_{max} (s)	0.01	0.002
T (s)	22	35
Total CPU time (s)	4.3 $\times 10^{5}$	1.4 $\times 10^{6}$

Table 3.2: Dynamic simulations parameters.

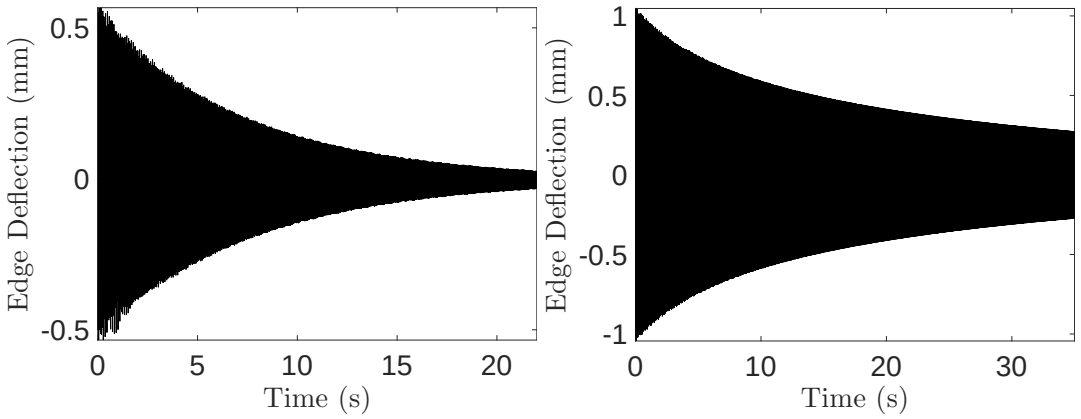

(a) Free vibration at 1200 rpm. (b) Free vibration at 4000 rpm.

Figure 3.11: FEM results.

3.3.2 Post Processing

We use a method similar to the one introduced by Londoño et al. (2015). It consists of estimating the instantaneous frequencies and envelope amplitudes based on the decaying response. First, the zeros of the response are found. In order to minimize noise, due to the imprecise estimation of the zeros for example, we don't estimate the frequency and amplitude between each of those zeros, but base on 10 periods. The instantaneous frequencies are defined as ten times the inverse of the time between 10 periods. As the damping ratio is very small in these decay curves, it doesn't affect the instantaneous frequency. The instantaneous amplitude is the maximum amplitude within each ten periods.

Figure 3.12a and 3.12b show the instantaneous frequency and amplitude, respectively, at 1200 rpm and 4000rpm. First, we notice that the data are more sparse at 1200 rpm than 400 rpm. Even if the signal

runs for the same amount of time, as the frequency is higher at 4000 rpm, we have more periods to process. One could run a longer simulation with less damping at 12000 rpm to obtain more results. We notice that the frequency increases with amplitude at 1200 rpm, characteristic of softening behavior. Conversely, the frequency decreases with amplitude at 4000 rpm, characteristic of hardening behavior.

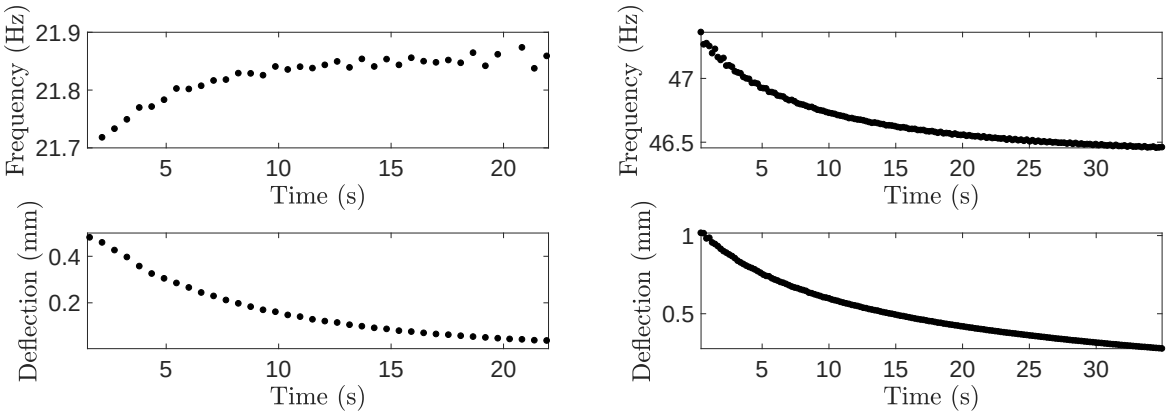

(a) 1200 rpm. (b) 4000 rpm.

Figure 3.12: Instantaneous frequencies and amplitudes.

3.3.3 Comparison Between Reduced Order Model and FEM Simulations

In Figures 3.13*a* and 3.13*b* we compare the reduced order model and FEM backbone curves at 1200 rpm and 4000 rpm, respectively. We notice an excellent agreement between the reduced order model and the nonlinear FEM simulations. This confirms the validity of the reduced order model.

3.4 Experiments

3.4.1 Experimental Setup

To characterize the dynamics of the membrane experimentally, the circular membrane is spun horizontally inside a vacuum chamber and is measured using two high speed DIC cameras as well as a laser vibrometer. This experimental setup is shown in Figures 3.14a and 3.14b. The Kapton membrane is clamped on a central hub, which is connected to a motor (brushless 5 Watt by Maxon Motor) through a shaft. The shaft is supported by two low friction sleeve bearings that allow for axial motions. The membrane and the entire system 'motor-shaft-hub' are excited vertically with an electromagnetic shaker (ET 132 Labworks Inc.) attached to the bottom of the motor. General experimental methods for modal analysis can be found in (Ewins, 2000). Since the membrane is excited symmetrically, this setup is restricted to the study of symmetric modes of the membrane. The motor has internal sensors that are used for closed loop control

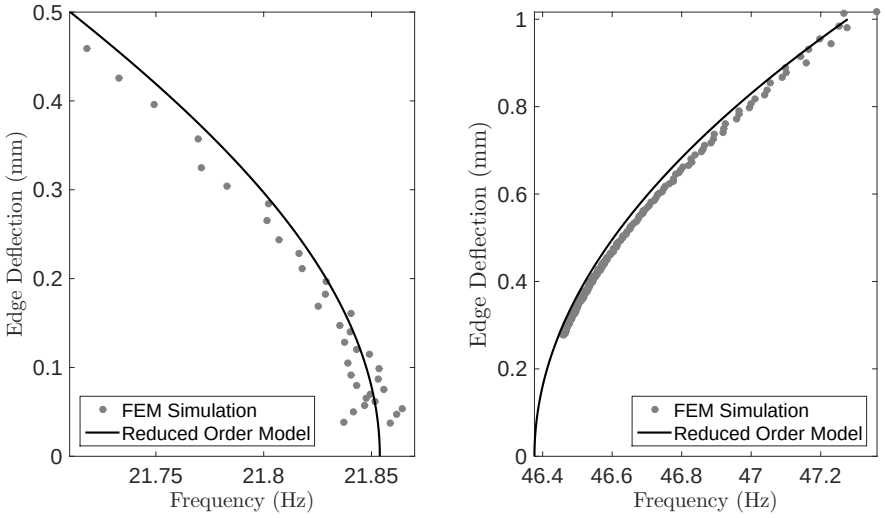

(a) 1200 rpm.

(b) 4000 rpm.

Figure 3.13: Backbone curves from simulations compared to theoretical ones.

of its angular velocity. To provide a stiffness to the system while allowing a vertical motion, a spring is attached between the motor and the fixed base. The oscillation of the hub does not correspond exactly to the excitation signal from the function generator, but rather there is a coupled motion of the membrane with the 'motor-shaft-hub system'. A study of this coupled motion was performed and the stiffness of the spring was chosen to minimize the coupling while maintaining high enough amplitudes of oscillation at the shaft, such that a constant amplitude sinusoidal sweep voltage profile input at the shakers leads to a constant amplitude sinusoidal sweep displacement at the hub. To further monitor the excitation, the oscillation of the hub is measured.

The achievable vacuum inside the chamber is 28.9 in Hg which corresponds to 96.6% of vacuum. The bearings allow minor lateral motion of the rotating shaft, which introduce undesired vibration in the membrane. To quantify the noise due to the bearings and to the remaining air inside the setup, the vibration of the edge of the membrane spinning at 1800 rpm was measured using the laser vibrometer (see 3.4.2.2). The displacements of the membrane edge and the corresponding Fourier transform are shown in figure 3.15. The amplitude of the noise is approximately 30 μm, which is smaller than the thickness of the membrane. Some narrow peaks highlighted by the orange dotted line can be observed in the Fourier transform of the measurement. The frequency of these peaks correspond to the frequency of the rotation (1800 rpm = 30 Hz) and its higher harmonics. Since the frequencies of these peaks are known, they do not introduce noise in the measurement as long as the frequency range of interest does not coincide with one of them.

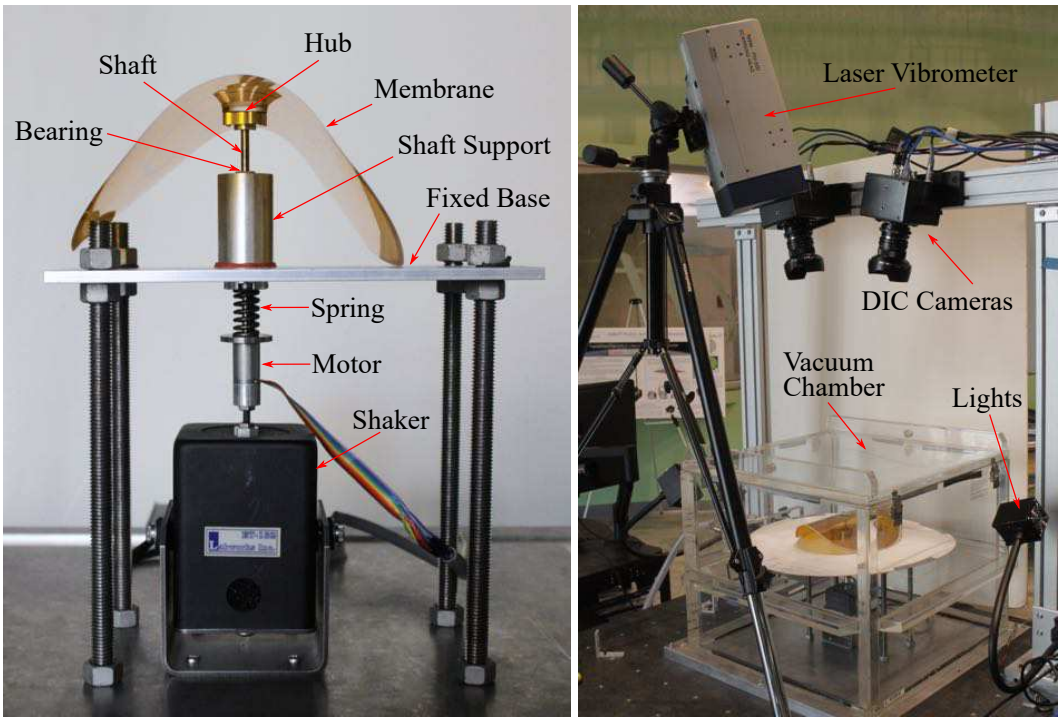

(a) Mechanical setup. (b) Full setup.

Figure 3.14: Experimental setup.

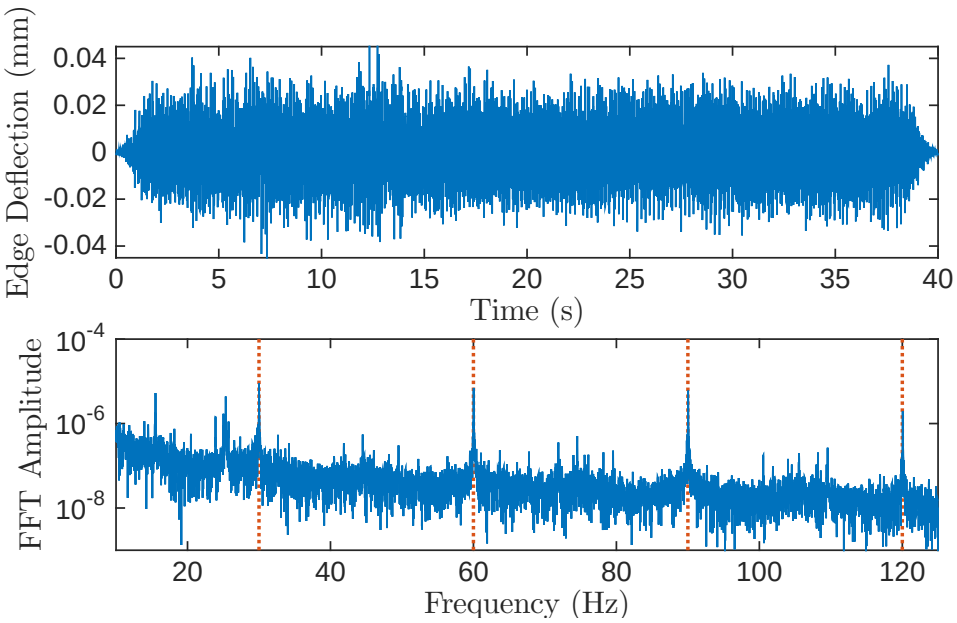

Figure 3.15: Noise in the setup: time measurement (top) and Fourier transform (bottom).

3.4.2 Measurement Techniques

Two different measuring methods were used to characterize the dynamic behavior of the membrane. The modal shapes are measured by a Digital Image Correlation system, while the transverse vibration is analyzed using a laser vibrometer.

3.4.2.1 Stereo DIC

Digital Image Correlation is an image based method that matches points of the measured sample in different images, and uses triangulation techniques to estimate 3D displacements. By defining a reference image, the displacement of the sample with respect to this reference image can be measured for each frame and the resulting deformations and strains can be calculated. The software applies an optimization algorithm to track speckles that are printed on the surface of the membrane and correlates the position of the speckles with their position on the reference image. The membrane with speckles is shown in Figure 3.16b.

By using two synchronized high speed cameras, the vertical motion of the membrane can be captured. Two Fastcam Mini UX100 high speed cameras from *Photron* with 18 mm f/3.5 Distagon T* lenses from *Zeiss* and a DIC software from *Correlated Solutions* are used in the experiments. The membrane is imaged 1250 times per second with an exposure time of 25 μs. The exposure time is limited by the illumination of the membrane, which is realized by four halogen lamps. Our samples are made of Kapton which is a transparent, reflective material. To avoid direct reflections into the camera and shadows, the membrane is lighted from below using a white reflective surface placed beneath the membrane. The experimental setup is schematically shown in Figure 3.16a.

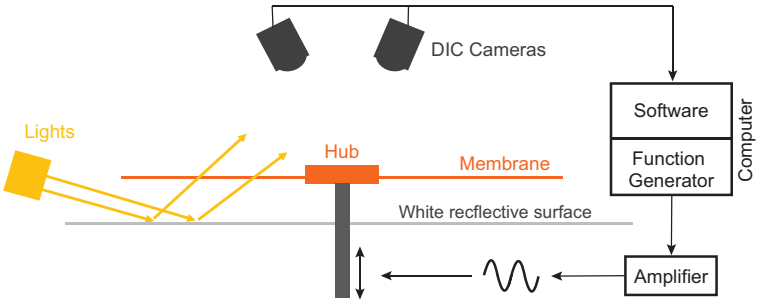

(a) Experimental scheme with the DIC cameras.

(b) Membrane used in DIC measurements.

Figure 3.16: Setup and membrane for DIC measurements.

The main advantage of the DIC system is that the membrane is analyzed in a local frame of reference since each image is correlated to the reference image. The images are stored first in the internal camer storage, which is limited and puts a constraint on the measurement length. The longest possible measurement with the resolution and frame rates chosen is approximately 15 seconds, which is not enough to characterize the

nonlinear behavior of the membrane. This technique was used to estimate the modes of vibration and the equilibrium shapes. The results will be presented in Sections 3.4.3.2 and 3.4.4.1.

3.4.2.2 Laser Vibrometer

A PSV-500 *Polytec* scanning laser vibrometer was used to measure the transverse vibration of the membrane (see Figure 3.17a). A single point on the membrane and a point at the hub are measured. Since the force is not directly measured, the acceleration measured at the hub is used instead as the input. The laser is stationary, so a ring on the rotating membrane rather than a single point is measured. This is adequate as we are interested in the symmetric modes. In order to get a good reflection of the laser beam, two rings were painted on the surface of the membrane (see figure 3.17b). In contrast to the DIC measurements, very long measurements are achievable with the laser. This was used to measure edge deflection during slow frequency sweeps.

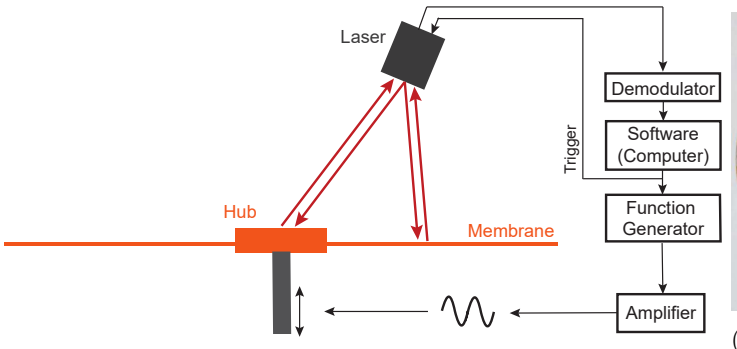

(a) Experimental scheme with laser vibrometer.

(b) Membrane used with laser vibrometer.

Figure 3.17: Setup and membrane for laser vibrometer measurements.

Signal Processing: Instead of performing a spectral analysis using a Fourier transform, the amplitude of the response is plotted against the corresponding excitation frequency. The envelope amplitude is calculated by computing the RMS value for subsequent intervals of the response ($RMS(x) = A/\sqrt{2}$). This method achieves better results than a Fourier transform. We are looking to compare the displacement amplitude of the response, whereas the laser measures the velocities. To overcome this, the Fourier transform of the velocity signal is calculated, the displacements (and accelerations) are easily computed in the Fourier domain, and finally the inverse transform is carried out. The Fourier domain is also well suited to filter the noise from the signal. This entire process is illustrated in Figure 3.18.

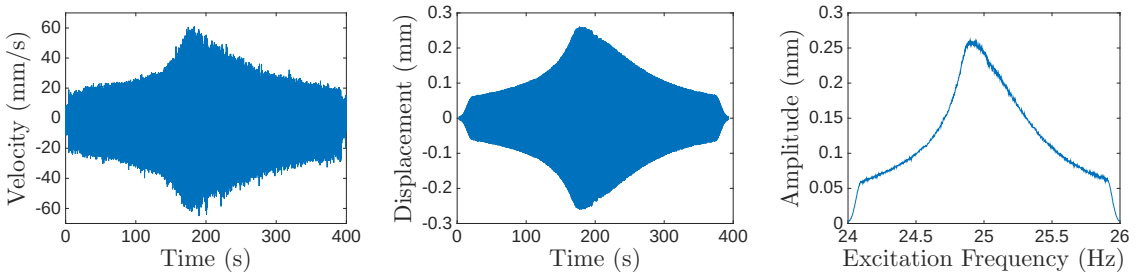

(a) Velocity signal. (b) Filtered displacement signal. (c) Displacement signal - RMS.

Figure 3.18: Laser data processing.

3.4.3 Experimental Results

We experimentally measured equilibrium shapes, mode shapes, and nonlinear vibration of the spinning membrane under gravity. To observe the nonlinear effects of the membrane, the system is excited with a slow frequency sweep with a typical bandwidth of 2Hz around the resonance, over 400 seconds. The response is then measured at the half radius of the membrane with the laser vibrometer. Once the resonance frequency is known, the membrane is excited with a constant frequency at its resonance and the DIC cameras are used to measure the modal shapes to assess the validity of ansatz 3.23 (i.e., the mode shape remains constant even at high amplitude of excitation).

3.4.3.1 Equilibrium

The equilibrium shapes of the membrane for three different angular velocities are first measured using DIC. Figure 3.19 shows the average axisymmetric deflections for three angular velocities: 2200 rpm, 2700 rpm, and 3500 rpm. As expected, as the angular velocity increases, the overall deflection decreases. Figure 3.20 shows the 2D equilibrium shapes. We notice that the equilibrium shapes are not perfectly symmetric; the edges of two opposite sides are deflected in all shapes shown. This can be explained by the prestress in the membrane, which becomes significant especially at the edges, since the in-plane stresses due to the centrifugal load become smaller at the edges.

3.4.3.2 Mode Shapes

The first and second symmetric mode shapes were measured for several different excitation amplitudes at the resonances using the DIC cameras. The full 2D mode shapes at the maximum deflection are shown in Figure 3.21.

To compare the modal shapes at different amplitudes, the deflections along eight radial slices around the membrane are averaged. The resulting radial shapes of both modes are presented in Figures 3.22a and 3.22b. In both cases, the modal shapes at the three lower amplitudes are close to proportional. This indicates a

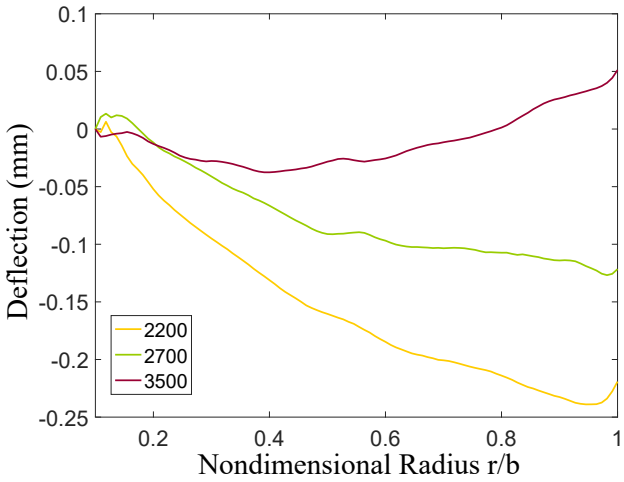

Figure 3.19: Equilibrium shapes at increasing angular velocities.

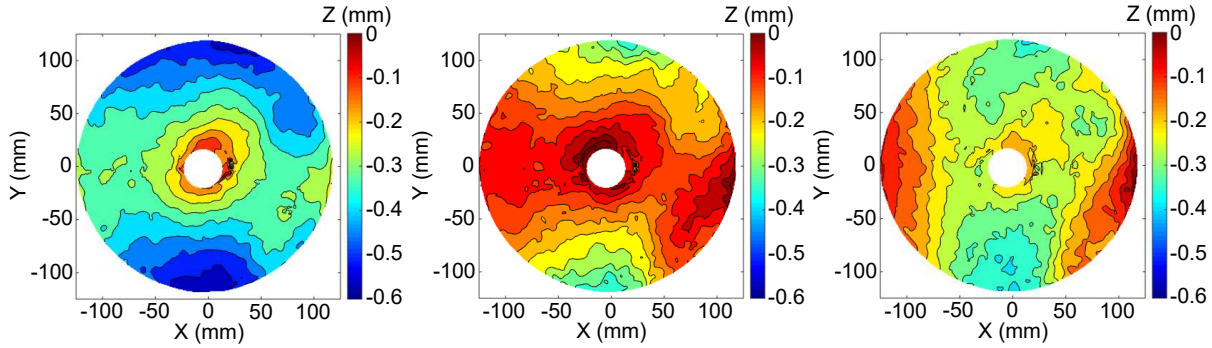

(a) Equilibrium at 2200 rpm. (b) Equilibrium at 2700 rpm. (c) Equilibrium at 3500 rpm.

Figure 3.20: Equilibrium at increasing angular velocities.

linear behavior of the modal shapes at these amplitudes. At the largest excitation the membrane starts to wrinkle and the shapes differ from the linear case. The modal shape of the membrane can therefore be considered linear for small enough amplitudes, which correspond to the assumption of ansatz 3.23.

3.4.3.3 Nonlinear Vibration

The vibration at the half radius of the membrane were measured with the laser vibrometer. The first mode of the membrane was excited with forward and backward frequency sweeps (400 s duration) at different amplitudes. The filtered time response are presented in Figure 3.23 for the membrane spinning at 3500 rpm and increasing hub acceleration from 45 mm.s^{-2} to 170 mm.s^{-2}. The filtering technique consisted in removing all the components of frequencies outside the range of the sweep. The membrane exhibits different nonlinear behavior for different rotational speeds. The response at 3500 rpm and 1800 rpm are presented in Figures 3.24b and 3.24a. The forward and backward frequency-response curves should match away from

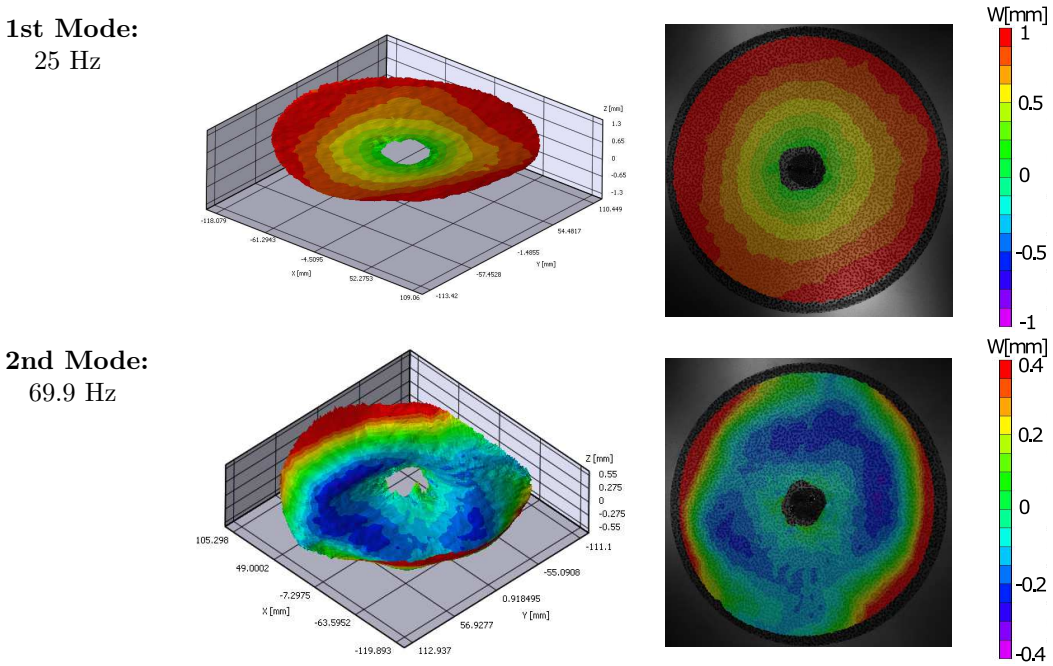

Figure 3.21: Modal shapes of first and second symmetric modes at 1800 rpm.

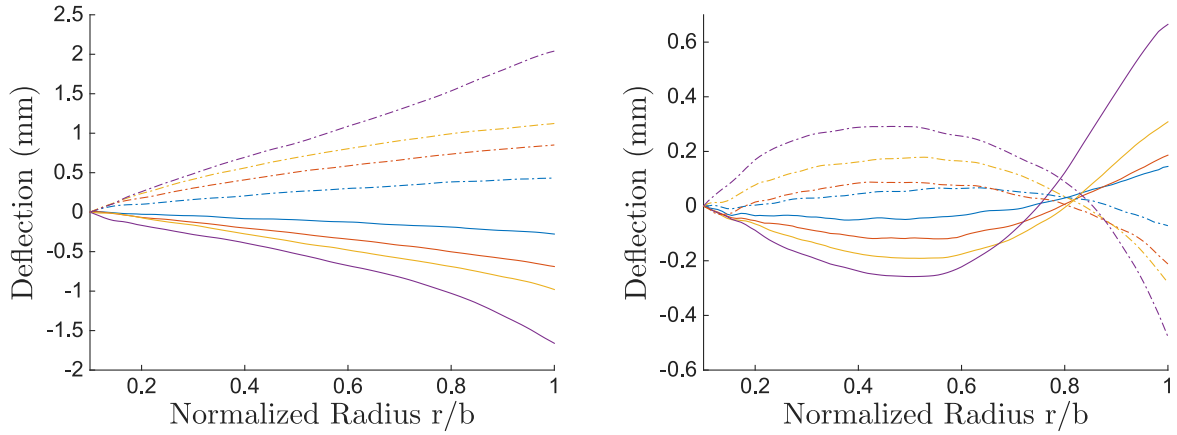

(a) Radial modal shape of the first symmetric mode (lower (solid line) and bigger (dotted lines) amplitudes).

(b) Radial modal shape of the second symmetric mode (lower (solid line) and bigger (dotted lines) amplitudes).

Figure 3.22: Measurements of first two axisymmetric mode shapes at 1800 rpm and increasing amplitude of deflections.

the jump. We notice on those plots that it is not exactly the case. This is because for a given input voltage to the shaker the amplitude of excitation at the hub is slightly different from one sweep to another. The membrane exhibits a hardening behavior at 3500 rpm, whereas softening is observed at 1800 rpm. We notice in the case of 3500 rpm that the membrane behaves linearly at the lowest amplitudes of excitation; the resonance peaks are symmetric and the response is the same for forward and backward excitations. At larger

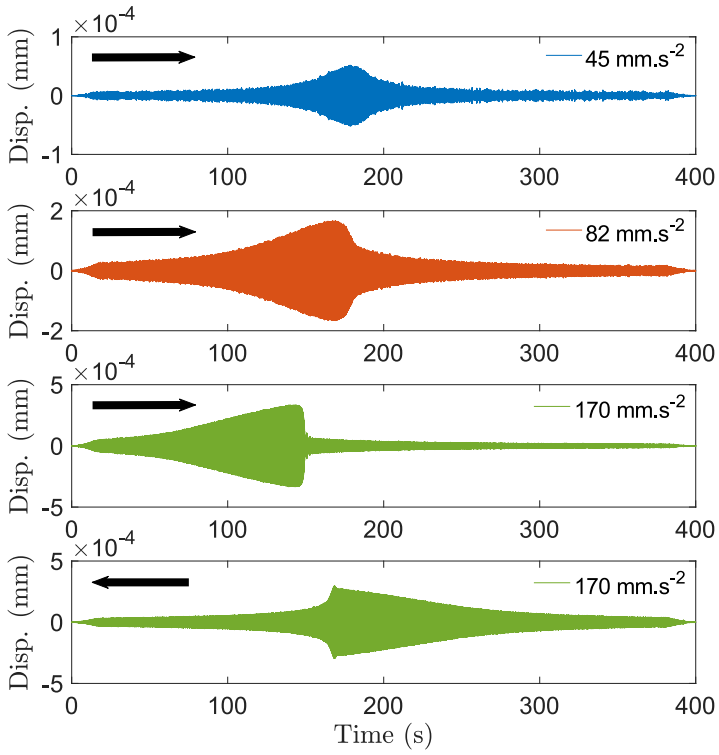

Figure 3.23: Filtered time response at 3500 rpm and increasing hub accelerations.

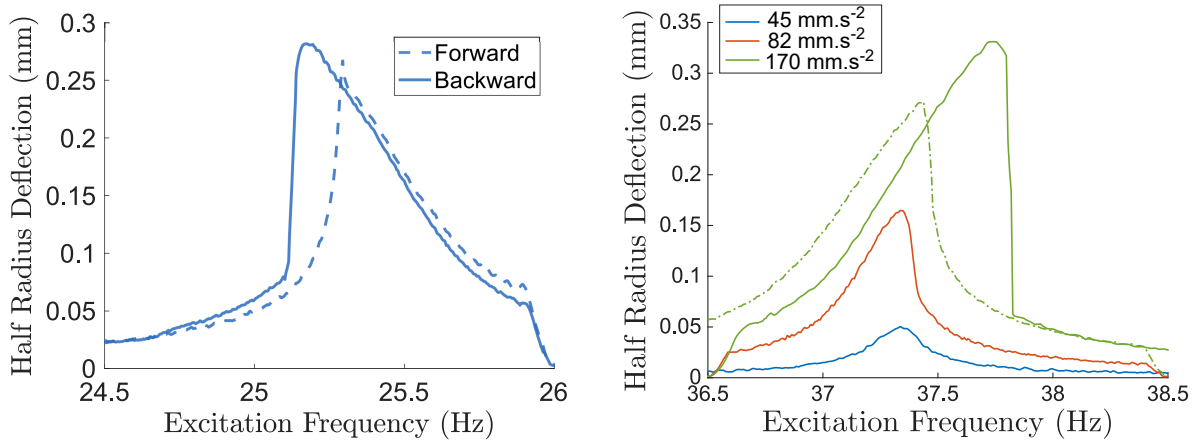

(a) Frequency-response curves at 1800 rpm (solid lines=Backward, dashed lines=Forward) and hub acceleration of 71 mm.s^{-2}.

(b) Frequency-response curves at 3500 rpm and increasing hub accelerations (solid lines=Forward, dashed lines=Backward).

Figure 3.24: Experimental frequency-response curves at low (1800 rpm) and high (3500 rpm) angular velocities.

amplitudes, nonlinear effects such as softening/hardening, bifurcations, and jumps in the amplitude of the response are observed.

The transition between softening and hardening regimes at increasing angular velocities is predicted by the mathematical model presented previously. The importance of gravity decreases for increasing speeds of rotation, as shown in Section 3.4.3.1.

3.4.4 Comparison Between Reduced Order Model and Experiments

3.4.4.1 Mode Shapes

The measured modal shapes are in good agreement with the finite element simulations and with theory. The normalized modal shapes of the first and second symmetric modes were determined by the theoretical model with and without gravity, by the finite element simulations, and were experimentally observed. The resulting modal shapes at 1800 rpm can be compared in Figure 3.25.

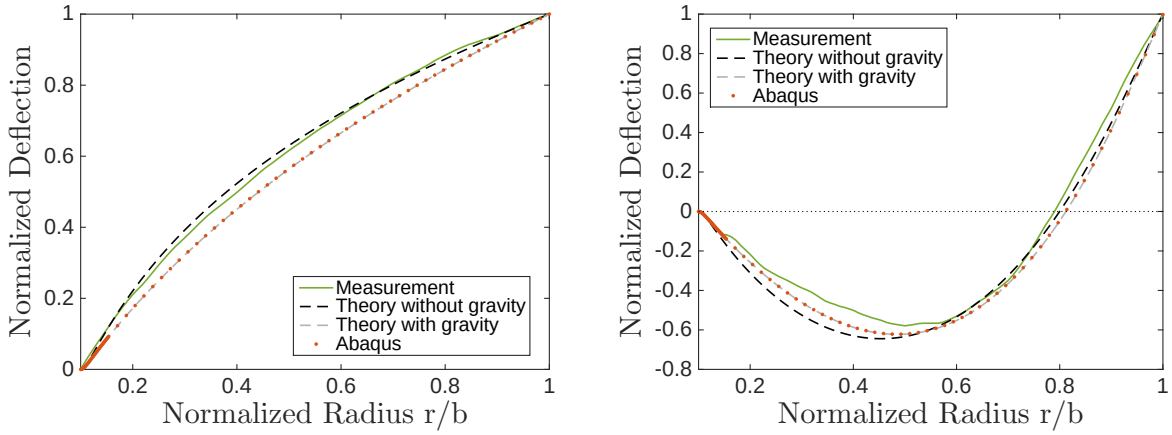

(a) Shape of first symmetric mode.

(b) Shape of second symmetric mode.

Figure 3.25: Comparison of the experimental and theoretical radial mode shapes

3.4.4.2 Nonlinear Behavior

The reduced order model developed to describe the transverse vibration of the membrane is compared here with the experimental measures. First we estimate the experimental dimensionless quantities w, p and c in order to justify our scaling analysis (Section 3.2.1). In particular those quantities were assumed to be $\mathcal{O}(1)$ as $\frac{h}{b}$ tends to zero. Table 3.3 shows the estimated dimensional quantities and their associated dimensionless values for ω=3500 rpm. We can see that w and p are indeed $\mathcal{O}(1)$. The damping coefficient in the experiments is higher but overall, the dimensionless terms are in agreement with the scaling analysis.

Let us now compare the response of the oscillator. The hardening behavior at 3500 rpm is well described by the model, but the resonance frequency predicted with the model is 40.7 Hz, whereas the experiments

	Estimated dimensional values	Dimensionless values
Deflection	$\bar{w} \leq 0.35$ mm	$w \leq 1$
Pressure	$\bar{p} \leq 0.0121$ Pa	$p \leq 6$
Damping coefficient	$\bar{c} \approx 0.007$	$c \leq 106$

Table 3.3: Scaling parameters at 3500 rpm.

observe the resonance at 37.3 Hz. To make the comparison of these responses easier, the frequency of excitation is normalized here by the corresponding resonance frequency. The damping used in the models was extracted from the width of the experimentally measured resonance peaks and are reported in Table 3.4. The average amplitude of the acceleration measured at the hub ($\ddot{d}_h$) is used as the excitation in the model ($p_0 = \rho \ddot{d}_h h$ from Equation 3.22). The model is compared to the measurements for three different amplitudes at 3500 rpm in Figure 3.26b. The amplitudes and the corresponding acceleration values are shown in Table 3.4. It can be observed that the reduced order model captures the nonlinear hardening behavior as well as the vibration amplitudes, with exception of the lowest amplitude, which could be explained by experimental uncertainties at these low amplitudes.

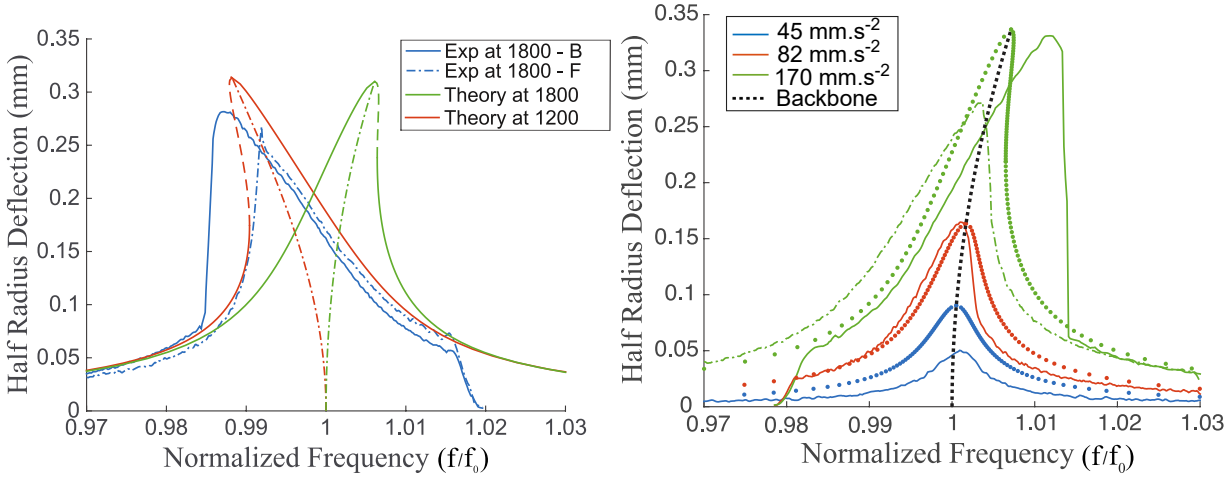

(a) Experiments and theoretical model at lower speeds (1800 rpm & 1200 rpm) for 71 mm.s^{-2} acceleration at the hub.

(b) Experiments and theoretical model at 3500 rpm (solid lines=experiment forward, dashed lines=experiments backward, dotted lines=theory).

Figure 3.26: Comparison of experimental and theoretical frequency-response curves at 1800 rpm and 3500 rpm.

The experiments measure softening at 1800 rpm, but the model predicts softening only at lower speeds of rotation. This can be explained by the initial curvature of the sample. In fact, the overall deflection under gravity is higher because of this initial downward curvature. This is similar to a membrane sagging under a higher gravity load, or a lower angular velocity, and thus is more likely to present an softening behavior. The measurement at 1800 rpm is compared in Figure 3.26a with the results of the model at 1800

	Amplitude	Hub Acceleration (mm/s^2)	Exp. Damping Ratio (%)
3500 rpm:	1	45.5	0.3
(figure 3.26b)	2	82.4	0.3
	3	169.6	0.3
1800 rpm:	1	71.0	0.27
(figure 3.26a)			

Table 3.4: Acceleration measured at the hub and estimated damping in the experiments.

rpm and 1200 rpm for a single amplitude of excitation. It can be concluded that the nonlinear behavior of the membrane measured in the experiments matches the predictions from the mathematical model developed in this chapter.

3.5 Conclusion

We have studied the axysymmetric nonlinear vibration of an axisymmetrically deflected spinning membrane. A reduced order model using von Kármán plate equations has been derived. The nonlinear coefficients of the equivalent oscillator have been explicitly formulated. It is shown that these coefficients depend on four dimensionless parameters: the dimensionless angular velocity Ω, dimensionless gravity load G, the Poisson's ratio ν, and the inner to outer radius ratio α. We find that the oscillator is a single well Helmholtz-Duffing oscillator, while results from the literature on axisymmetric nonlinear vibration of flat spinning annulus predict a Duffing oscillator. Thus the deflection of the membrane fundamentally alters its nonlinear behavior and introduces a quadratic term in the restoring force. The general steady-state solutions of such oscillators have been reported. It is shown that at high angular velocities and for small amplitudes of excitation the membrane exhibits a hardening behavior while a softening behavior characterizes the oscillations at high angular velocities. A threshold between hardening and softening at low amplitudes of excitations was numerically computed for a wide range of dimensionless parameters.

A finite element simulation in Abaqus/Standard that simulates the nonlinear oscillations of deflected spinning membranes is presented. We find that such simulations require a fine time step and appropriate damping coefficients to obtain accurate results while decreasing the simulation time. The tuned values corresponding to the experimental sample are reported. A post-processing technique on the decay response of the oscillator is used to estimate the backbone curve from the simulations. An excellent agreement between simulations and analytical results is found.

Finally, an experimental setup that decouples translational and rotational motions has been presented and laser vibrometry was used the measure the deflection of the membrane during slow frequency sweeps. The experiments show a very good agreement with the theory and the discrepancies have been attributed to the initial curvature of the sample.

We have presented a general formulation including the bending stiffness of the thin plate. A formulation neglecting the bending stiffness could also be derived. The general method would be the same, but singular second order boundary value problems are expected to be found instead of the fourth order equations.

The results from this chapter can be used to design experimental setups to limit the influence of gravity on the nonlinear behavior of spinning disks. They can also be used to estimate the influence of a perturbation at the hub of a spacecraft (reaction wheels for example) that occurs at an axisymmetric resonance (first resonance of spinning thin disks). As an extension to this work, one could study the dynamic response of a spinning membrane at an angle relative to gravity. In that case the membrane would be dynamically excited by the stationary gravity load. Some critical angular velocities can occur. The nonlinear vibration at those angular velocities could be studied.

Chapter 4

Parametric Analysis of Spinning Origami Packageable Structures

4.1 Introduction

In this chapter we study more realistic structures made of hinged panels following an origami pattern that enables packaging. The aim of this chapter is to estimate the influence of those hinges on the behavior of the spacecraft and, in particular, to estimate the speed at which those hinges do not influence the behavior of the spacecraft. We focused on the origami pattern presented in Figure 4.1 (Arya, 2016). This pattern is

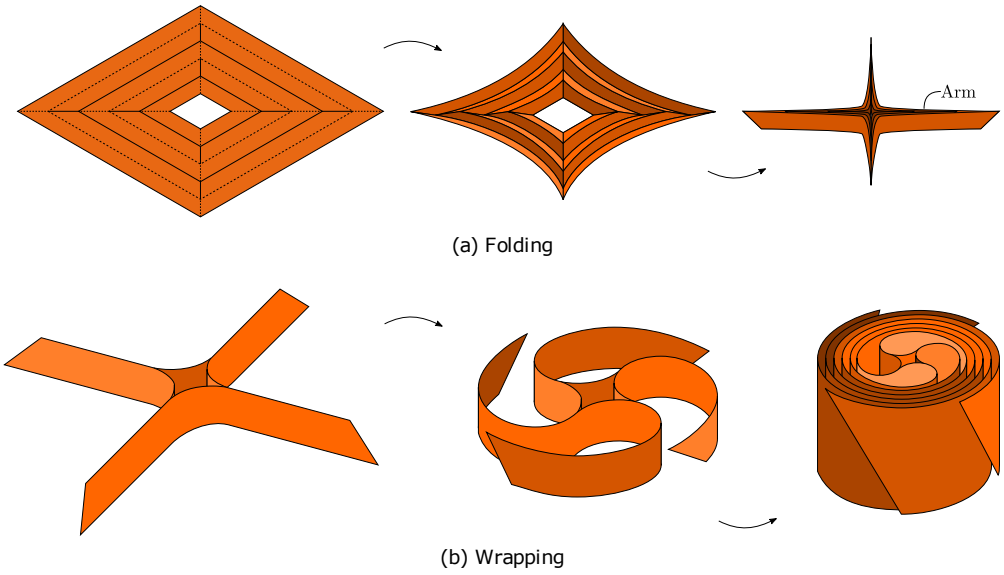

Figure 4.1: Folding concept (Arya, 2016)

a common choice for solar sailing missions (IKAROS, Sunjammer, ATK) or the space solar power satellite mission (Caltech SSPI). The associated packaging concept is also represented in Figure 4.1 and consists of

two main steps: folding and wrapping. Traditionally, the connections between panels are hinges with one degree of freedom: the rotation along the hinge line. As the structure gets bigger and the panel thicker, some shear would develop at the fold lines, which is incompatible with those hinges. Instead sliding hinges were introduced by Arya et al. (2017), and Arya et al. (2015). Those hinges have two degrees of freedom, rotation and translation along to the direction of the edge, and accommodate sliding of the panels. Some analysis of the behavior of such structures, prestressed using booms have been performed (Arya et al., 2016). Here we focus on spinning origami packageable structures and prestressing using centrifugal force.

Those origami packageable structures are characterized by discrete changes in bending stiffness at the fold lines. Such hinges are difficult to reproduce at small scales for lab experiments and they complicate the analytical formulation of the problem. We thus implemented this model in FEM using Abaqus/Standard. An Abaqus model of "flexible hinges" has been developed using Abaqus connector elements. Two kinds of connector were considered: revolute joints and cylindrical joints. The degrees of freedom of each of those joints are shown Figures 4.2a and 4.2b. They respectively model fixed hinges with one d.o.f. and sliding hinges with two d.o.f. We are interested in the influence of those hinges on in-plane stress distribution and frequencies since those quantities characterize the linear behavior of the structure. The geometry and dimensions of the considered structure are shown in Figure 4.3. In this model the plate is isotropic with constant thickness and the inner edge of the structure is clamped.

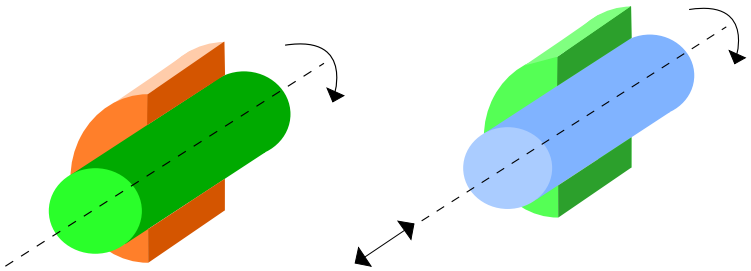

(a) Revolute joints kinematics. (b) Cylindrical joints kinematics.

Figure 4.2: Joints degrees of freedom.

The next section describes the Abaqus/Standard FEM model. The following section presents results in terms of in-plane stress fields. Then the natural frequencies are compared to isotropic structures. Finally some examples are presented.

4.2 Abaqus Model

These origami structures are approximated by connected isotropic, homogeneous plates. When the structure is wrapped, shear mainly focuses on the horizontal and vertical edges (Arya, 2016). Figure 4.4 shows the different hinge locations based on this observation.

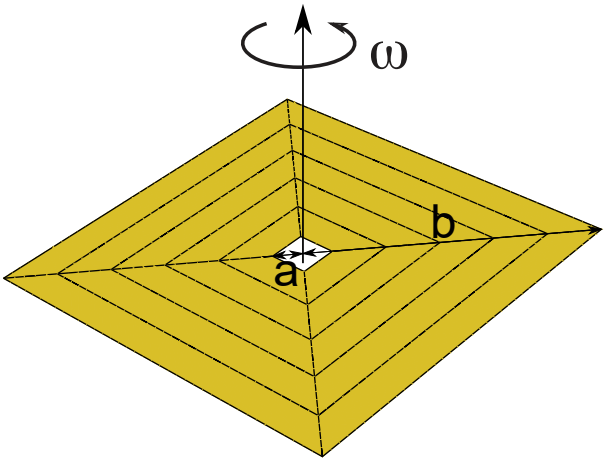

Figure 4.3: Schematic and notation of spinning origami packageable structure for 5 panels per quadrant (n=5).

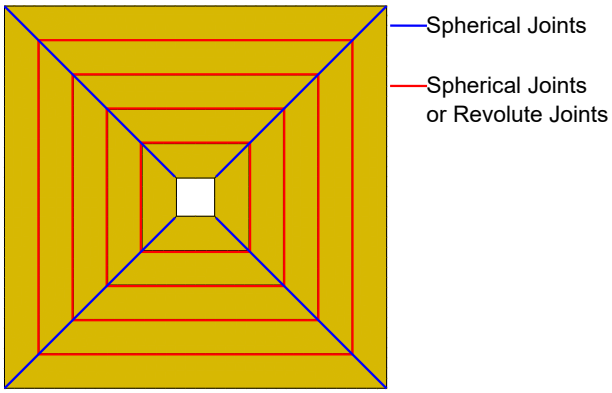

Figure 4.4: Schematic of the structure's hinges definitions. The sliding directions of the revolute joints are parallel to the edges.

By analogy with isotropic plates, for a given $\alpha = \frac{a}{b}$ (hub to membrane ratio), ν (Poisson's ratio), and n (number of panel per quadrant) the stress field is proportional to $\rho b^2 \omega^2$ and the dimensionless frequencies $\frac{2\pi f}{\omega}$ only depend on one parameter Ω (Equation 4.1). We are interested by the influence of the angular velocity (effectively Ω) and the topology of the structure (n) on its stress field and frequencies. Through this study we only consider α=0.1 and ν=0.34. In the Abaqus simulation we implemented a modular structure with the properties and dimensions shown in Table 4.1. A wide range of Ω was considered by changing ω.

$$\Omega = \sqrt{\frac{\rho h}{D}} b^2 \omega \tag{4.1}$$

We considered a linear elastic material with the properties of Kapton. The plates are modeled with S4R shell elements. The structure is clamped along the inner edge. The simulations were run in two steps.

Young's modulus E	2.5 GPa
Poisson's ratio ν	0.34
Density ρ	1420 kg m^{-3}
Thickness h	100 μm
Outer radius b	1 m
Inner radius a	10 cm

Table 4.1: Panel properties and structure dimensions.

First, a nonlinear static simulation prescribed the state of prestress due to centrifugal force. Then, a linear perturbation and frequency extraction was performed. The main novelty of this model is the implementation of the "flexible hinges". We detail this model in the next section.

4.2.1 Hinge Model

A particularity of these types of structure are the distributed hinges between the panels. Physically, this corresponds to many small ligaments on the edges of the panels or a thin "tape", weak in bending. We implemented a connector element between each opposite nodes on adjacent panels. In Abaqus, connector elements provide a versatile way to model physical mechanisms whose geometry is discrete (i.e., node-to-node) but with complex connections. Classically such elements are used in Abaqus to model physical hinges in a discrete way. We use those in a distributed manner. To do so we mesh each panel such that the nodes on two adjacent edges are collocated (see Figure 4.5a). We then add a "wire" with zero length between each of those collocated nodes. This process was automated with a script such that any number of panel n with any dimension b, geometry α, properties or mesh density can be quickly implemented. To avoid over-constraining the four nodes that meet at the corners we only implement three connectors, as shown in Figure 4.5b.

We have considered two kinds of connector element: spherical joints to model the fixed hinges between panels and cylindrical joints to model the sliding hinges. The first connector only constrains the translation degrees of freedom whereas the second one has two degrees of freedom: a rotation and a translation along to a defined axis. We focus here on zero stiffness hinges, but properties such as stiffness or damping can be easily added with this setup.

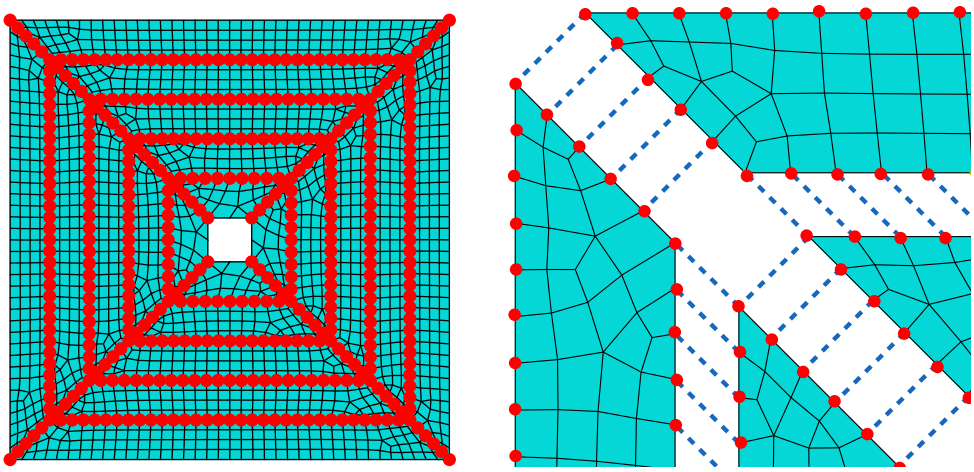

(a) Schematic of the hinge implementation. Each red dot corresponds to two nodes linked by a connector element.

(b) Exploded view of corner connector elements convention. Only three connections between the four nodes. Each dotted line is a connector.

Figure 4.5: Example hinged model in Abaqus/Standard (coarse mesh for illustration purposes).

4.3 Stress Distribution

The stress in such structures is proportional to $\rho b^2\omega^2$. Figures 4.6 and 4.7 show the components $\frac{\sigma_{11}}{\rho b^2\omega^2}$, $\frac{\sigma_{12}}{\rho b^2\omega^2}$ of the in-plane stress for spherical and cylindrical joints, respectively, for n=5 and n=10. As the structure is symmetric, the component σ_{22} is the same as σ_{11} but rotated 90°.

With spherical joints the stress distribution is the same as homogeneous membranes as all the in-plane degrees of freedom except normal rotation are constrained. The case of sliding hinges is more interesting. The panels slide relative to each other when centrifugal force is applied and the stress field is discontinuous around the hinges. The black and gray colors in Figure 4.6 and Figure 4.7 are, respectively, values higher and below the range that is shown and are points of stress concentration. Overall the minimum in-plane principal stress component is positive everywhere (zero at the free edge) so no buckling due to centrifugal load is expected.

4.4 Frequencies

In this part we focus on the frequencies of spinning spacecraft with increasing angular velocities. We studied each hinge type separately and in each case we compared the results to the isotropic (hinge-less) case.

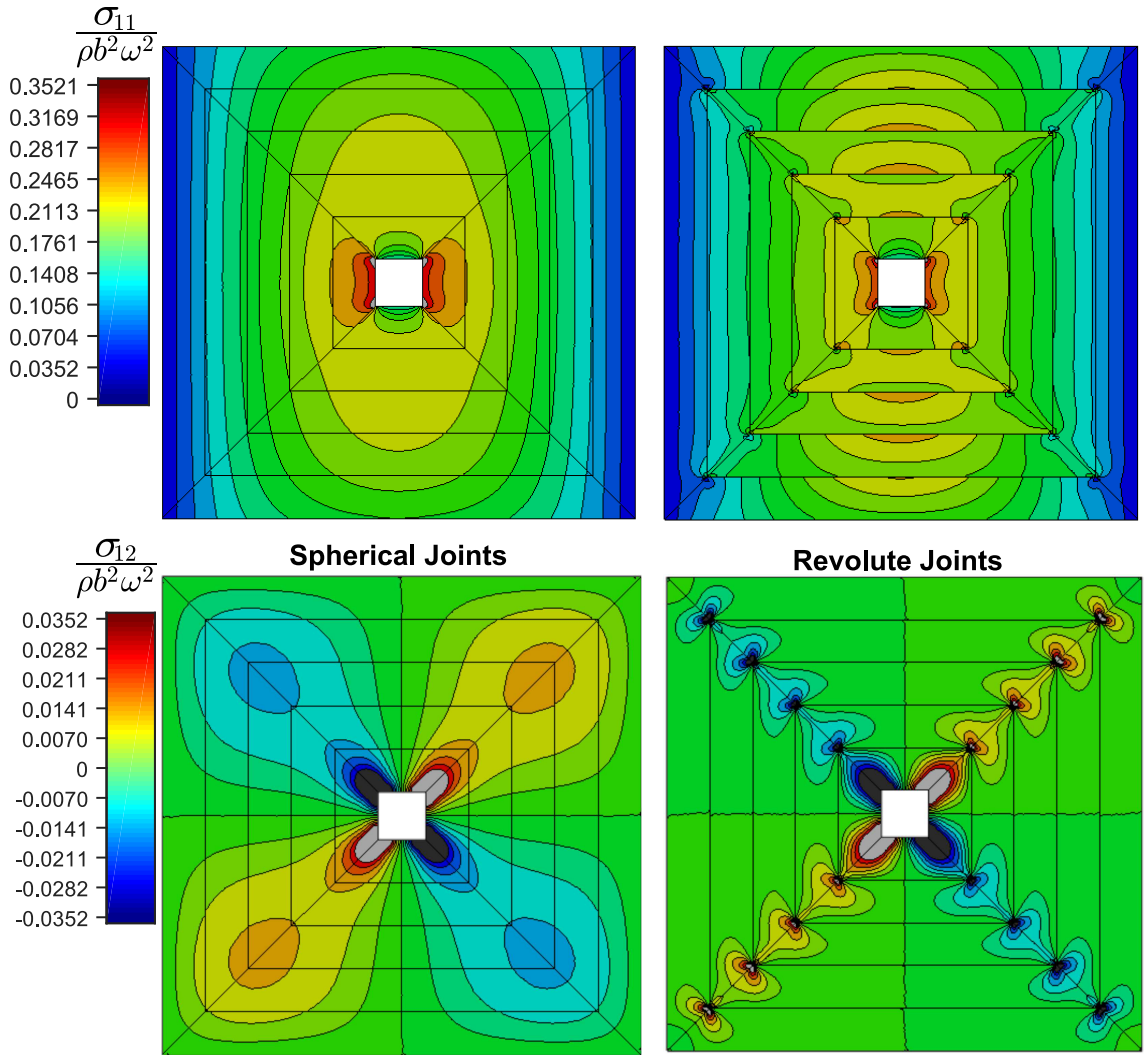

Figure 4.6: Dimensionless in-plane stress components for α=0.1, ν=0.34, and n=5. The components 1 and 2 are, respectively, horizontal and vertical.

4.4.1 Spherical Joints

A linear frequency analysis of such a spacecraft is performed for α=0.1 and ν=0.34 and increasing Ω from 0.08 to 400. Figure 4.8 shows the results for n=2 (solid line) compared to a uniform membrane (dashed line).

The results are in log scale to highlight three behaviors delimited by the red lines. At low Ω (meaning low angular velocity or thick panels) except for the lowest frequency, the slope of the frequency curve is -1. This is characteristic of the behavior of a static plate whose dimensional natural frequencies is independent of the angular velocity. At high angular velocity the slope is zero. This is characteristic of a spinning membrane's behavior whose dimensional frequency is proportional to the angular velocity. The mode with zero slope at

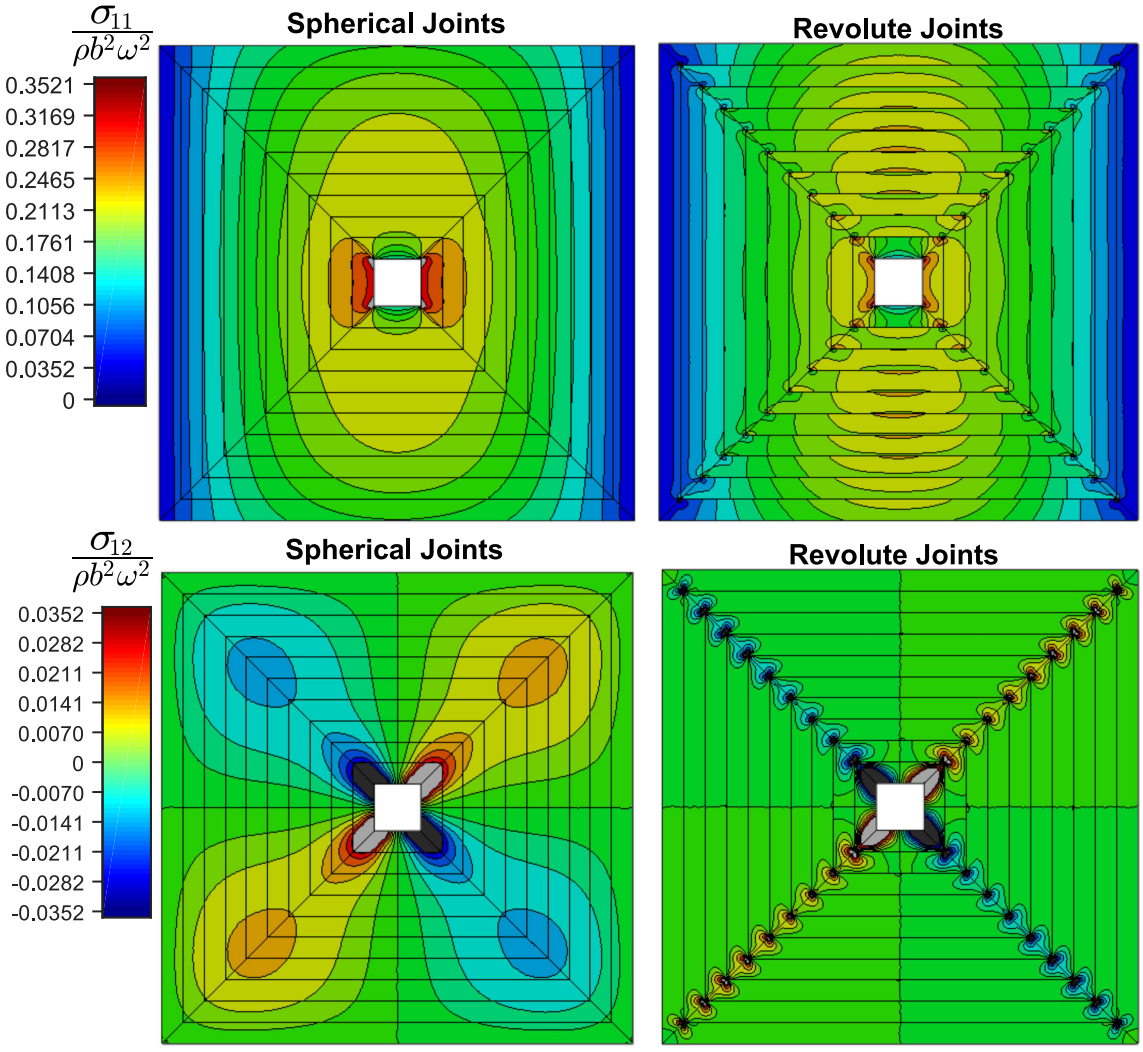

Figure 4.7: Dimensionless in-plane stress components for α=0.1, ν=0.34, and n=10.

low angular velocity thus exhibits a "membrane behavior". This corresponds to the unconstrained degree of freedom Figure 4.9a due to the hinge with zero stiffness. As angular velocity is increased there is a transition and overall the coefficient of proportionality decreases (lower curve). The lowest mode shapes for low and high Ω are shown in Figure 4.9.

Let us now study the influence of n on these results. Figure 4.10 shows the results for n=2, 5, 10, 20, and homogeneous membranes. As n increases there are more degrees of freedom in the unconstrained case, and n-1 horizontal asymptotes at low angular velocities. Overall the membrane behavior is reached for the same Ω=50 limit (considering only the first few modes). Overall the transition between hinged plate and uniform membrane occurs at the same time as the transition between uniform plate and uniform membrane.

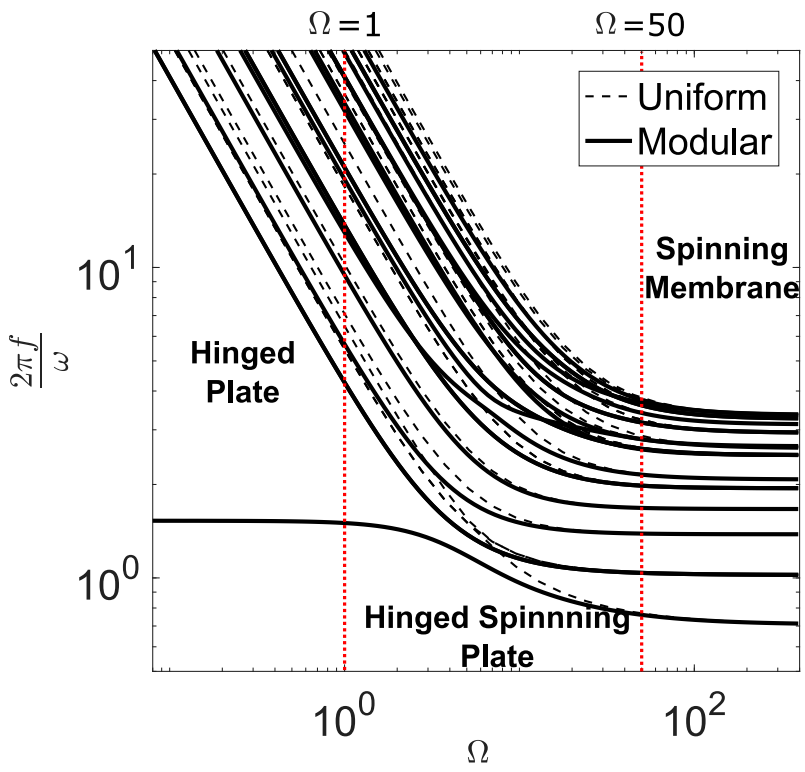

Figure 4.8: Frequency (in the rotating frame) for increasing Ω for a uniform spacecraft and a modular one with n=2.

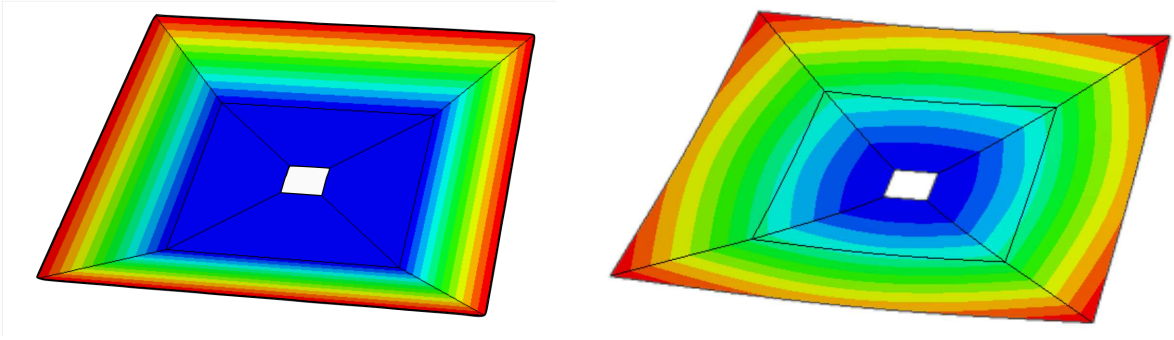

(a) Ω ≤1.

(b) Ω ≥50.

Figure 4.9: Mode shapes at increasing Ω.

4.4.2 Revolute Joints

Figure 4.11 shows the same graph but with sliding hinges. Overall we see the same behavior, but this time at high Ω we do not recover the membrane behavior. In fact, the asymptotes for uniform and modular structures are different and even more so as the number of n increases. This is due to the observation in

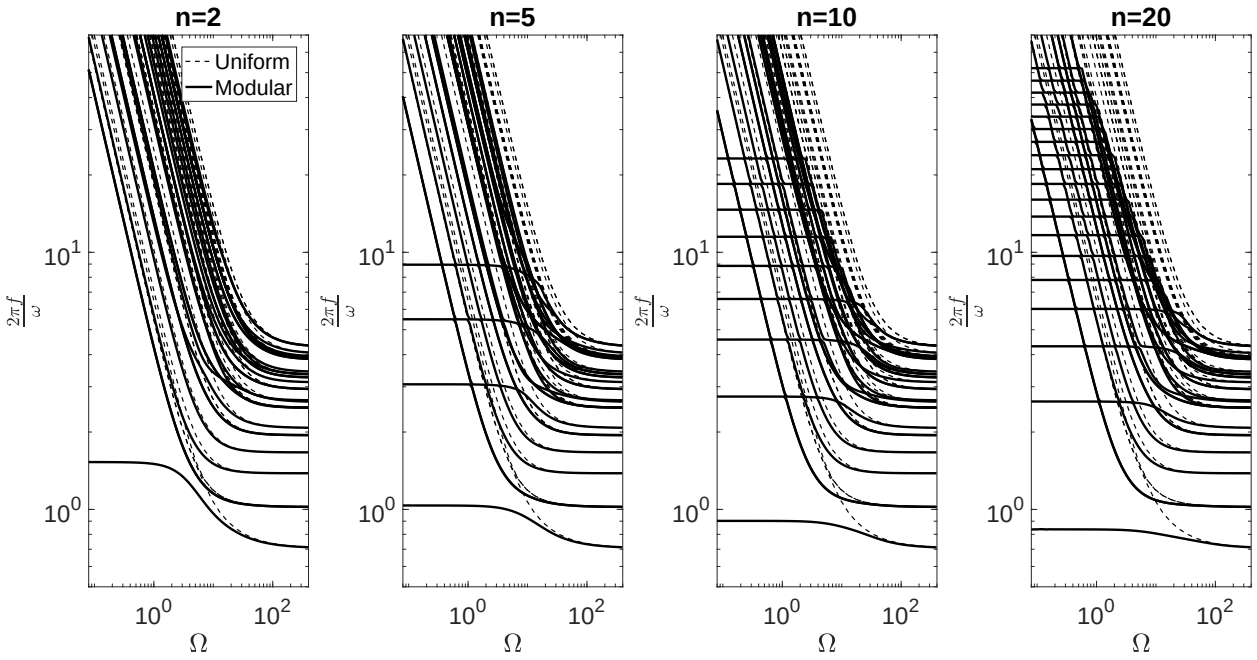

Figure 4.10: Influence of Ω on the frequencies (in the rotating frame) of spinning spacecraft with hinged panels for different topologies (n) for α=0.1 and ν=0.34 and compared to uniform membranes.

Section 4.3. The in-plane stress, which is dominant in this range of low bending stiffness, is modified in the case of sliding hinges compared to a uniform structure.

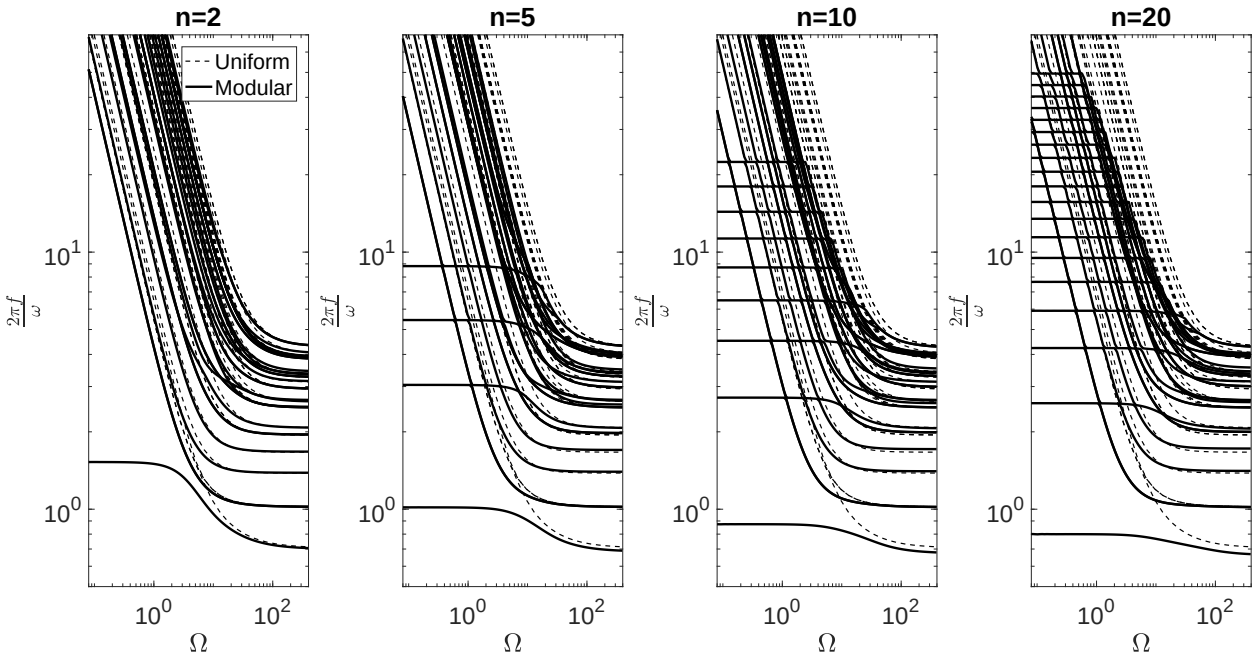

Figure 4.11: Influence of Ω on the frequencies (in the rotating frame) of spinning spacecraft with sliding hinged panels for different topologies (n), α=0.1 and ν=0.34 and compared to uniform membranes.

4.4.3 Potential Application

These results could be applied to a simplified model of the IKAROS solar sail by JAXA shown in Figure 4.12. IKAROS is a 20 m diagonal thin spacecraft with n=18 polyimide film panels (whose properties are suppose equal to Kapton) that is spinning at about 1 rpm. The hub to membrane ratio is assumed to be α=0.1. This spacecraft also has stiffening elements and tip masses but those component are ignored here.

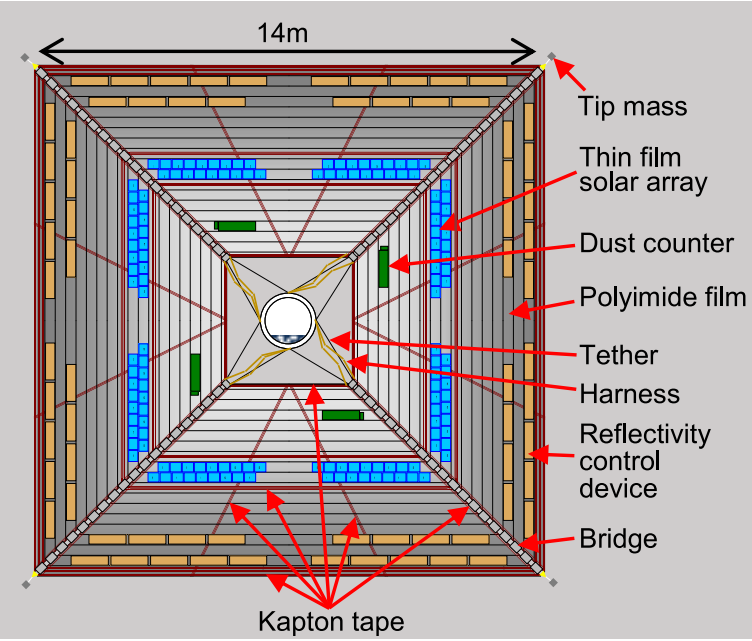

Figure 4.12: IKAROS solar sail concept (Okuizumi et al., 2017).

The hinges between the panels are spherical hinges. We find that the spacecraft would have to be at least 0.5 mm thick for the bending stiffness and the panels to influence the natural frequencies. The thickness of the polyimide film panels is 7.5 μm (Sawada et al., 2007), and therefore the linear mechanics of this spacecraft is that of a uniform membrane.

4.5 Conclusion

In this chapter a generic FEM model and its implementation in Abaqus/Standard of hinged membranes or origami packageable structures has been presented. A preliminary analysis of such structures in terms of stress distribution and out-of-plane frequencies confirms physical intuitions: fixed hinges do not influence the stress distribution while sliding hinges do. The consequence of this observation is that at high angular velocity, the hinged plates behave like a uniform membrane if the hinges are fixed, and the behavior is slightly different if the hinges are sliding.

In the case of fixed hinges we find that for dimensionless angular velocity Ω above 50, the uniform membrane behavior is recovered. For sliding hinges, the same criterion holds but the effective properties of the "uniform membrane"' are slightly different.

Finally, one advantage of this analysis method is the possibility of implementing various kinds of hinge with properties such as linear or nonlinear elastic stiffness. As a example, one could study the influence of hinge imperfections or damping on the behavior of the structure.

Chapter 5

Finite Element Formulation of Solar Radiation Pressure and its Implementation in Abaqus/Standard

5.1 Introduction and Background

Solar radiation pressure can become the dominant load for thin structures in space depending on the orbit and the maneuvers. This load can potentially deform the structure up to buckling (see Chapter 2) or even create flutter instabilities (Dowell, 2011). Solar radiation action on a body is classically modeled as a force with a component parallel to the local normal to the surface and one parallel to the direction of the incoming beam from the sun. The amplitude of the also force depends on the slope at the surface and the properties at the surface. Overall, solar radiation pressure is a deformation-dependent, non-conservative, follower load. This load has been included in many solar sailing studies, for example when considering orbital mechanics and attitude control. McInnes (1999) summarizes the solar sail equations of motion and presents some sun-centered or planet-centered orbits taking into account the influence of solar radiation pressure on the sail. Very often it is modeled as a uniform pressure when studying its influence on the shape of a structure. This is a good approximation when the light beam is transversely to a flat structure. When the beam is at an angle, the situation is very different and special treatment is required. Some studies have been performed in the context of the Heliogyro solar sails (Figure 1.5a), a long (3 km) spinning thin membrane. MacNeal (1971) has studied this concept extensively (MacNeal, 1967) and mentioned the possibility of flutter instability without providing further results. Later this work was expanded by Natori et al. (1989); this was, to our knowledge, the first to calculate solarelastic flutter in the context of spinning beams. More recently Dowell (2011) derived some general equations in the context of plates and drew a parallelism with aerodynamic pressure. Later, Gibbs (2014) studied an additional case of a static tensioned membrane clamped on the edges. In all those examples results were found based on numerical solutions of the PDEs describing each

problem.

As solar radiation pressure conditions are difficult to reproduce on Earth, reliable and efficient simulation tools need to be developed. To our knowledge the only FEM works that simulate solar radiation pressure are from Sakamoto et al. (2007), and Wilkie et al. (2015). Both author only consider perfectly reflective surfaces. In addition in the first reference, the authors express the nodal force but neglect the variation of the amplitude of the load in the expression of the load stiffness, and instead only focuses on equilibrium deflections. The method in the second reference is specifically applied in Abaqus/Standard and relies on dynamic simulations and a combination of subroutines that monitor the local deformation and update the external load accordingly at each increment. This method is reported to be computationally expensive and does not enable fast frequency based estimation of flutter for example. Additionally, in all those examples, only perfectly reflective surfaces are considered. Other examples of applications consider thin solar cells in space for solar power satellites, which would require the analysis of absorbent surfaces as well. In this chapter we derived the FEM formulation of full solar radiation pressure on reflective but also absorbent and diffuse surfaces. We implemented this method in Abaqus/Standard for 3D problems with quadrilateral surface elements on solid or continuum shell mechanical elements. This method enables rapid frequency-based prediction of flutter or buckling among other applications.

Follower load elements have been extensively studied in the finite element method. In this chapter we used the notation and theoretical framework from Wriggers (2008). For the case of solar radiation pressure both the amplitude and the direction of the load depend on the local normal that depends on the deformations. A classical example of this kind of load is fluid-structure interaction, as discussed by multiple authors. Hassler and Schweizerhof (2008) considered the case where internal pressure depends on structural deformations. Scheizerhof and Ekkehard (1984) provided a general discretization of deformation dependent loads.

The aim of this chapter is twofold. First, present the FEM derivation of the solar radiation pressure components on the three types of surfaces: reflective, absorbent and diffuse. Second, derive and test a systematic method to implement deformation-dependent traction in Abaqus/Standard using an UEL subroutine and tie constraints. Each of these methods can be used independently to implement solar radiation pressure load in a different FEM code and to implement different types of deformation-dependent loads in Abaqus/Standard.

We first provide additional details on solar radiation pressure. Then, we recall some aspects of the FEM derivation of external traction force as described by Wriggers (2008). Next, we explicitly derive the discretization of solar radiation pressure on quadrilateral surface elements for the three surface types and report the nodal forces and stiffness sub-matrices. Finally, we introduce a general method to integrate surface load elements in Abaqus/Standard and present a test case on perfectly reflective spinning plate.

5.2 Solar Radiation Pressure Overview

Solar radiation pressure comes from the radiative energy from the sun. It is difficult to model and accurately predict the solar cycle and variation, and thus the intensity of the solar flux. But the changes of sun irradiance are relatively slow. The biggest variation follows the solar cycle which is an 11-year change in the sun activity. Nonetheless, the intensity from the sun at 1 AU is generally estimated at a value of 1361 $W.m^{-2}$, and is inversely proportional to the distance from the sun. The force that it exerts on a spacecraft depends on the properties at the surface and overall is a non-conservative perturbation (McInnes, 1999; Vallado, 2004). The general model for solar force can be expressed based on the normal $\boldsymbol{n}$, the surface area da, the direction of the incoming beam $\boldsymbol{s}$, the properties of the surface and the force of solar pressure P_{SR}. Figure 5.1 introduces the notation. The solar radiation force is reported in Equations 5.1, 5.2, and 5.3 respectively for absorbent, reflective, and diffuse surfaces.

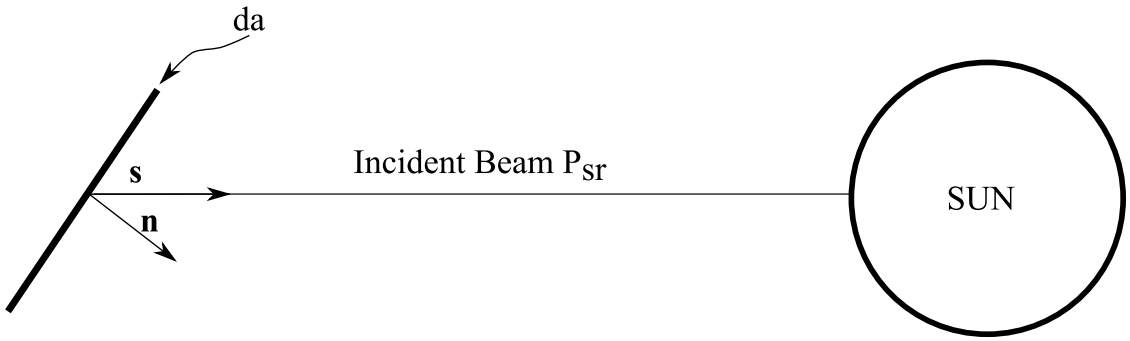

Figure 5.1: Solar pressure diagram and sign convention.

$$dF_a = -P_{SR} c_{Ra} \left(\boldsymbol{s} \cdot \boldsymbol{n}\right) \boldsymbol{s} \; da \tag{5.1}$$

$$dF_{rs} = -2P_{SR} c_{Rs} \left(\boldsymbol{s} \cdot \boldsymbol{n}\right)^2 \boldsymbol{n} \; da \tag{5.2}$$

$$dF_{rd} = -P_{SR} c_{Rd} \left(\boldsymbol{s} \cdot \boldsymbol{n}\right) \left(\frac{2}{3}\boldsymbol{n} + \boldsymbol{s}\right) da \tag{5.3}$$

where c_{Ra} is the coefficient of absorption and c_{Rs} and c_{Rd} are respectively the diffuse and specular reflectivities, such that:

$$c_{Ra} + c_{Rs} + c_{Rd} = 1.0 \tag{5.4}$$

The solar radiation force is the sum of those three components:

$$dF_{SP} = dF_a + dF_{rs} + dF_{rd} \tag{5.5}$$

We rewrite the solar radiation pressure the following way to capture the three specific deformation-dependent load components to be implemented in FEM:

$$dF_{SP} = p_1 \left(\boldsymbol{s} \cdot \boldsymbol{n}\right)^2 \boldsymbol{n} da + p_2 \left(\boldsymbol{s} \cdot \boldsymbol{n}\right) \boldsymbol{s} da + p_3 \left(\boldsymbol{s} \cdot \boldsymbol{n}\right) \boldsymbol{n} da \tag{5.6}$$

where:

$$p_1 = -2 P_{SR} c_{Rs} \tag{5.7}$$

$$p_2 = -P_{SR} \left(c_{Ra} + c_{Rd}\right) \tag{5.8}$$

$$p_3 = -\frac{2}{3} P_{SR} c_{Rd} \tag{5.9}$$

5.3 Surface Loading in FEM

In this section we describe the main steps in deriving surface loading in FEM as explained by Wriggers (2008) and we introduce the notations and interpolation functions. We restrict ourselves to 3D problems with quadrilateral surface elements and continuum elements whose degrees of freedom at each node are the displacements. We also consider that the traction only depends on the first derivative of the nodal position, in particular, local normal, and thus use bilinear interpolation functions. The results in the particular case of solar radiation pressure will be presented in the Section 5.4. In order to characterize a load element, the nodal force and stiffness sub-matrices are defined. First, the virtual external work due to traction loading is discretized. From this the nodal force $\boldsymbol{r_A}$ expression is derived. Then, the virtual external work is linearized and discretized to express the nodal stiffness sub-matrix $\boldsymbol{k_{AB}}$.

Let us introduce the following kinematic notation:

$$\boldsymbol{x} = \boldsymbol{\varphi}\left(\boldsymbol{X}, t\right) \tag{5.10}$$

where $\boldsymbol{X}$ is the position in the initial configuration and $\boldsymbol{x}$ is the position in the current configuration.

After inserting the finite element approximation for the virtual displacements or test function $\boldsymbol{\eta}$, the contribution of the surface traction $\boldsymbol{t}$ which describes the surface loading (Figure 5.2) to the weak form in its current configuration ($g(\boldsymbol{\varphi}, \boldsymbol{\eta})$) is:

$$g\left(\boldsymbol{\varphi}, \boldsymbol{\eta}\right) = \int_{\boldsymbol{\varphi}(\Gamma_\sigma)} \boldsymbol{\eta} \cdot \boldsymbol{t} da \tag{5.11}$$

where Γ_σ is the initial surface subjected to the traction. The surface load shape functions have to be defined

for $d-1$ dimensions, where d is the dimension of the problem (in our case d=3). The ansatz function can

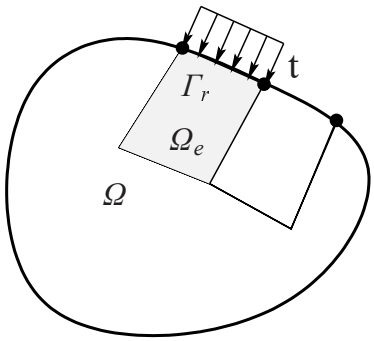

Figure 5.2: Surface loads (Wriggers, 2008) in 2D.

now be used to discretize the weak form:

$$\begin{aligned} g(\boldsymbol{\varphi}, \boldsymbol{\eta}) &= \int_{\boldsymbol{\varphi}(\Gamma_\sigma)} \boldsymbol{\eta} \cdot \boldsymbol{t} da \\ &= \bigcup_{r=1}^{n_r} \sum_{A=1}^{m} \boldsymbol{\eta_A}^T \int_{\varphi(\Gamma_r)} N_A \boldsymbol{t} d\Gamma \\ &= \bigcup_{r=1}^{n_r} \sum_{A=1}^{m} \boldsymbol{\eta_A}^T \boldsymbol{r_A}(\boldsymbol{x_e}) \end{aligned} \tag{5.12}$$

with

$$\boldsymbol{r_A}(\boldsymbol{x_e}) = \int_{\varphi(\Gamma_r)} N_A \boldsymbol{t} d\Gamma \tag{5.13}$$

where n_r is the number of element boundaries where loads are applied, Γ_r is the initial surface of an element subjected to a traction vector $\boldsymbol{t}$, m is the number of nodes per element (in our case m=4), $\{N_A\}_{A\in[1..4]}$ are the interpolation functions and $\{\boldsymbol{\eta_A}\}_{A\in[1..4]}$ are the nodal positions.

To numerically compute the nodal force (Equation 5.13) we use the classical isoparametric mapping. Figure 5.3 illustrates the mapping from isoparametric reference configuration to initial configuration to current configuration for quadrilateral elements. The highest derivative in this weak form comes from the normal vector $\boldsymbol{n}$ and is order 1. We thus use bilinear interpolation functions to approximate the solutions:

$$N_A(\xi, \eta) = \frac{1}{2}(1 + \xi_A \xi)\frac{1}{2}(1 + \eta_A \eta) \tag{5.14}$$

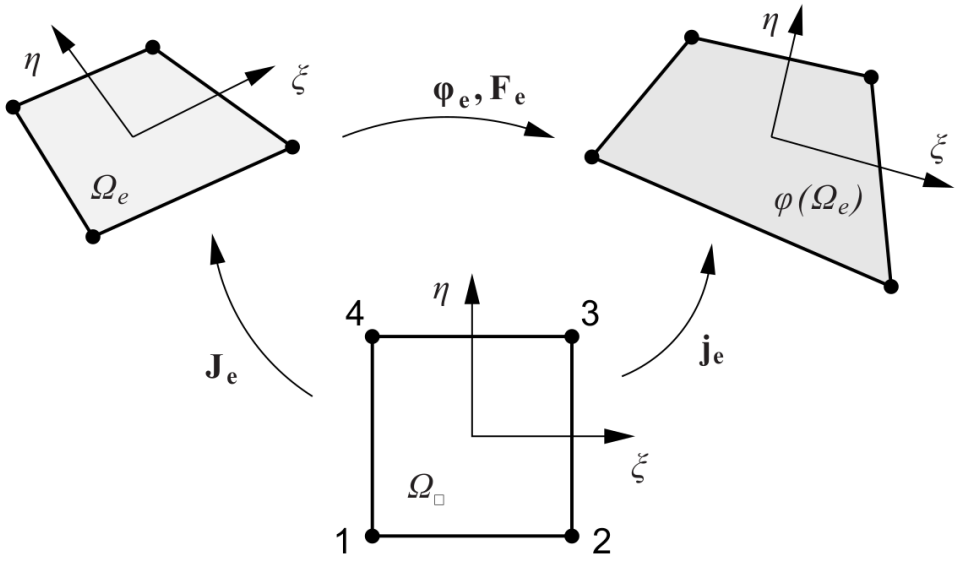

Figure 5.3: Mappping for a 4 nodes element (Wriggers, 2008).

where ξ_A and η_A are the corner coordinates in the reference configuration:

$$\begin{aligned}(\xi_1, \eta_1) &= (-1, -1)\\ (\xi_2, \eta_2) &= (1, -1)\\ (\xi_3, \eta_3) &= (1, 1)\\ (\xi_4, \eta_4) &= (-1, 1)\end{aligned} \tag{5.15}$$

Each node has 3 degrees of freedom in displacement $\boldsymbol{x_A} = (x_{1,A}, x_{2,A}, x_{3,A})$, where $A \in [1...4]$. Using the isoparametric shape functions we have:

$$\boldsymbol{\varphi_e} = \boldsymbol{x_e} = \sum_{A=1}^{4} N_A(\xi, \eta)\, \boldsymbol{x_A} \tag{5.16}$$

and the derivative of the components of the position vector $x_{i,\alpha}$ (where α is either ξ or η):

$$x_{i,\alpha} = \sum_{A=1}^{4} N_A(\xi, \eta)_{,\alpha}\, x_{i,A} \tag{5.17}$$

Let us now express the normal vector according to the nodal degrees of freedom. It is shown (Wriggers,

2008) that the current normal can be expressed according the reference coordinates as:

$$\boldsymbol{n} = \frac{\boldsymbol{\varphi}_{,\boldsymbol{\xi}} \times \boldsymbol{\varphi}_{,\boldsymbol{\eta}}}{||\boldsymbol{\varphi}_{,\boldsymbol{\xi}} \times \boldsymbol{\varphi}_{,\boldsymbol{\eta}}||} \tag{5.18}$$

And the current volume element $d\Gamma$ can be expressed as:

$$d\Gamma = ||\boldsymbol{\varphi}_{,\boldsymbol{\xi}} \times \boldsymbol{\varphi}_{,\boldsymbol{\eta}}|| d\xi d\eta \tag{5.19}$$

The cross product $\boldsymbol{n}_e$ can now be computed:

$$\begin{aligned} \boldsymbol{\varphi}_{,\boldsymbol{\xi}} \times \boldsymbol{\varphi}_{,\boldsymbol{\eta}} &= \begin{bmatrix} x_{2,\xi} x_{3,\eta} - x_{3,\xi} x_{2,\eta} \\ x_{3,\xi} x_{1,\eta} - x_{1,\xi} x_{3,\eta} \\ x_{1,\xi} x_{2,\eta} - x_{2,\xi} x_{1,\eta} \end{bmatrix} \\ &= \boldsymbol{n}_e \end{aligned} \tag{5.20}$$

Thus

$$\boldsymbol{r_A} = \int_{-1}^{1} \int_{-1}^{1} N_A \boldsymbol{t} ||\boldsymbol{\varphi}_{,\boldsymbol{\xi}} \times \boldsymbol{\varphi}_{,\boldsymbol{\eta}}|| d\xi d\eta \tag{5.21}$$

Let us now linearize the virtual external work (Equation 5.11) to define $\boldsymbol{k_{AB}}$:

$$\lim_{\epsilon \to 0} \frac{d}{d\epsilon} g\left(\boldsymbol{\varphi} + \epsilon \triangle \boldsymbol{u}, \boldsymbol{\eta}\right) = Dg_p\left(\boldsymbol{\varphi}, \boldsymbol{\eta}\right) \cdot \triangle \boldsymbol{u} \tag{5.22}$$

After discretization we obtain:

$$Dg_p\left(\boldsymbol{\varphi}, \boldsymbol{\eta}\right) \cdot \triangle \boldsymbol{u} = \bigcup_{r=1}^{n_r} \sum_{A=1}^{m} \sum_{B=1}^{m} \boldsymbol{\eta_A}^T \boldsymbol{k_{AB}} \triangle \boldsymbol{u_B} \tag{5.23}$$

In the following section we derive $\boldsymbol{r_A}$ and $\boldsymbol{k_{AB}}$ for the three types of surface properties independently.

5.4 Solar Radiation Pressure Element

To simplify the notation we are first going to differentiate three quantities. The choice of these quantities will become apparent later in the derivation.

The first quantity was differentiated by Wriggers (2008) in the context of uniform pressure:

$$\lim_{\epsilon \to 0} \frac{d}{d\epsilon} \boldsymbol{n_e}\left(\boldsymbol{\varphi} + \epsilon \triangle \boldsymbol{u}\right) = \triangle \boldsymbol{u}_{,\boldsymbol{\xi}} \times \boldsymbol{\varphi}_{,\boldsymbol{\eta}} - \triangle \boldsymbol{u}_{,\boldsymbol{\eta}} \times \boldsymbol{\varphi}_{,\boldsymbol{\xi}} \tag{5.24}$$

with $\boldsymbol{n_e}$ defined in Equation 5.20. This quantity is then discretized using the following ansatz, with $\triangle \boldsymbol{u_B}$ the column vector with the degrees of freedom at node B:

$$\triangle \boldsymbol{u} = \sum_{B=1}^{4} N_B(\xi, \eta) \triangle \boldsymbol{u_B} \tag{5.25}$$

After discretization we obtain:

$$\lim_{\epsilon \to 0} \frac{d}{d\epsilon} \boldsymbol{n_e}(\boldsymbol{\varphi} + \epsilon \triangle \boldsymbol{u}) = \sum_{B=1}^{4} (N_{B,\xi} \boldsymbol{N_{1,\eta}} - N_{B,\eta} \boldsymbol{N_{1,\xi}}) \triangle \boldsymbol{u_B} \tag{5.26}$$

with

$$\boldsymbol{N_{1,\alpha}} = \begin{bmatrix} 0 & x_{3,\alpha} & -x_{2,\alpha} \\ -x_{3,\alpha} & 0 & x_{1,\alpha} \\ x_{2,\alpha} & -x_{1,\alpha} & 0 \end{bmatrix} \tag{5.27}$$

Secondly:

$$\lim_{\epsilon \to 0} \frac{d}{d\epsilon} (\boldsymbol{s} \cdot \boldsymbol{n_e}(\varphi + \epsilon \triangle \boldsymbol{u})) = \boldsymbol{s} \cdot (\triangle \boldsymbol{u_{,\xi}} \times \boldsymbol{\varphi_{,\eta}} - \triangle \boldsymbol{u_{,\eta}} \times \boldsymbol{\varphi_{,\xi}}) \tag{5.28}$$

After discretization we obtain:

$$\lim_{\epsilon \to 0} \frac{d}{d\epsilon} (\boldsymbol{s} \cdot \boldsymbol{n_e}(\boldsymbol{\varphi} + \epsilon \triangle \boldsymbol{u})) = \sum_{B=1}^{4} \left(N_{B,\xi} \boldsymbol{\Phi^T_{1,\eta}} - N_{B,\eta} \boldsymbol{\Phi^T_{1,\xi}} \right) \triangle \boldsymbol{u_B} \tag{5.29}$$

and

$$\boldsymbol{\Phi_{1,\alpha}} = \begin{bmatrix} s_3 \varphi_{2,\alpha} - s_2 \varphi_{3,\alpha} \\ s_1 \varphi_{3,\alpha} - s_3 \varphi_{1,\alpha} \\ s_2 \varphi_{1,\alpha} - s_1 \varphi_{2,\alpha} \end{bmatrix} \tag{5.30}$$

Finally:

$$\lim_{\epsilon \to 0} \frac{d}{d\epsilon} (\boldsymbol{n_e}(\boldsymbol{\varphi} + \epsilon \triangle \boldsymbol{u}) \cdot \boldsymbol{n_e}(\boldsymbol{\varphi} + \epsilon \triangle \boldsymbol{u})) = 2 \boldsymbol{n_e}(\boldsymbol{\varphi}) \cdot (\triangle \boldsymbol{u_{,\xi}} \times \boldsymbol{\varphi_{,\eta}} - \triangle \boldsymbol{u_{,\eta}} \times \boldsymbol{\varphi_{,\xi}}) \tag{5.31}$$

After discretization we obtain:

$$\lim_{\epsilon \to 0} \frac{d}{d\epsilon} (\boldsymbol{n_e}(\boldsymbol{\varphi} + \epsilon \triangle \boldsymbol{u}) \cdot \boldsymbol{n_e}(\boldsymbol{\varphi} + \epsilon \triangle \boldsymbol{u})) = \sum_{B=1}^{4} \left(N_{B,\xi} \boldsymbol{\Phi^T_{2,\eta}} - N_{B,\eta} \boldsymbol{\Phi^T_{2,\xi}} \right) \triangle \boldsymbol{u_B} \tag{5.32}$$

with

$$\boldsymbol{\Phi_{2,\alpha}} = 2 \begin{bmatrix} n_{e3}\varphi_{2,\alpha} - n_{e2}\varphi_{3,\alpha} \\ n_{e1}\varphi_{3,\alpha} - n_{e3}\varphi_{1,\alpha} \\ n_{e2}\varphi_{1,\alpha} - n_{e1}\varphi_{2,\alpha} \end{bmatrix} \tag{5.33}$$

We have now defined all the quantities necessary to express the nodal forces and sub-stiffness matrices of the solar radiation pressure element for the three types of surfaces.

5.4.1 Reflective Surface

In the case of a perfectly reflective surface the traction is:

$$\boldsymbol{t} = p_1 \left(\boldsymbol{s} \cdot \boldsymbol{n}\right)^2 \boldsymbol{n} \tag{5.34}$$

with $\boldsymbol{s} = (s_1, s_2, s_3)$ the incoming light beam direction. Using Equations 5.18 and 5.19 we can write:

$$\boldsymbol{t} d\Gamma = p_1 \frac{\left(\boldsymbol{s} \cdot \boldsymbol{n_e}\right)^2}{\boldsymbol{n_e} \cdot \boldsymbol{n_e}} \boldsymbol{n_e} d\xi d\eta \tag{5.35}$$

Using Equations 5.35 and 5.21 we obtain:

$$\boldsymbol{r}_A \left(\boldsymbol{\varphi_e}\right) = \int_{-1}^{1} \int_{-1}^{1} N_A \left(\xi, \eta\right) p_1 \frac{\left(\boldsymbol{s} \cdot \boldsymbol{n_e}\right)^2}{\boldsymbol{n_e} \cdot \boldsymbol{n_e}} \boldsymbol{n_e} d\xi d\eta \tag{5.36}$$

This can be expressed according to the current coordinates. We did not find a closed form expression for the integral for a general quadrilateral element, so we computed it numerically. We will describe this numerical integration in part 5.4.4.

In order to use iterative solvers to solve the nonlinear problem we need to express the linearization of the virtual work and in particular estimate the element sub-stiffness matrices $\boldsymbol{k_{AB}}$. We recognize in Equation 5.36 the quantities that we have introduced in Equations 5.26, 5.29, and 5.32. We can thus directly state:

$$\boldsymbol{k_{AB}} = \int_{-1}^{1} \int_{-1}^{1} N_A \left(N_{B,\xi} \left(p_a \boldsymbol{N_{1,\eta}} + p_b \boldsymbol{N_{2,\eta}} + p_c \boldsymbol{N_{3,\eta}}\right) - N_{B,\eta} \left(p_a \boldsymbol{N_{1,\xi}} + p_b \boldsymbol{N_{2,\xi}} + p_c \boldsymbol{N_{3,\xi}}\right)\right) d\xi d\eta \tag{5.37}$$

with

$$p_a = p_1 \frac{(\boldsymbol{s} \cdot \boldsymbol{n_e})^2}{\boldsymbol{n_e} \cdot \boldsymbol{n_e}} \tag{5.38}$$

$$p_b = 2p_1 \frac{\boldsymbol{s} \cdot \boldsymbol{n_e}}{\boldsymbol{n_e} \cdot \boldsymbol{n_e}} \tag{5.39}$$

$$p_c = -p_1 \frac{(\boldsymbol{s} \cdot \boldsymbol{n_e})^2}{(\boldsymbol{n_e} \cdot \boldsymbol{n_e})^2} \tag{5.40}$$

and

$$\boldsymbol{N_{2,\alpha}} = \boldsymbol{n_e} \boldsymbol{\Phi}_{\boldsymbol{1,\alpha}}^{\boldsymbol{T}} \tag{5.41}$$

$$\boldsymbol{N_{3,\alpha}} = \boldsymbol{n_e} \boldsymbol{\Phi}_{\boldsymbol{2,\alpha}}^{\boldsymbol{T}} \tag{5.42}$$

with $\boldsymbol{\Phi_{1,\alpha}}$ and $\boldsymbol{\Phi_{2,\alpha}}$ respectively expressed in Equations 5.30 and 5.33.

5.4.2 Absorbent Surface

The case of a perfectly absorbent surface is simpler, as now the traction can be written as:

$$\boldsymbol{t} d\Gamma = p_2 \left(\boldsymbol{s} \cdot \boldsymbol{n_e}\right) \boldsymbol{s} d\xi d\eta \tag{5.43}$$

The nodal force becomes:

$$\boldsymbol{r}_A \left(\boldsymbol{\varphi_e}\right) = \int_{-1}^{1} \int_{-1}^{1} p_2 N_A \left(\boldsymbol{s} \cdot \boldsymbol{n_e}\right) \boldsymbol{s} d\xi d\eta \tag{5.44}$$

and the stiffness sub-matrix is:

$$k_{AB} = \int_{-1}^{1} \int_{-1}^{1} p_2 N_A \left(N_{B,\xi} \boldsymbol{N_{4,\eta}} - N_{B,\eta} \boldsymbol{N_{4,\xi}}\right) d\xi d\eta \tag{5.45}$$

with

$$\boldsymbol{N_{4,\alpha}} = \boldsymbol{s} \boldsymbol{\Phi}_{\boldsymbol{1,\alpha}}^{\boldsymbol{T}} \tag{5.46}$$

and $\boldsymbol{\Phi_{1,\alpha}}$ expressed in Equation 5.30.

5.4.3 Diffuse Surface

There are two terms for the diffuse surface. One component is parallel to the normal to the surface and the other is parallel to the beam direction. The second one is derived exactly the same way as shown in the case

of perfectly absorbent surface, with $p_2 = -P_{SR}c_{Rd}$ (see Equation 5.8). We therefore focus on the first term:

$$\boldsymbol{t}d\Gamma = p_3 \frac{\boldsymbol{s}\cdot\boldsymbol{n_e}}{||\boldsymbol{n_e}||}\boldsymbol{n_e}d\xi d\eta \tag{5.47}$$

This is similar to the case of a perfectly reflective surface.

The nodal force is:

$$\boldsymbol{r}_A(\boldsymbol{\varphi_e}) = \int_{-1}^{1}\int_{-1}^{1} p_3 N_A \frac{\boldsymbol{s}\cdot\boldsymbol{n_e}}{||\boldsymbol{n_e}||}\boldsymbol{n_e}d\xi d\eta \tag{5.48}$$

The sub stiffness matrix is:

$$\boldsymbol{k_{AB}} = \int_{-1}^{1}\int_{-1}^{1} p_3 N_A \left(N_{B,\xi}\boldsymbol{N_{5,\eta}} - N_{B,\eta}\boldsymbol{N_{5,\xi}}\right) d\xi d\eta \tag{5.49}$$

$$\boldsymbol{N_{5,\alpha}} = p_d\boldsymbol{N_{1,\alpha}} + p_e\boldsymbol{N_{2,\alpha}} + p_f\boldsymbol{N_{3,\alpha}} \tag{5.50}$$

with

$$\begin{aligned} p_d &= p_3\frac{\boldsymbol{s}\cdot\boldsymbol{n_e}}{||\boldsymbol{n_e}||} \\ p_e &= p_3\frac{1}{||\boldsymbol{n_e}||} \\ p_f &= -\frac{1}{2}p_3\frac{\boldsymbol{s}\cdot\boldsymbol{n_e}}{||\boldsymbol{n_e}||^3} \end{aligned} \tag{5.51}$$

and $\boldsymbol{N_{1,\alpha}}$, $\boldsymbol{N_{2,\alpha}}$, and $\boldsymbol{N_{3,\alpha}}$ respectively in Equations 5.27, 5.41 and 5.42.

5.4.4 Numerical Integration

We did not find a closed form solution for the element integrals r_A and k_{AB}. Instead, we implement a numerical integration based on Simpson 2D integration scheme that we briefly summarize here. Let's call $f(\xi,\eta)$ the integrand and $\Omega_\square = \{(\xi,\eta) : -1 \le \xi \le 1, -1 \le \eta \le 1\}$ the domain of integration. The interval [-1,1] is subdivided into N (even number) sub intervals of equal width $h = \frac{2}{N}$ by using equally spaced sample $\xi_i = -1 + ih$ and $\eta_i = -1 + ih$ for i=1,2,...N. The composite Simpson's rule is:

$$\int_{-1}^{1}\int_{-1}^{1} f(\xi,\eta)\, d\xi d\eta \approx \frac{4}{9N^2}\sum_{i=1}^{m+1}\sum_{j=1}^{n+1} W_{ij} f(\xi_i,\eta_j) \tag{5.52}$$

where

$$W = \begin{bmatrix} 1 & 4 & 2 & 4 & \dots & 2 & 4 & 1 \\ 4 & 16 & 8 & 16 & \dots & 8 & 16 & 4 \\ 2 & 8 & 4 & 8 & \dots & 4 & 8 & 2 \\ 4 & 16 & 8 & 16 & \dots & 8 & 16 & 4 \\ \vdots & \vdots & \vdots & \vdots & \dots & \vdots & \vdots & \vdots \\ 2 & 8 & 4 & 8 & \dots & 4 & 8 & 2 \\ 4 & 16 & 8 & 16 & \dots & 8 & 16 & 4 \\ 1 & 4 & 2 & 4 & \dots & 2 & 4 & 1 \end{bmatrix} \tag{5.53}$$

Higher N lead to more precise results and smaller N to faster computations. We have compared the numerical results and the approximated results for different quadrilateral element geometries and N=10 provided good approximations for each case.

5.5 Implementation in Abaqus/Standard

In this section a method to integrate load elements into Abaqus/Standard is presented. This method combines a user defined element subroutine and a tie constraint between "load elements" and "mechanical elements". An UEL subroutine is used to implement the solar pressure element or "load element" as derived in part 5.4. Details are provided in Section 5.5.1. One of the challenges in implementing load elements in Abaqus/Standard was to add stiffness and nodal force to existing elements without having to implement our own mechanical elements. This effectively means decoupling load elements and mechanical elements to be able to access Abaqus libraries. We explain this method in Section 5.5.2. The objective is to perform static and complex frequency analysis for buckling and flutter estimations. We explain how to conduct such an analysis in Section 5.5.3. The Fortran subroutine files and a typical input file can be found in Appendix D.

5.5.1 UEL Subroutine

We used a UEL user subroutine to define the solar pressure load elements (Simulia, 2013b). This subroutine is called for each element defined by this UEL subroutine and each time some element calculations are required. Within this subroutine we evaluate the nodal force and stiffness matrices. As we use quadrilateral element in 3D we have 12 degrees of freedom within an element. The nodal force is a vector of size 12 and the matrix size is 12×12. The only two variables we need to define for our purpose are RHS which is effectively $\boldsymbol{r_A}$ and AMATRX, which corresponds to $\boldsymbol{k_{AB}}$. The variables passed to the subroutine are COORDS, an array containing the original coordinates of the nodes of the element, U, an array containing the current

estimates of the basic solution variables (displacements in our case) and some flags defining the procedure type (see part 5.5.3).

We have implemented three subroutines: for perfectly reflective, perfectly absorbent, and perfectly diffuse surfaces separately. In each case the solar pressure is characterized by three constants, the solar pressure modulated by the properties of the surface p_i (with i=1,2 or 3 depending on the surface type as in Equations 5.7, 5.8, 5.9), and the direction $\boldsymbol{s} = (s_1, s_2, s_3)$ of the incoming light beam with $s_1^2 + s_2^2 + s_3^2 = 1$. The subroutine properties are three positive or negative float numbers: p_i, s_1 and s_2.

Effectively, the following parameters are used in the UEL subroutine: MCRD (number of d.o.f. per node)=3, NNODE (number of nodes per element)=4, and NDOFEL (total number of d.o.f. in an element)=12. The relation between $\boldsymbol{r_A}$ and RHS and $\boldsymbol{k_{AB}}$ and AMATRX are:

$$\begin{cases} RHS(k_1) = r_A\,(ii) \\ A = \text{floor}((k_1 - 1)/3) + 1 \\ ii = \text{mod}(k_1 - 1, 3) + 1 \end{cases}$$

and

$$\begin{cases} AMATRX(k_1, k_2) = -k_{AB}\,(ii, jj) \\ A = \text{floor}((k_1 - 1)/3) + 1 \\ B = \text{floor}((k_2 - 1)/3) + 1 \\ ii = \text{mod}(k_1 - 1, 3) + 1 \\ jj = \text{mod}(k_2 - 1, 3) + 1 \end{cases}$$

The properties of the element are defined in the input file. We specified that the subroutine element has 4 nodes, unsymmetric stiffness matrix (use the option UNSYMM) and 3 properties to be defined. The degrees of freedom we use are the displacements which correspond to the components 1, 2, and 3. This corresponds to the following lines in the input file (a full input file can be found in Appendix D Section D.3 as an example).

```
*USER ELEMENT, NODES=4, UNSYMM, TYPE=U1, I PROPERTIES=0,PROPERTIES=3
 1, 2, 3
```

The element properties are specified in the order (p_i, s_1, s_2) as follows:

```
*UEL PROPERTY, ELSET=Set-2
 0.01, 0.7071, 0.0
```

5.5.2 Tie Constraint

Now that we have developed an UEL subroutine we need to integrate it into Abaqus mechanical models. We used tie constraints to add stiffness and nodal force from solar pressure element to an existing Abaqus

model. The idea is to create a new 3D surface part that matches the surface of the object on which the load is applied both in geometry and mesh. As we have implemented the subroutine for quadrilateral elements the surface of the object needs to be meshed accordingly. One can use for example hexahedral continuum shell elements for thin objects or hexahedral elements for 3D objects. This is illustrated Figure 5.4a for thin continuum shell elements and Figure 5.4b for solid elements. The load elements are in red and mechanical elements from Abaqus libraries in green.

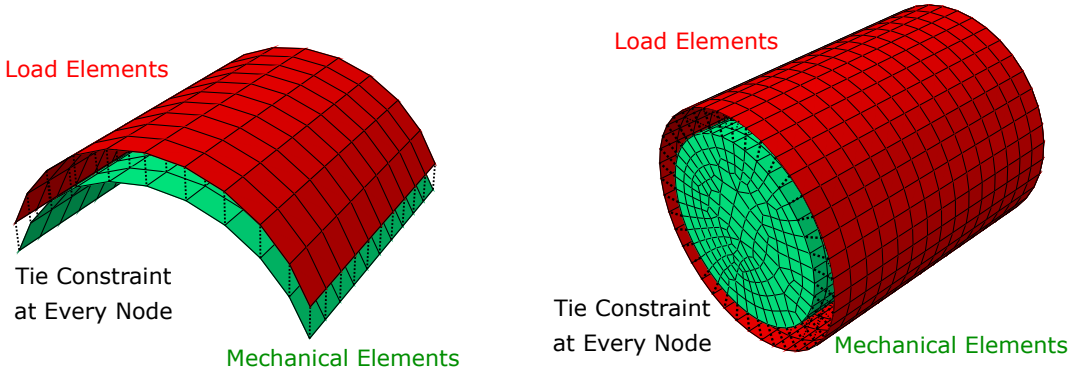

(a) Thin continuum shell mechanical elements.

(b) Solid mechanical elements.

Figure 5.4: The red elements are the load elements whose geometry and mesh match the object (in green) surface. There is effectively no separation between red and green surfaces. The thin dotted lines represent the tie constraint at every node.

Since the load elements are surface elements, a convention on the positive normal direction needs to be introduced. Abaqus by default uses the convention in Figure 5.5. Since the normal Equation 5.20 might not be in the proper direction (relative to the object these surface elements are attached to), the direction $\boldsymbol{s}$ must be chosen such that the overall force on the object is in the modeled direction.

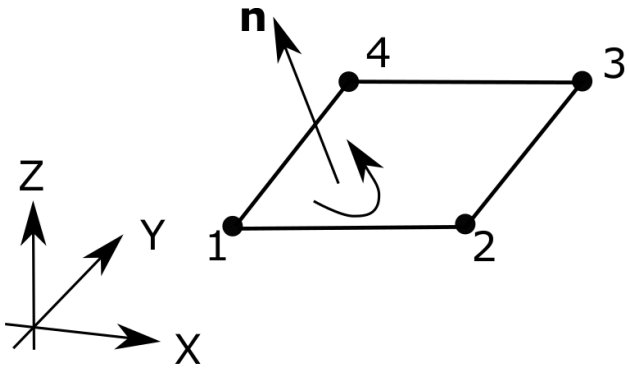

Figure 5.5: Abaqus surface elements convention.

The load and mechanical parts are then connected using a surface based tie constraint: the mesh tie constraint (Simulia, 2013a). Each node on the slave (load) surface is constrained to have the same motion

as the point on the master (mechanical) surface to which it is closest (spot on in our case). We use a nodal region and only constrain the translational degrees of freedom. We implement all boundary conditions and loads (except solar pressure) on the mechanical (master) surface only.

5.5.3 Abaqus Analysis

We want to use this method to estimate equilibria and run frequency-based stability analyses. The subroutine was thus implemented and tested for static and complex frequency analyses. In particular, the amplitude of the pressure is implemented differently for each case and we use flags to differentiate the type of analysis at each step.

5.5.3.1 Static Analysis

For the static analysis and in particular in the nonlinear case the amplitude of the load p_i is linearly increased within the step in order to improve the convergence of the Newton-Raphson algorithm. To this end the target amplitude is multiplied by the current time of the step and the step total time is 1. The flag to be used to identify this analysis is LFLAGS(1).

With this convention, by default solar radiation pressure is incrementally increased at every static step. The static step at which solar pressure is not required or is maintained constant should be identified in the subroutine (using KSTEP identifier) and p_i should respectively be set to 0 and 1. Additionally, by default Abaqus makes the stiffness matrix of the system symmetric. We need to specify an unsymmetric stiffness matrix during the static step using the option unsymm=YES.

5.5.3.2 Complex Frequency Analysis

As the load stiffness can be unsymmetric, the frequency and mode shapes of the structure can be complex. Abaqus can evaluate complex frequency and this analysis type is compatible with UEL subroutines (but does not account for damping from the subroutine, which is not a restriction for our application). In this case, the amplitude of the load p_i is directly specified and not incrementally increased. The flags for frequency and complex frequency analysis are respectively 41 and 47.

The procedure to obtain the complex frequencies is a subspace projection method. First the eigenmodes of the symmetric stiffness matrix are extracted in a frequency analysis. Then the complex eigenfrequency extraction is performed. In order to obtain accurate results, a large enough set of eigenmodes needs to be extracted prior to the complex frequency step and a convergence analysis needs to be carried out.

We have tested this implementation in Abaqus/Standard in the case of a perfectly reflective surface as shown next.

5.6 Test Case: Linear Spinning Clamped Plate

In this section we compare the results from Abaqus using the subroutine to results from exact PDE solutions. The case tested does not represent an actual physical system but offers a benchmark.

A square clamped plate with perfectly reflective surface spinning around the normal axis at its center with incoming light on one side from various directions was considered (Figure 5.6). This problem was solved quasi-statically, i.e., we consider the prestress due to the centrifugal force but assume that the solar radiation pressure does not depend on time (ϕ is fixed).

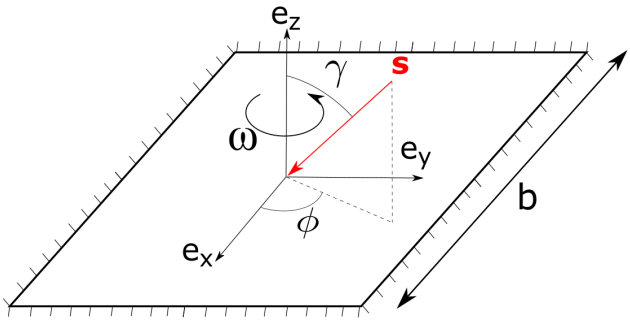

Figure 5.6: Square spinning plate geometry and notations.

First, the linear deflection of the spinning plate with incoming light from various angles was considered. The linear equilibrium equation governing this system (adapted from Dowell (2011)) is:

$$-\lambda^2 \rho h w + D\nabla^4 w + \frac{1}{2}\rho h \omega^2 r^2 \nabla^2 w + \rho h \omega^2 r \frac{\partial w}{\partial r} \\ - p_1 \sin(2\gamma)\left(\cos(\phi)\frac{\partial w}{\partial x} + \sin(\phi)\frac{\partial w}{\partial y}\right) = -p_1 \cos(\gamma)^2 \tag{5.54}$$

where D is the bending stiffness, h is the thickness of the plate, w is the deflection, and σ_c the in-plane stress due to centrifugal force. The boundary conditions are clamped on the outer edge:

$$\begin{aligned} w &= 0 \\ \nabla w \cdot \boldsymbol{n} &= 0 \end{aligned} \tag{5.55}$$

This type of linear problem can be solved in Matlab using the PDE toolbox as shown in Appendix C.

We focus here on the frequency analysis to compare the implementation of the solar pressure load stiffness and test the complex frequency procedure. We only consider the frequency around the flat surface by neglecting the deflection due to the right hand side of Equation 5.54. The associated eigenvalue problem is:

$$-\lambda^2 w + D\nabla^4 w + \frac{1}{2}\rho h \omega^2 r^2 \nabla^2 \bar{w} + \rho h \omega^2 r \frac{\partial w}{\partial r} - p_1 \sin(2\gamma)\left(\cos(\phi)\frac{\partial w}{\partial x} + \sin(\phi)\frac{\partial w}{\partial y}\right) = 0$$

This stiffness in the case of perfectly reflective surface consists of two parts, one due to the "uniform pressure" ($p_a \boldsymbol{N_{1,\eta}}$ in Equation 5.37), and one from the amplitude variation ($p_b \boldsymbol{N_{2,\eta}} + p_c \boldsymbol{N_{3,\eta}}$ in Equation 5.37). Since we have neglected the right hand side in Equation 5.54 in the Matlab model and consider the eigenvalue problem of a flat surface we removed the "uniform load" stiffness in the subroutine.

E	2.5 GPa
ν	0.34
ρ	1420 kg.m^{-3}
h	0.1 mm
b	0.2121 m
γ	$\frac{\pi}{4}$
ϕ	0
ω	500 rpm
p_1	$[0 \cdots 100]$ Pa

Table 5.1: Dimensions and properties of spinning square plate.

The Abaqus model is a plate with SC8R continuum shell elements. We considered a 0.1 mm thick Kapton plate. The properties and dimensions are reported in Table 5.1. Fifty modes were extracted in a frequency step before the complex frequency evaluation. Figure 5.7 shows the frequency evolution while p_1 is increased from 0 Pa to 100 Pa obtained with Abaqus and Matlab. Figure 5.8 presents the nine first mode shapes at p_1=100 Pa obtained with Abaqus Figure 5.8b and Matlab Figure 5.8a. There is perfect agreement between the simulations and the PDE solutions. To test the implementation further and verify that the implementation was independent of the coordinate system, the same problem in different orientations of {plate+incoming light} were solved and the same solutions were found in each case. In addition, several meshes and angles of incidence γ and ϕ have been considered. In each case a perfect agreement between Abaqus and Matlab solutions was found. This confirms the validity of our approach.

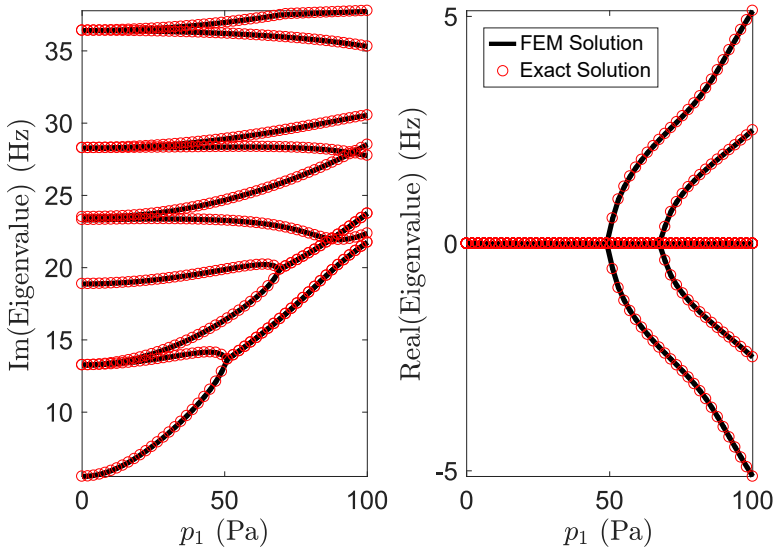

Figure 5.7: Eigenvalue comparison.

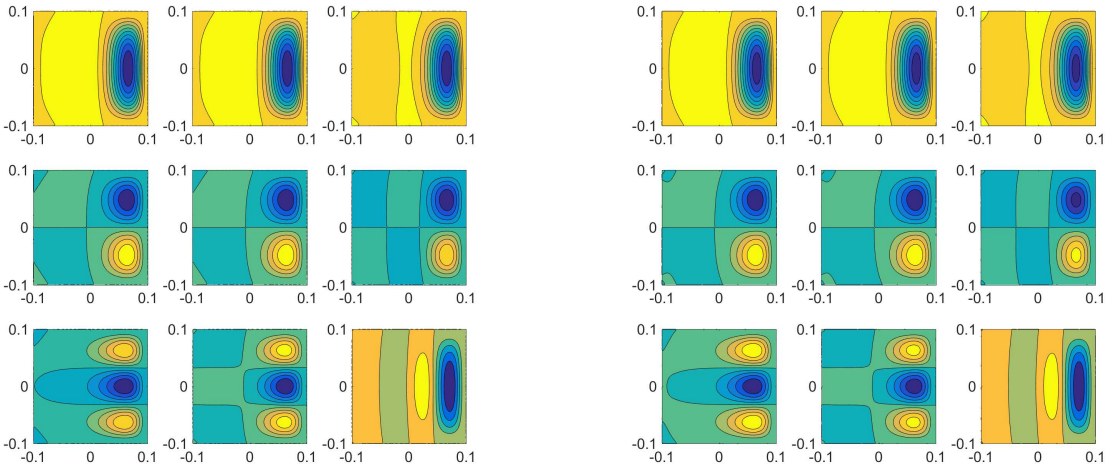

(a) Exact Solution.

(b) FEM Solution.

Figure 5.8: Comparison of the nine first modes of vibration for ω=500 rpm and p_1=100 (Modes are ordered by increasing eigenvalue imaginary part).

5.7 Conclusion

The finite element formulation of solar radiation pressure element has been derived for the cases of perfectly reflective, perfectly absorbent, and perfectly diffuse surfaces for 3D problems and quadrilateral surface elements. The nodal force and the sub-matrices were explicitly written in terms of the nodal displacements and a method to implement this load in Abaqus/Standard was introduced. This method relies on the combina-

tion of user element subroutine and a tie constraint method that decouples the implementation of the load elements and mechanical elements. The general FEM derivation of solar radiation pressure can be implemented in any FEM code. The technique to integrate deformation-dependent loads in Abaqus can be used with different external load element subroutines. In this regard, those two parts could be treated independently. The external load element stiffness is found to be unsymmetric. Details on the Abaqus analysis for unsymmetrical stiffness matrices including the deformation-dependent external load methods were presented for the cases of static linear and nonlinear analyses and complex frequencies analyses. Finally this method was compared against PDE solutions. We found an excellent match between the two results confirming the validity of our approach.

Unlike previous implementations of solar radiation pressure in Abaqus, this method enables quick flutter or buckling estimations based on frequency analysis. This method was only tested for static and complex frequency analysis but it is expected that minor modifications would enable dynamic analysis as well. This work could be extended for a shell formulation of the pressure load by using the same tie constraint (with adding constraints on the rotational degrees of freedom). A different implementation of the load element taking into account all the degrees of freedom at the nodes would need to be derived. Additional future work could be to develop techniques to deal with shadows. A first extension to the subroutine would be to monitor the sign of the normal relative to the incoming beam to locally differentiate between sides exposed to the sun and those in the shadow. More advanced extensions could include ray-tracing techniques.

This new capability can be used in the design of large structures in space with incoming solar radiation pressure for which simple PDE solutions cannot be found (structures with multiple components, anisotropy, and complex geometries).

Chapter 6

Conclusion

6.1 Summary

Chapter 2 of this thesis has focused on the buckling of spinning membranes under transverse uniform loading. Transverse uniform body forces acting on a spinning membrane induce deflections much greater than the membrane thickness, and these deflections are associated with a compressive hoop stress around the edge of the membrane. This hoop stress can buckle the membrane, resulting in a series of azimuthal wrinkles. A general formulation of the problem has been presented in terms of the dimensionless load G and dimensionless angular velocity Ω, and the critical values of G and Ω have been numerically estimated. For $\Omega < 1$, G_{crit} depends only on the bending stiffness of the membrane (bending dominated behavior), and hence it is constant with G. For $\Omega > 10$, we recover the results of the membrane theory, namely, that wrinkling depends only on the mid-plane stress, and hence G increases with the cube of Ω (in-plane dominated behavior). Both of these specific numerical limits increase if the ratio between inner and outer radius of the membrane, α, is increased. A generic FEM algorithm based on the steps of the analytical methods has been implemented and the results match perfectly with the analytical results. This algorithm has then been used to derive a wide range of results with different dimensionless parameters. An experimental setup has been described and digital image correlation was used to measure the equilibrium shapes of the structure pre and post-buckling. A good match has been found between experimental data and analytical predictions.

Chapter 3 has focused on the axysymmetric nonlinear vibration of a symmetrically deflected spinning membrane. A reduced order model using von Kármán plate equations was derived. The nonlinear coefficients of the equivalent oscillator have been explicitly formulated. It is shown that these coefficients depend on four dimensionless parameters: the dimensionless angular velocity Ω, dimensionless gravity load G, the Poisson's ratio ν, and the inner to outer radius ratio α. We find that the oscillator is a single well Helmholtz-Duffing oscillator, while results from the literature on axisymmetric nonlinear vibrations of flat spinning annulus predict a Duffing oscillator. Thus the deflection of the membrane fundamentally alters its nonlinear

behavior and introduces a quadratic term in the restoring force. The general steady-state solutions of such oscillators have been reported. It is shown that at high angular velocities and for small amplitudes of excitation the membrane exhibits a hardening behavior while a softening behavior characterizes the oscillations at high angular velocities. A threshold between hardening and softening at low amplitudes of excitations was numerically computed for a wide range of dimensionless parameters. A generic finite element method in Abaqus/Standard that simulates the nonlinear oscillations of deflected spinning membranes has been presented. We find that such simulations require a fine time step and appropriate damping coefficients. The tuned values corresponding to the experimental sample are reported. A post-processing technique on the decay response of the oscillator has been used to estimate the backbone curve from the simulations. An excellent agreement between simulations and analytical results has been found. Finally, an experimental setup that decoupled translational and rotational motions has been presented and laser vibrometry has been used the measure the deflection of the membrane during slow frequency sweeps. The experiments show a very good agreement with the theory and the discrepancies were attributed to initial curvature of the sample.

Chapter 4 has presented a short parametric analysis for one type of origami packageable structure. Such structures are characterized by a series of hinged panels. A FEM model in Abaqus/Standard of hinges between plates with various properties has been presented. Two particular hinges have been studied further: fixed hinges with one degree of freedom and sliding hinges. Several intuitive results have been described in terms of stress distribution and natural frequencies of vibration. The hinged structures stress and frequencies are then compared against results for uniform membranes with the same geometry. It is shown that when all the in-plane degrees of freedom at the hinges are constrained, the hinges do not affect the in-plane stress distribution. It is found that for dimensionless angular velocities Ω higher than 50, the hinges don't affect the frequencies of the structure that then behaves like a uniform membrane. It is also shown that in the case of sliding hinges (one in-plane degree of freedom unconstrained), the in-plane stress distribution is modified and consequently the natural frequencies are different from those of a uniform plate even at high angular velocities. At high angular velocities it is shown that the linear behavior of the structure is the same as the one on a uniform membrane with different effective properties.

Finally, in Chapter 5, the Finite Element formulation of solar radiation pressure in the case of perfectly reflective, perfectly absorbent, and perfectly diffuse surfaces, for 3D problems, and quadrilateral surface elements has been derived. We have formulated, for each case, the load element nodal forces and the sub-matrices. We show that this follower load leads to an unsymmetric external load stiffness. We then have introduced a method to implement this load in Abaqus/Standard. This method relies on a UEL subroutine and tie constraints. We have explained how to deal with the unsymmetric matrix and, in particular, how to run static and complex frequency analysis in this case. Finally we have compared Abaqus results with

Matlab solutions on a benchmark case of spinning plates and for a wide range of parameters. We found a perfect match between the two results, thus validating our approach.

6.2 Contribution

Unique contributions to the field of space structures have been made.

- We have derived master curves on the wrinkling of spinning membranes under transverse uniform load that span a wide range of design parameters and can be used to define the minimum angular velocity of spinning thin spacecraft required to avoid wrinkling under solar radiation pressure or transverse maneuvers. In addition, we show that pre-buckled, axisymmetric deflections alter the dynamics of the structure. In particular, a spinning spacecraft excited at axisymmetric resonance and large amplitude present hardening behavior at low angular velocity due to the deflection of the structure. In addition, we show that increasing the angular velocity can limit jump phenomena or multiplicity of the steady state solutions, making the behavior more predictable.

- Generic FEM methods applicable to different geometries and material properties have been presented to compute the nonlinear buckling limits and the coefficients of nonlinear vibrations.

- An experimental setup for studying spinning membrane-like space structures has been presented and two measuring techniques, Stereo Digital Image Correlation and laser vibrometry, have been used and compared. The resulting setup and measuring techniques can be used to study and characterize arbitrary spinning space structure designs.

- Generic FEM methods to implement origami packageable structures have been developed in Abaqus. Several types of hinges with different degrees of freedom and properties can be implemented using the same approach. We show that at high angular velocities perfect hinges don't alter the linear behavior of the structures. Sliding hinges also present a uniform membrane behavior at high angular velocities but with different effective properties.

- Finally, we have derived and implemented a general approach to deal with deformation-dependent solar radiation pressure. This implementation enables equilibrium analysis and frequency-based stability analysis of complex space structures. This new capability enables rapid solarelastic flutter predictions for future classes of large membrane-like space structures.

6.3 Follow-On Work

There are many potential avenues in terms of future work to understand, model, and control the dynamics and stability of spinning flexible membranes.

- The new FEM capability could be used to further study the influence of solar pressure on thin spinning disks in more realistic structures, and could be extended to shell elements and dynamic simulations.
- In addition, more realistic hinges with various stiffness and imperfections and damping could be studied with the Abaqus hinges model, as many properties can be added to the connector elements. In addition to the frequency analysis, some nonlinear deflection or buckling analysis could be performed.
- Using the experimental setup presented in this thesis, both the deployment and dynamics of spinning origami membrane structures could be studied.
- The nonlinear vibrations of spinning membranes under oblique solar radiation pressure at critical speed could be studied further. Some reduced order models similar to those introduced Chapter 3 could be developed and tested against FEM simulations using the new solar radiation pressure elements.
- Going further, one could study the coupling between orbital mechanics and structure deformation.

Bibliography

Arya, M. (2016). Packaging and deployment of large planar spacecraft structures. *Caltech Thesis*.

Arya, M., Lee, N., and Pellegrino, S. . (2015). Wrapping thick membranes with slipping folds. *2nd AIAA Spacecraft Structures Conference, 5-8 January 2015, Kissimmee, FL. AIAA 2015-0682*.

Arya, M., Lee, N., and Pellegrino, S. (2016). Ultralight structures for space solar power satellites. *SciTech 2016, San Diego, AIAA-2016-1950*.

Arya, M., Lee, N., and Pellegrino, S. (2017). Crease-free biaxial packaging of thick membranes with slipping folds. *International Journal of Solids and Structures, doi 10.1016/j.ijsolstr.2016.08.013*, 108(24-39).

Barasch, S. and Chen, Y. (1972). On the vibration of a rotating disk. *Journal of Applied Mechanics*.

Benedettini, F. and Rega, G. (1987). Non-linear dynamics of an elastic cable under planar excitation. *International Journal of Non-Linear Mechanics*, 22:497–509.

Benson, R. (1983). Observation on the steady-state solution of an extremely flexible spinning disk with a transverse load. *Journal of Applied Mechanics*, 50:525–530.

Benson, R. and Bogy, D. (1978). Deflection of a very flexible spinning disk due to a stationary transverse load. *Transactions of ASME*, 45:636–642.

Caltech (2015). Space based solar power project funded (http://www.caltech.edu/news/space-based-solar-power-project-funded-46644).

Chen, J. and Fang, Y. (2011). Warping of stationary and rotating heavy disks. *International Journal of Solids and Structures*, 48:3032–3040.

Ciarlet, P. G. (1980). A justification of the von Kármán equations. *Archive for Rational Mechanics and Analysis*, 73.

Clampin, M. (2008). Status of the James Webb Space Telescope (JWST). *Proceedings of SPIE, Space Telescopes and Instrumentation 2008: Optical, Infrared, and Millimeter*.

Cole, K. and Benson, R. (1988). A fast eigenfunction approach for computing spinning disk deflections. *Journal of Applied Mechanics*, 54:453–456.

Dowell, E. H. (2011). Can solar sails flutter? *The American Institute of Aeronautics and Astronautics Journal*, 46(6).

Eversman, W. (1968). Transverse vibrations of a clamped spinning membrane. *The American Institute of Aeronautics and Astronautics Journal*.

Ewins, D. J. (2000). Modal testing. *Research Studies Press*.

Gärdsback, M. and Tibert, G. (2009). Deployment control of spinning space webs and membranes. *Journal of Guidance, Control and Dynamics*, 32(5).

Gibbs, S. C. (2014). Stability of beams, plates and membranes due to subsonic aerodynamic flows and solar radiation pressure. *Ph.D. Thesis*.

Gunnar, T. and Gärdsback, M. (2009). Space webs, final report. *ESA Technical Report*.

Hassler, M. and Schweizerhof, K. (2008). On the static interaction of fluid and gas loaded multi-chamber systems in large deformation finite element analysis. *Computer Methods in Applied Mechanics and Engineering*, 197:17251749.

Holmes, P. and Rand, D. A. (1976). The bifurcation of duffing's equation: an application of catastrophe theory. *Journal of Sound and Vibration*.

JAXA (2010). Small solar power sail demonstrator "IKAROS".

Jerke, J. M. and Heuth, A. R. J. (1968). The geometric properties of an expandable whirling-membrane solar-energy concentrator. *NASA Technical Note NASA TN D-4532*.

Johnson, L., Young, R., Montgomery, E., and Alhorn, D. (2010). Status of solar sail technology within NASA. *Advances in Space Research*, 48:16871694.

Kovacic, I. and Brennan, M. (2011). The duffing equation. *Wiley*.

Kyser, A. C. (1965). Uniform-stress spinning filamentary disk. *The American Institute of Aeronautics and Astronautics Journal*, 3(7):1313–1316.

Londoño, J., Neild, S., and Cooper, J. A. (2015). Identification of backbone curves of nonlinear systems from resonance decay response. *Journal of Sound and Vibration*, 348:224–238.

MacNeal, R. H. (1967). The Heliogyro an interplanetary flying machine. *Astro Research Coorporation*.

MacNeal, R. H. (1971). Structural dynamics of the Heliogyro. *NASA technical note NASA CR 1745*.

McInnes, C., R. (1999). Solar sailing: Technology, dynamics and mission applications. *Praxis Publishing*.

Melnikov, V. M. and Koshelev, V. A. (1998). Large space structures formed by centrifugal forces. *Earth Space Institute Book Series*, 4.

Mori, O., Shirasawa, Y., Miyazaki, Y., Sakamoto, H., Hasome, M., Okuizumi, N., Sawada, H., Furuya, H., Matunaga, S., Natori, M., Tsuda, Y., Saiki, T., Funase, R., Mimasu, Y., and Kawaguchi, J. (2012). Deployment and steering dynamics of spinning solar sail IKAROS. *22nd International Symposium on Space Flight Dynamics, So Jos dos Campos, Brazil, February, 2011 Journal of Aerospace Engineering, Sciences and Applications*, 4(4).

Moussessian, A., Del Castillo, L., Bach, V., Grando, M., Quijano, U., Smith, P., and Zawadzki, M. (2011). Large aperture, scanning, L-band SAR.

Nakasuka, S., Funase, R., Nakada, K., Kaya, N., and Mankins, J. C. (2006). Large membrane furoshiki satellite applied to phased array antenna and its sounding rocket experiment. *Acta Astronautica*, 58(8):395–400.

NASA (2006). STS-116 shuttle mission imagery (https://spaceflight.nasa.gov/gallery/images/shuttle/sts-116/html/iss014e10084.html).

NASA (2015). Explore James Webb Space Telescope: the sunshield (https://jwst.nasa.gov/sunshield.html).

Natori, M., Nemat-Nasser, S., and Mitsugi, J. (1989). Stability of beams, plates and membranes due to subsonic aerodynamic flows and solar radiation pressure.

Nayfeh, A. H. (2000). *Nonlinear Interations:Analytical,Computational, and Experimental Methods*. Wiley, New York.

Nayfeh, A. H., Jilani, A., and Manzione, P. (2001). Transverse vibrations of a centrally clamped rotating circular disk. *Nonlinear Dynamics*, 26:163–178.

Nowinski, J. (1964). Nonlinear transverse vibrations of a spinning disk. *Journal of Applied Mechanics*, pages 72–78.

Okuizumi, N. (2007). Equilibrium of a rotating circular membrane under transverse distributed load. *Journal of System Design and Dynamics*, 1(1):85–95.

Okuizumi, N. (2009). Vibration mode analysis of a rotating circular membrane under transverse distributed load. *Journal of Design and Dynamics*, 3(1):95–105.

Okuizumi, N. (2014). Forced vibration experiments of a rotating extremely thin circular membrane. *Mechanical Engineering Journal*.

Okuizumi, N., Satou, Y., Mori, O., Sakamoto, H., and Furuya, H. (2017). Investigation of the deformation and stiffness of spinning solar sail membrane of IKAROS. *AIAA SciTech Forum, 9 - 13 January 2017, Grapevine, Texas, 4th AIAA Spacecraft Structures Conference*.

Raman, A. and Mote, C. (1999). Non-linear oscillations of circular plates near a critical speed resonance. *Journal of Non-Linear Mechanics*, 34:139–157.

Raman, A. and Mote, C. (2001). Experimental studies on the non-linear oscillations of imperfect circular disks spinning near critical speed. *International Journal of Non-Linear Mechanics*.

Rega, G., Vestroni, F., and Benedettini, F. (1984). Parametric analysis of large amplitude free vibrations of a suspended cable. *International Journal of Solids and Structures*, 20(2):95–105.

Renshaw, A. A. (1998). Critical speed for floppy disks. *Transactions of ASME*, 65(0):116–120.

Renshaw, A. A. and Mote, C. D. (1995). A perturbation solution for the flexible rotating disk: Nonlinear equilibrium and stability equilibrium under transverse loading. *Journal of Sound and Vibration*, 183(2):309326.

Renshaw, A. A. and Mote, C. D. (1996). Local stability of gyroscopic systems near vanishing eignevalues. *Transactions of the American Society of Mechanical Engineers*, 63:116–120.

Sakamoto, H., Miyazaki, Y., and Mori, O. (2011). Transient dynamic analysis of gossamer-appendage deployment using nonlinear finite element method. *Journal of Spacecraft and Rockets*, 48(5).

Sakamoto, H., Park, K. C., and Miyazaki, Y. (MayJune 2007). Finite element modeling of sail deformation under solar radiation pressure. *Journal of Spacecraft and Rockets*, 44(3).

Satou, Y., Mori, O., Okuizumi, N., Shirasawa, Y., Furuya, H., and Sakamoto, H. (2015). Deformation properties of solar sail IKAROS membrane with nonlinear finite element analysis. *2nd AIAA Spacecraft Structures Conference*.

Sawada, H., Mori, O., Okuizumi, N., Shirasawa, Y., Miyazaki, Y., Natori, M., Matunaga, S., Furuya, H., and Sakamoto, H. (2007). Mission report on the solar power sail deployment demonstration of IKAROS. *52nd AIAA/ASME/ASCE/AHS/ASC Structures, Structural Dynamics and Materials Conference*.

Scheizerhof, K. and Ekkehard, R. (1984). Displacement dependent pressure loads in nonlinear finite element analysis. *Computers & Structures*, 18(6):1099–1114.

Schuerch, H. U. and Hedgepeth, J. M. (October 1968). Large low-frequency orbiting radio telescope. *NASA Contractor Report, CR-1201*, 3(1):95–105.

Simmonds, J. (1962a). The finite deflection of a normally loaded, spinning, elastic membrane. *Journal of Aerospace Sciences*, 29(1):16–18.

Simmonds, J. (1962b). The transverse vibrations of a flat spinning membrane. *Journal of the Aerospace Sciences, http://dx.doi.org/10.2514/8.9297*, 29:16–18.

Simulia (2013a). Abaqus analysis user's guide.

Simulia (2013b). Abaqus user subroutines reference guide.

Soares, R. and Gonçalves, P. (2012). Nonlinear vibrations and instabilities of a stretched hyperelastic annular membrane. *International Journal of Solids and Structures*, 49:514526.

Tatematsu, Y., Suzuki, T., Yamazaki, M., and Miyazaki, Y. (2017). Verification of the similarity rules for spin deployment membrane in the ground experiment. *AIAA SciTech Forum, 9-13 January 2017, Grapevine, Texas,* 4^{th} *AIAA Spacecraft Structures Conference.*

Tobias, S. A. and Arnold, R. N. (1957). The influence of dynamical imperfection of vibration of rotating disks. *Proceedings of the Institution of Mechanical Engineers.*

Torii, T. and Yasuda, K. (1998). Nonlinear forced oscillation of a rotating disk excited at a point fixed in space. *The Japanese Society of Mechanical Engineering International Journal.*

Vallado, D. A. (2004). *Fundamentals of Astrodynamics and Applications (Third Edition)*. Space Technology Library.

Vandeparre, H., Pineirua, M., Brau, F., Roman, B., Bico, J., Gay, C., Bao, W., Lau, C., Reis, P., and Damman, P. (2011). Wrinkling hierarchy in constrained thin sheets from suspended graphene to curtains. *Physical Review Letter*, 106.

Wilkie, W. K., Warren, J. E., Horta, L. G., Lyle, K. H., Juang, J. N., Gibbs, S. C., Dowell, E. H., Guerrant, D. V., and Lawrence, D. (2015). Recent advances in Heliogyro solar sail structural dynamics, stability, and control research. *2nd AIAA Spacecraft Structures Conference.*

Wong, Y. W. and Pellegrino, S. (1999a). Wrinkled membranes part I: experiments, doi: 10.2140/jomms.2006.1.3. *Journal of Mechanics of Materials and Structures*, 1(1):3–25.

Wong, Y. W. and Pellegrino, S. (1999b). Wrinkled membranes part III: numerical simulations, doi: 10.2140/jomms.2006.1.63. *Journal of Mechanics of Materials and Structures*, 1(1):63–95.

Wong, Y. W. and Pellegrino, S. (2006). Wrinkled membranes part II: analytical models, doi: 10.2140/jomms.2006.1.27. *Journal of Mechanics of Materials and Structures*, 1(1):27–61.

Wriggers, P. (2008). *Nonlinear Finite Element Methods*. Springer.

Yamazaki, M. and Miyazaki, Y. (2011). Low-order model of spin type solar sail dynamics by empirical model reduction. *52nd AIAA/ASME/ASCE/AHS/ASC Structures, Structural Dynamics and Materials Conference 19th 4 - 7 April 2011, Denver, Colorado*.

Zhao, J., Tian, T., and Hu, H. Y. (2013). Deployment dynamics of a simplied spinning IKAROS solar sail via absolute coordinate based method. *Acta Mechanica Sinica*, 29(1):132–142.

Appendix A

Wave Number Estimation and Filtering

In order to estimate the wavelength of the equilibrium shapes at different angular velocities in Chapter 2, we project the shape onto the first modes of a static plate, clamped at the hub and free on the outer edge, defined on the same annulus geometry (same α). Let us call $W_{n,m}$ the mode with n nodal diameters and m nodal circles and normalized such that:

$$\int_0^{2\pi} \int_a^b W_{n,m}^2 \, r dr \, d\theta = 1 \tag{A.1}$$

Those shapes form an orthonormal basis for the 2D functions defined on those annulus and that satisfy the same clamped-free boundary conditions. In particular, they are an orthonormal basis for the transverse component of deflection w of the spinning membranes for small amplitudes of deflection. This is the range where the wave number is difficult to estimate. This projection method is also used to filter out the random noise that we discus in Appendix B.

The projection on each mode defines $c_{n,m}$ as:

$$c_{n,m} = \int_0^{2\pi} \int_a^b w_{eq} W_{n,m} \, r dr \, d\theta \tag{A.2}$$

with w_{eq} is the measured equilibrium shape.

In order to remove the noise we only consider the shapes with $n \in [0 \dots 20]$ and $m \in [1 \dots 8]$. This enables us to estimate $n = 18$ (the theoretical maximum wave number to be observed with our sample choice Table 2.1).

We define the projected shape for a given n as:

$$W_{eq,n} = \sum_{m=1}^{8} c_{n,m} W_{n,m} \tag{A.3}$$

and the associated amplitude as:

$$\text{Amp}_n = \max(W_{eq,n}) \tag{A.4}$$

As the DIC system doesn't correlate up the edges, we choose to extrapolate the data by rescaling the outer edge and filling by zeros close to the inner edge. We illustrate this extrapolation/filtering on two different data sets: one at 1283 rpm (Figure A.1a, Figure A.1b and Figure A.1c) and one at 434 rpm (Figure A.1d, Figure A.1e and Figure A.1f). The data at high speed are noisier for two reasons. First, as the membrane gets flatter at high angular velocity, the noise gets relatively higher. Also, as we spin faster there is more blur, mainly on the outer edge.

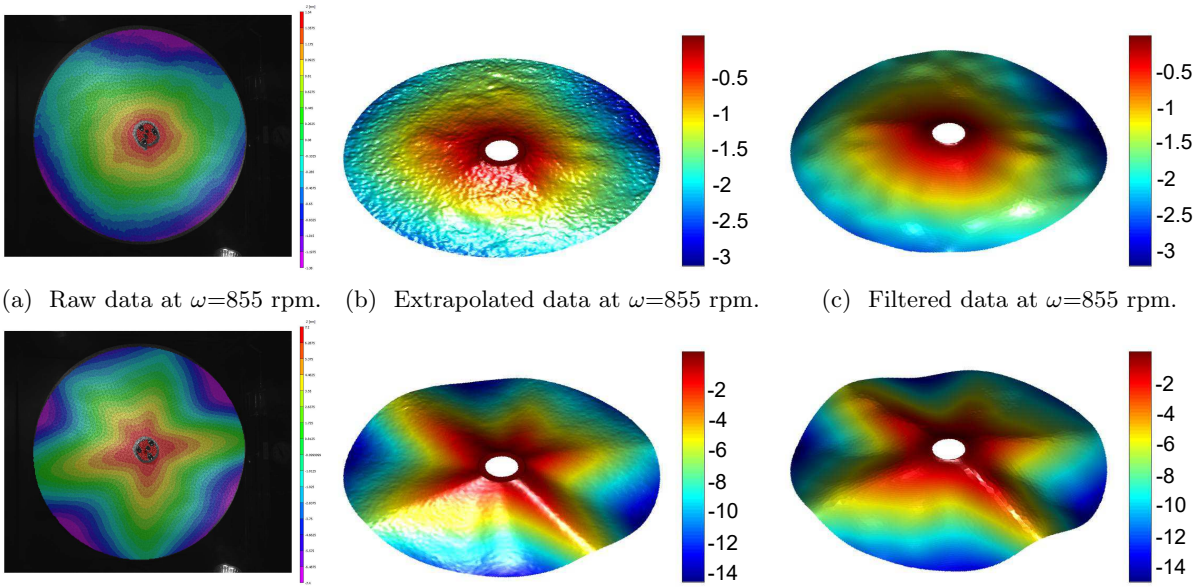

(a) Raw data at ω=855 rpm. (b) Extrapolated data at ω=855 rpm. (c) Filtered data at ω=855 rpm.

(d) Raw data at ω=289 rpm. (e) Extrapolated data at ω=289 rpm. (f) Filtered data at ω=289 rpm.

Figure A.1: Filtering results at high and low angular velocities. Deflection units are mm.

Appendix B

Measurement Precision and Accuracy in Stereo Digital Image Correlation

We performed a "stationary images" test to estimate the errors due to lighting, speckles, and contrast. To this end we took two successive images of the same stationary sample and ran a correlation. Any displacement field between these two images corresponds to an error. This error does not include the blurring due to rotation of the membrane. We obtained a random error with zero mean and a maximum amplitude of about 20 μm on the out-of-plane displacement component. This is set to be our noise level.

A challenge with this setup was to deal with the optical distortions created by the thick (2.54 cm) acrylic lid of the vacuum box. Each camera is looking through the lid at a different angle and at a different location. Each camera thus sees a different rigid body motion and a different optical distortion of the membrane. We corrected for the different rigid body motions by correcting the calibration of the DIC system. The steps to follow within VIC-3D are:

1. Calibration with membrane placed below the acrylic lid.
2. Take images of the membrane from two points at a known distance.
3. The software uses these two points to optimize the camera angles for the lowest projection error from an epipolar line.
4. Run the correlation.

This doesn't correct the optical distortion but reduces the projection error (epipolar error). Next we estimate the error introduced by the lid.

The main source of bias comes from the optical distortion due to the acrylic lid. When a camera takes images through a window with a different refractive index than air, it can produce distorted images. Each camera in the stereo system is looking through a different portion of the lid and at a different angle. They each see a slightly different, slightly distorted membrane. The correlation software estimates the best 3D

shape from those images of slightly different objects. We estimated the error due to distortion plus software by correlating the images of a rigid plate with and without the lid. We show in Figure *B.1* the different components of distortion after removing the rigid body motions (meaning 3D displacement of each point from the results with and without lid, minus overall rigid body motion).

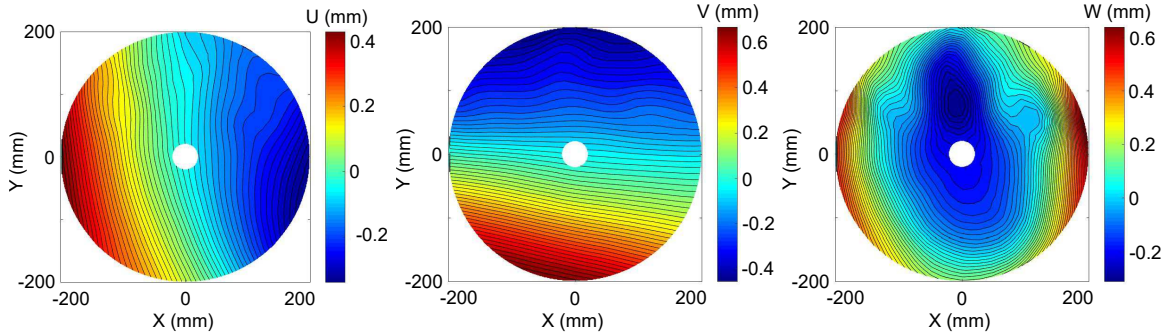

(a) First in plane component. (b) Second in plane component. (c) Out of plane component.

Figure B.1: Measured distortion components.

The bias level in each component is about 0.8 mm. This value is quite high but in this study we are interested in the waviness of the surface and as the distortion is smooth, we consider that it will not affect our results. Figure B.2 shows the different wave numbers of the transverse component of the distortion (Figure B.1c) obtained using the method presented in the next section.

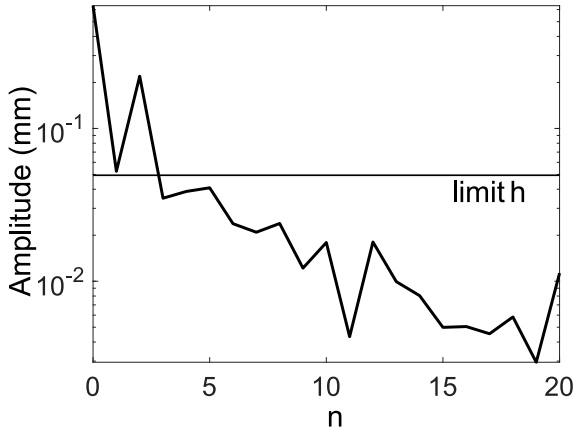

Figure B.2: Dominant wave numbers contained in the lid-induced distortion estimate. The horizontal line gives a reference as $h = 50\mu m$ (smallest membrane thickness considered in this study).

Appendix C

Matlab Solution of Benchmark Problem for Abaqus Subroutine

In this appendix, we present the implementation in Matlab of the equilibrium and frequency problems of a spinning reflective square plate under solar radiation pressure and clamped on the edge. This corresponds to the benchmark problem in Chapter 5 Section 5.6.

C.1 Problem Formulation

The equilibrium equation 5.54 can be written as:

$$D\nabla^4 w - \nabla \cdot ((\sigma_c + \sigma_P) \otimes \nabla w) = -p_1 \cos(\gamma)^2 \tag{C.1}$$

where σ_c is the in-plane stress due to centrifugal force such that:

$$\nabla \cdot \sigma_c = -\rho h \omega^2 \boldsymbol{r} \tag{C.2}$$

and σ_P comes from the deformation-dependent part of solar radiation pressure:

$$\sigma_P = p_1 \sin(2\gamma) \begin{bmatrix} 0 & \sin(\phi)\, x - \cos(\phi)\, y \\ \cos(\phi)\, y - \sin(\phi)\, x & 0 \end{bmatrix}$$

The boundary conditions are clamped on the outer edge:

$$\begin{aligned} \boldsymbol{u} &= 0 \\ w &= 0 \\ \nabla w \cdot \boldsymbol{n} &= 0 \end{aligned} \tag{C.3}$$

The frequencies and mode shapes of the flat plate (neglecting the deflection due to the right hand side) are described by the following equation:

$$-\rho h\lambda^2 w + D\nabla^4 w - \nabla\cdot((\sigma_c + \sigma_P)\otimes\nabla w) = 0$$

C.2 Matlab PDE Toolbok

This type of linear problem can be solved in Matlab using the PDE toolbox (Matlab Documentation). This toolbox solves the following general boundary value problem:

$$\boldsymbol{m}\frac{\partial^2 \boldsymbol{v}}{\partial t^2} + \boldsymbol{d}\frac{\partial \boldsymbol{v}}{\partial t} - \nabla\cdot(\boldsymbol{c}\otimes\nabla\boldsymbol{v}) + \boldsymbol{a}\boldsymbol{v} = \boldsymbol{f} \tag{C.4}$$

and eigenvalue problems of the form:

$$-\nabla\cdot(\boldsymbol{c}\otimes\nabla\boldsymbol{v}) + \boldsymbol{a}\boldsymbol{v} = \boldsymbol{\lambda}\boldsymbol{d}\boldsymbol{v}$$

with either Dirichlet or Neumann boundary conditions:
Dirichlet:

$$\boldsymbol{h}\boldsymbol{v} = \boldsymbol{r}$$

Generalize Neumann:

$$\boldsymbol{n}\cdot(\boldsymbol{c}\nabla\boldsymbol{v}) + \boldsymbol{q}\boldsymbol{v} = \boldsymbol{g}$$

C.3 In-Plane Equilibrium

First the in-plane equilibrium is solved. The unknown is the in-plane displacement $v = u$. We rewrite Equation C.2 into its Matlab form:

$m = d = a = 0$

$$c = \begin{bmatrix} 2G+\mu & 0 & 0 & G \\ 0 & G & \mu & 0 \\ 0 & \mu & G & 0 \\ G & 0 & 0 & 2G+\mu \end{bmatrix}$$

and

$$f = \begin{bmatrix} \rho h \omega^2 x \\ \rho h \omega^2 y \end{bmatrix}$$

where G is the shear modulus and $\mu = \frac{2G\nu}{1-\nu}$. The boundary conditions are Dirichlet boundary conditions, such that:

$$r = \begin{bmatrix} 0 \\ 0 \end{bmatrix}, \; h = \begin{bmatrix} 1 & 0 \\ 0 & 1 \end{bmatrix}$$

From the displacement solution u, the stress components can be calculated:

$$\begin{bmatrix} \sigma_{c,xx} \\ \sigma_{c,yy} \\ \sigma_{c,xy} \end{bmatrix} = \frac{E}{1-\nu^2} \begin{bmatrix} 1 & \nu & 0 \\ \nu & 1 & 0 \\ 0 & 0 & \frac{1-\nu}{2} \end{bmatrix} \begin{bmatrix} u_{1,x} \\ u_{2,y} \\ u_{1,y} + u_{2,x} \end{bmatrix}$$

C.4 Out-of-Plane Equilibrium

In order to solve the fourth order problem describing the deflection we use:

$$\boldsymbol{v} = (w, \nabla^2 w)$$

The following coefficients for the equilibrium equation are used:

$$c = \begin{bmatrix} 1 & 0 & 0 & 0 \\ 0 & 1 & 0 & 0 \\ -\sigma_{c,xx} & -p_1 \sin(2\gamma)\left(\sin(\phi)x - \cos(\phi)y\right) - \sigma_{c,xy} & D & 0 \\ -p_1 \sin(2\gamma)\left(\cos(\phi)y - \sin(\phi)x\right) - \sigma_{c,xy} & -\sigma_{c,yy} & 0 & D \end{bmatrix}$$

$$a = \begin{bmatrix} 0 & 1 \\ 0 & 0 \end{bmatrix}, \; m = 0, \; d = 0, \; f = \begin{bmatrix} 0 \\ p_1 \cos(\phi)^2 \end{bmatrix}$$

We use Neumann boundary conditions to express the condition at the clamped edge. The following coefficients are used:

$$g = \begin{bmatrix} 0 \\ 0 \end{bmatrix}, \; q = \begin{bmatrix} 0 & k \\ 0 & 0 \end{bmatrix}$$

with k=1×10^7.

C.5 Eigenvalue Problem

Finally the egeinvalue problem can be written the same way as the out-of-plane equilibrium but using f=0 and changing d to:

$$d = \begin{bmatrix} 0 & 0 \\ \rho h & 0 \end{bmatrix}$$

Appendix D

UEL Abaqus Subroutine for Solar Radiation Pressure and Generic Input File

We attach here the UEL subroutine of the solar radiation pressure element for reflective and absorbent surfaces as described in Chapter 5 Section 5.4. Those Fortran files can be copied and used directly in Abaqus/Standard. We also show a generic input as described in Chapter 5 Section 5.5.

D.1 Fortran Subroutine for Reflective Surface

```
      SUBROUTINE UEL(RHS,AMATRX,SVARS,ENERGY,NDOFEL,NRHS,NSVARS,
     1 PROPS,NPROPS,COORDS,MCRD,NNODE,U,DU,V,A,JTYPE,TIME,DTIME,
     2 KSTEP,KINC,JELEM,PARAMS,NDLOAD,JDLTYP,ADLMAG,PREDEF,NPREDF,
     3 LFLAGS,MLVARX,DDLMAG,MDLOAD,PNEWDT,JPROPS,NJPROP,PERIOD)
C
      INCLUDE 'ABA_PARAM.INC'
      PARAMETER ( ZERO = 0.D0, HALF = 0.5D0, ONE = 1.D0 )
C
      DIMENSION RHS(MLVARX,*),AMATRX(NDOFEL,NDOFEL),PROPS(*),
     1 SVARS(*),ENERGY(8),COORDS(MCRD,NNODE),U(NDOFEL),
     2 DU(MLVARX,*),V(NDOFEL),A(NDOFEL),TIME(2),PARAMS(*),
     3 JDLTYP(MDLOAD,*),ADLMAG(MDLOAD,*),DDLMAG(MDLOAD,*),
     4 PREDEF(2,NPREDF,NNODE),LFLAGS(*),JPROPS(*),
     5 XI_I(4), Eta_I(4), s(3), ne(3), P_mat(2,6),
     6 Coord_mat(3,4), CW(2), WW(2,2),Vect_ne(3),
     7 S_mat(3,3), dphi_xi(3), dphi_eta(3)
C
      IF (LFLAGS(1)==1) THEN
        p1=PROPS(1)*TIME(1)
      ELSE IF (LFLAGS(1)==41.OR.LFLAGS(1)==47) THEN
```

```
        p1=PROPS(1)
      END IF
      s1=PROPS(2)
      s2=PROPS(3)
      s3=sqrt(1-s1*s1-s2*s2)
      s=(/ s1, s2, s3/)
C
      DO K1 = 1, NDOFEL
        DO KRHS = 1, NRHS
          RHS(K1,KRHS) = ZERO
        END DO
        DO K2 = 1, NDOFEL
          AMATRX(K2,K1) = ZERO
        END DO
      END DO
C
C Current Nodal Coordinates
      x1=COORDS(1,1)+U(1)
      y1=COORDS(2,1)+U(2)
      z1=COORDS(3,1)+U(3)
      x2=COORDS(1,2)+U(4)
      y2=COORDS(2,2)+U(5)
      z2=COORDS(3,2)+U(6)
      x3=COORDS(1,3)+U(7)
      y3=COORDS(2,3)+U(8)
      z3=COORDS(3,3)+U(9)
      x4=COORDS(1,4)+U(10)
      y4=COORDS(2,4)+U(11)
      z4=COORDS(3,4)+U(12)
C
      Xi_I=(/ -1, 1, 1, -1 /)
      Eta_I=(/ -1, -1, 1, 1 /)
      Coord_mat=reshape ( (/ x1, y1, z1, x2, y2, z2, x3, y3, z3, x4, y4,
     & z4 /), (/ 3, 4 /) )
      P_mat=reshape ( (/ 1, 2, 2, 1, 3, 3, 1, 2, 2, 1, 3, 3/),
     &(/ 2, 6 /) )
      S_mat=reshape ( (/ 0, -1, 1, 1, 0, -1, -1, 1, 0/),
     &(/ 3, 3 /) )
C Integration Constants
      Korder=10
      CW=(/ 4, 2 /)
      WW=reshape ( (/ 16, 8, 8, 4 /), (/ 2, 2 /) )
C
      IF (JELEM==50.AND.KSTEP==1.AND.KINC==1) THEN
        PRINT *,'Using SolarPressure.for'
      END IF
```

```
C
C Nodal Force
C
      DO K1=1,NDOFEL
        Ka=(K1-1)/3+1
        Kk=mod(K1-1,3)+1
        ETA_A=Eta_I(Ka)
        XI_A=Xi_I(Ka)
C
        rA=0
        DO KI=0,Korder
          DO KJ=0,Korder
            xi=-1+KI*2.0/Korder
            eta=-1+KJ*2.0/Korder
            IF ((KI==0.AND.KJ==0).OR.(KI==0.AND.KJ==Korder).OR.
     &(KI==Korder.AND.KJ==0).OR.(KI==Korder.AND.KJ==Korder)) THEN
              W=1
            ELSE IF (KI==0.OR.KI==Korder) THEN
              W=CW(mod(KJ-1,2)+1)
            ELSE IF (KJ==0.OR.KJ==Korder) THEN
              W=CW(mod(KI-1,2)+1)
            ELSE
              W=WW(mod(KI-1,2)+1,mod(KJ-1,2)+1)
            END IF
C Define vector Vect_n_e=(Vect_ne_1,Vect_ne_2,Vect_ne_3)
            Vect_ne_1=(z1*(0.25*xi - 0.25) - 1.0*z2*(0.25*xi + 0.25) +
     & z3*(0.25*xi + 0.25) - 1.0*z4*(0.25*xi - 0.25))*(0.25*y1*(
     &eta - 1.0) - 0.25*y2*(eta - 1.0) + 0.25*y3*(eta + 1.0) - 0
     &.25*y4*(eta + 1.0)) - 1.0*(y1*(0.25*xi - 0.25) - 1.0*y2*(0
     &.25*xi + 0.25) + y3*(0.25*xi + 0.25) - 1.0*y4*(0.25*xi - 0
     &.25))*(0.25*z1*(eta - 1.0) - 0.25*z2*(eta - 1.0) + 0.25*z3
     &*(eta + 1.0) - 0.25*z4*(eta + 1.0))
            Vect_ne_2=(x1*(0.25*xi - 0.25) - 1.0*x2*(0.25*xi + 0.25) +
     & x3*(0.25*xi + 0.25) - 1.0*x4*(0.25*xi - 0.25))*(0.25*z1*(
     &eta - 1.0) - 0.25*z2*(eta - 1.0) + 0.25*z3*(eta + 1.0) - 0
     &.25*z4*(eta + 1.0)) - 1.0*(z1*(0.25*xi - 0.25) - 1.0*z2*(0
     &.25*xi + 0.25) + z3*(0.25*xi + 0.25) - 1.0*z4*(0.25*xi - 0
     &.25))*(0.25*x1*(eta - 1.0) - 0.25*x2*(eta - 1.0) + 0.25*x3
     &*(eta + 1.0) - 0.25*x4*(eta + 1.0))
            Vect_ne_3=(y1*(0.25*xi - 0.25) - 1.0*y2*(0.25*xi + 0.25) +
     & y3*(0.25*xi + 0.25) - 1.0*y4*(0.25*xi - 0.25))*(0.25*x1*(
     &eta - 1.0) - 0.25*x2*(eta - 1.0) + 0.25*x3*(eta + 1.0) - 0
     &.25*x4*(eta + 1.0)) - 1.0*(x1*(0.25*xi - 0.25) - 1.0*x2*(0
     &.25*xi + 0.25) + x3*(0.25*xi + 0.25) - 1.0*x4*(0.25*xi - 0
     &.25))*(0.25*y1*(eta - 1.0) - 0.25*y2*(eta - 1.0) + 0.25*y3
     &*(eta + 1.0) - 0.25*y4*(eta + 1.0))
```

```
            Vect_ne=(/ Vect_ne_1, Vect_ne_2, Vect_ne_3/)
            rA=rA+W*(ETA_A*eta + 1.0)*((XI_A*xi)/4.0 + 0.25)*p1*(s1*
     &Vect_ne_1+s2*Vect_ne_2+s3*Vect_ne_3)**2/(Vect_ne_1**2+Vect_ne_2
     &**2+Vect_ne_3**2)*Vect_ne(Kk)
          END DO
        END DO
        RHS(K1,1)=4.0/9.0/Korder/Korder*rA
      END DO
C
C Stiffness Sub-Matrix
C
      DO K1=1,NDOFEL
        DO K2=1,NDOFEL
          Ka=(K1-1)/3+1
          Kb=(K2-1)/3+1
          Kk=mod(K1-1,3)+1
          Kl=mod(K2-1,3)+1
          ETA_A=Eta_I(Ka)
          ETA_B=Eta_I(Kb)
          XI_A=Xi_I(Ka)
          XI_B=Xi_I(Kb)
          Kalpha=P_mat(1,Kl+1)
          Kbeta=P_mat(1,Kl+2)
          Kgamma=P_mat(2,Kl+Kk)
          rK=0
          DO KI=0,Korder
            DO KJ=0,Korder
              xi=-1+KI*2.0/Korder
              eta=-1+KJ*2.0/Korder
              IF ((KI==0.AND.KJ==0).OR.(KI==0.AND.KJ==Korder).OR.
     &(KI==Korder.AND.KJ==0).OR.(KI==Korder.AND.KJ==Korder)) THEN
                W=1
              ELSE IF (KI==0.OR.KI==Korder) THEN
                W=CW(mod(KJ-1,2)+1)
              ELSE IF (KJ==0.OR.KJ==Korder) THEN
                W=CW(mod(KI-1,2)+1)
              ELSE
                W=WW(mod(KI-1,2)+1,mod(KJ-1,2)+1)
              END IF
            Vect_ne_1=(z1*(0.25*xi - 0.25) - 1.0*z2*(0.25*xi + 0.25) +
     & z3*(0.25*xi + 0.25) - 1.0*z4*(0.25*xi - 0.25))*(0.25*y1*(
     &eta - 1.0) - 0.25*y2*(eta - 1.0) + 0.25*y3*(eta + 1.0) - 0
     &.25*y4*(eta + 1.0)) - 1.0*(y1*(0.25*xi - 0.25) - 1.0*y2*(0
     &.25*xi + 0.25) + y3*(0.25*xi + 0.25) - 1.0*y4*(0.25*xi - 0
     &.25))*(0.25*z1*(eta - 1.0) - 0.25*z2*(eta - 1.0) + 0.25*z3
     &*(eta + 1.0) - 0.25*z4*(eta + 1.0))
```

```
      Vect_ne_2=(x1*(0.25*xi - 0.25) - 1.0*x2*(0.25*xi + 0.25) +
     & x3*(0.25*xi + 0.25) - 1.0*x4*(0.25*xi - 0.25))*(0.25*z1*(
     &eta - 1.0) - 0.25*z2*(eta - 1.0) + 0.25*z3*(eta + 1.0) - 0
     &.25*z4*(eta + 1.0)) - 1.0*(z1*(0.25*xi - 0.25) - 1.0*z2*(0
     &.25*xi + 0.25) + z3*(0.25*xi + 0.25) - 1.0*z4*(0.25*xi - 0
     &.25))*(0.25*x1*(eta - 1.0) - 0.25*x2*(eta - 1.0) + 0.25*x3
     &*(eta + 1.0) - 0.25*x4*(eta + 1.0))
      Vect_ne_3=(y1*(0.25*xi - 0.25) - 1.0*y2*(0.25*xi + 0.25) +
     & y3*(0.25*xi + 0.25) - 1.0*y4*(0.25*xi - 0.25))*(0.25*x1*(
     &eta - 1.0) - 0.25*x2*(eta - 1.0) + 0.25*x3*(eta + 1.0) - 0
     &.25*x4*(eta + 1.0)) - 1.0*(x1*(0.25*xi - 0.25) - 1.0*x2*(0
     &.25*xi + 0.25) + x3*(0.25*xi + 0.25) - 1.0*x4*(0.25*xi - 0
     &.25))*(0.25*y1*(eta - 1.0) - 0.25*y2*(eta - 1.0) + 0.25*y3
     &*(eta + 1.0) - 0.25*y4*(eta + 1.0))
      dx_xi=0.25*x1*(eta - 1.0) - 0.25*x2*(eta - 1.0) + 0.25*x3*
     &(eta + 1.0) - 0.25*x4*(eta + 1.0)
      dx_eta=x1*(0.25*xi - 0.25) - 1.0*x2*(0.25*xi + 0.25) + x3*
     &(0.25*xi + 0.25) - 1.0*x4*(0.25*xi - 0.25)
      dy_xi=0.25*y1*(eta - 1.0) - 0.25*y2*(eta - 1.0) + 0.25*y3*
     &(eta + 1.0) - 0.25*y4*(eta + 1.0)
      dy_eta=y1*(0.25*xi - 0.25) - 1.0*y2*(0.25*xi + 0.25) + y3*
     &(0.25*xi + 0.25) - 1.0*y4*(0.25*xi - 0.25)
      dz_xi=0.25*z1*(eta - 1.0) - 0.25*z2*(eta - 1.0) + 0.25*z3*
     &(eta + 1.0) - 0.25*z4*(eta + 1.0)
      dz_eta=z1*(0.25*xi - 0.25) - 1.0*z2*(0.25*xi + 0.25) + z3*
     &(0.25*xi + 0.25) - 1.0*z4*(0.25*xi - 0.25)
      dphi_xi=(/dx_xi, dy_xi, dz_xi/)
      dphi_eta=(/dx_eta, dy_eta, dz_eta/)
      Vect_ne=(/Vect_ne_1, Vect_ne_2, Vect_ne_3/)
C
      v_N1_xi=S_mat(Kk,Kl)*dphi_xi(Kgamma)
      v_N1_eta=S_mat(Kk,Kl)*dphi_eta(Kgamma)
      pa=p1*(s(1)*Vect_ne(1)+s(2)*Vect_ne(2)+s(3)*Vect_ne(3))**2/
     &(Vect_ne(1)**2+Vect_ne(2)**2+Vect_ne(3)**2)
      v_NN1=pa*(0.25*XI_B*(ETA_B*eta + 1.0)*v_N1_eta-ETA_B*(0.25
     &*XI_B*xi + 0.25)*v_N1_xi)
C
      PHI1_xi=s(Kbeta)*dphi_xi(Kalpha)-s(Kalpha)*dphi_xi(Kbeta)
      PHI1_eta=s(Kbeta)*dphi_eta(Kalpha)-s(Kalpha)*dphi_eta(Kbeta)
      v_N2_xi=Vect_ne(Kk)*PHI1_xi
      v_N2_eta=Vect_ne(Kk)*PHI1_eta
      pb=2*p1*(s(1)*Vect_ne(1)+s(2)*Vect_ne(2)+s(3)*Vect_ne(3))/
     &(Vect_ne(1)**2+Vect_ne(2)**2+Vect_ne(3)**2)
      v_NN2=pb*(0.25*XI_B*(ETA_B*eta + 1.0)*v_N2_eta-ETA_B*(0.25
     &*XI_B*xi + 0.25)*v_N2_xi)
C
```

```
            PHI2_xi=2*(Vect_ne(Kbeta)*dphi_xi(Kalpha)
     &-Vect_ne(Kalpha)*dphi_xi(Kbeta))
            PHI2_eta=2*(Vect_ne(Kbeta)*dphi_eta(Kalpha)
     &-Vect_ne(Kalpha)*dphi_eta(Kbeta))
            v_N3_xi=Vect_ne(Kk)*PHI2_xi
            v_N3_eta=Vect_ne(Kk)*PHI2_eta
            pc=-p1*(s(1)*Vect_ne(1)+s(2)*Vect_ne(2)+s(3)*Vect_ne(3))**2/
     &(Vect_ne(1)**2+Vect_ne(2)**2+Vect_ne(3)**2)**2
            v_NN3=pc*(0.25*XI_B*(ETA_B*eta + 1.0)*v_N3_eta-ETA_B*(0.25
     &*XI_B*xi + 0.25)*v_N3_xi)
C
            v_NN=v_NN1+v_NN2+v_NN3
C
            rK=rK+W*(ETA_A*eta + 1.0)*(XI_A*xi/4.0 + 1.0/4.0)*v_NN
            END DO
          END DO
          AMATRX(K1,K2)=-4.0/9.0/Korder/Korder*rK
        END DO
       END DO
C
       RETURN
       END
```

D.2 Fortran Subroutine for Absorbent Surface

```
       SUBROUTINE UEL(RHS,AMATRX,SVARS,ENERGY,NDOFEL,NRHS,NSVARS,
     1 PROPS,NPROPS,COORDS,MCRD,NNODE,U,DU,V,A,JTYPE,TIME,DTIME,
     2 KSTEP,KINC,JELEM,PARAMS,NDLOAD,JDLTYP,ADLMAG,PREDEF,NPREDF,
     3 LFLAGS,MLVARX,DDLMAG,MDLOAD,PNEWDT,JPROPS,NJPROP,PERIOD)
C
       INCLUDE 'ABA_PARAM.INC'
       PARAMETER ( ZERO = 0.D0, HALF = 0.5D0, ONE = 1.D0 )
C
       DIMENSION RHS(MLVARX,*),AMATRX(NDOFEL,NDOFEL),PROPS(*),
     1 SVARS(*),ENERGY(8),COORDS(MCRD,NNODE),U(NDOFEL),
     2 DU(MLVARX,*),V(NDOFEL),A(NDOFEL),TIME(2),PARAMS(*),
     3 JDLTYP(MDLOAD,*),ADLMAG(MDLOAD,*),DDLMAG(MDLOAD,*),
     4 PREDEF(2,NPREDF,NNODE),LFLAGS(*),JPROPS(*),
     5 XI_I(4), Eta_I(4), s(3), ne(3), P_mat(2,6),
     6 Coord_mat(3,4), CW(2), WW(2,2),Vect_ne(3),
     7 S_mat(3,3), dphi_xi(3), dphi_eta(3)
C
       IF (LFLAGS(1)==1) THEN
         p2=PROPS(1)*TIME(1)
       ELSE IF (LFLAGS(1)==41.OR.LFLAGS(1)==47) THEN
```

```
        p2=PROPS(1)
      END IF
      s1=PROPS(2)
      s2=PROPS(3)
      s3=sqrt(1-s1*s1-s2*s2)
      s=(/ s1, s2, s3/)
C
      DO K1 = 1, NDOFEL
        DO KRHS = 1, NRHS
          RHS(K1,KRHS) = ZERO
        END DO
        DO K2 = 1, NDOFEL
          AMATRX(K2,K1) = ZERO
        END DO
      END DO
C
C Current Nodal Coordinates
      x1=COORDS(1,1)+U(1)
      y1=COORDS(2,1)+U(2)
      z1=COORDS(3,1)+U(3)
      x2=COORDS(1,2)+U(4)
      y2=COORDS(2,2)+U(5)
      z2=COORDS(3,2)+U(6)
      x3=COORDS(1,3)+U(7)
      y3=COORDS(2,3)+U(8)
      z3=COORDS(3,3)+U(9)
      x4=COORDS(1,4)+U(10)
      y4=COORDS(2,4)+U(11)
      z4=COORDS(3,4)+U(12)
C
      Xi_I=(/ -1, 1, 1, -1 /)
      Eta_I=(/ -1, -1, 1, 1 /)
      Coord_mat=reshape ( (/ x1, y1, z1, x2, y2, z2, x3, y3, z3, x4, y4,
     & z4 /), (/ 3, 4 /) )
      P_mat=reshape ( (/ 1, 2, 2, 1, 3, 3, 1, 2, 2, 1, 3, 3/),
     &(/ 2, 6 /) )
      S_mat=reshape ( (/ 0, -1, 1, 1, 0, -1, -1, 1, 0/),
     &(/ 3, 3 /) )
C Integration Constants
      Korder=10
      CW=(/ 4, 2 /)
      WW=reshape ( (/ 16, 8, 8, 4 /), (/ 2, 2 /) )
C
      IF (JELEM==50.AND.KSTEP==1.AND.KINC==1) THEN
        PRINT *,'Using SolarPressure.for'
      END IF
```

```
C
C Nodal Force
C
      DO K1=1,NDOFEL
        Ka=(K1-1)/3+1
        Kk=mod(K1-1,3)+1
        ETA_A=Eta_I(Ka)
        XI_A=Xi_I(Ka)
C
        rA=0
        DO KI=0,Korder
          DO KJ=0,Korder
            xi=-1+KI*2.0/Korder
            eta=-1+KJ*2.0/Korder
            IF ((KI==0.AND.KJ==0).OR.(KI==0.AND.KJ==Korder).OR.
     &(KI==Korder.AND.KJ==0).OR.(KI==Korder.AND.KJ==Korder)) THEN
              W=1
            ELSE IF (KI==0.OR.KI==Korder) THEN
              W=CW(mod(KJ-1,2)+1)
            ELSE IF (KJ==0.OR.KJ==Korder) THEN
              W=CW(mod(KI-1,2)+1)
            ELSE
              W=WW(mod(KI-1,2)+1,mod(KJ-1,2)+1)
            END IF
C Define vector Vect_n_e=(Vect_ne_1,Vect_ne_2,Vect_ne_3)
            Vect_ne_1=(z1*(0.25*xi - 0.25) - 1.0*z2*(0.25*xi + 0.25) +
     & z3*(0.25*xi + 0.25) - 1.0*z4*(0.25*xi - 0.25))*(0.25*y1*(
     &eta - 1.0) - 0.25*y2*(eta - 1.0) + 0.25*y3*(eta + 1.0) - 0
     &.25*y4*(eta + 1.0)) - 1.0*(y1*(0.25*xi - 0.25) - 1.0*y2*(0
     &.25*xi + 0.25) + y3*(0.25*xi + 0.25) - 1.0*y4*(0.25*xi - 0
     &.25))*(0.25*z1*(eta - 1.0) - 0.25*z2*(eta - 1.0) + 0.25*z3
     &*(eta + 1.0) - 0.25*z4*(eta + 1.0))
            Vect_ne_2=(x1*(0.25*xi - 0.25) - 1.0*x2*(0.25*xi + 0.25) +
     & x3*(0.25*xi + 0.25) - 1.0*x4*(0.25*xi - 0.25))*(0.25*z1*(
     &eta - 1.0) - 0.25*z2*(eta - 1.0) + 0.25*z3*(eta + 1.0) - 0
     &.25*z4*(eta + 1.0)) - 1.0*(z1*(0.25*xi - 0.25) - 1.0*z2*(0
     &.25*xi + 0.25) + z3*(0.25*xi + 0.25) - 1.0*z4*(0.25*xi - 0
     &.25))*(0.25*x1*(eta - 1.0) - 0.25*x2*(eta - 1.0) + 0.25*x3
     &*(eta + 1.0) - 0.25*x4*(eta + 1.0))
            Vect_ne_3=(y1*(0.25*xi - 0.25) - 1.0*y2*(0.25*xi + 0.25) +
     & y3*(0.25*xi + 0.25) - 1.0*y4*(0.25*xi - 0.25))*(0.25*x1*(
     &eta - 1.0) - 0.25*x2*(eta - 1.0) + 0.25*x3*(eta + 1.0) - 0
     &.25*x4*(eta + 1.0)) - 1.0*(x1*(0.25*xi - 0.25) - 1.0*x2*(0
     &.25*xi + 0.25) + x3*(0.25*xi + 0.25) - 1.0*x4*(0.25*xi - 0
     &.25))*(0.25*y1*(eta - 1.0) - 0.25*y2*(eta - 1.0) + 0.25*y3
     &*(eta + 1.0) - 0.25*y4*(eta + 1.0))
```

```
            Vect_ne=(/ Vect_ne_1, Vect_ne_2, Vect_ne_3/)
            rA=rA+W*(ETA_A*eta + 1.0)*((XI_A*xi)/4.0 + 0.25)*p2*(s(1)*
     &Vect_ne(1)+s(2)*Vect_ne(2)+s(3)*Vect_ne(3))*s(Kk)
          END DO
        END DO
        RHS(K1,1)=4.0/9.0/Korder/Korder*rA
       END DO
C
C Stiffness Sub-Matrix
C
       DO K1=1,NDOFEL
         DO K2=1,NDOFEL
           Ka=(K1-1)/3+1
           Kb=(K2-1)/3+1
           Kk=mod(K1-1,3)+1
           Kl=mod(K2-1,3)+1
           ETA_A=Eta_I(Ka)
           ETA_B=Eta_I(Kb)
           XI_A=Xi_I(Ka)
           XI_B=Xi_I(Kb)
           Kalpha=P_mat(1,Kl+1)
           Kbeta=P_mat(1,Kl+2)
           rK=0
           DO KI=0,Korder
             DO KJ=0,Korder
               xi=-1+KI*2.0/Korder
               eta=-1+KJ*2.0/Korder
               IF ((KI==0.AND.KJ==0).OR.(KI==0.AND.KJ==Korder).OR.
     &(KI==Korder.AND.KJ==0).OR.(KI==Korder.AND.KJ==Korder)) THEN
                 W=1
               ELSE IF (KI==0.OR.KI==Korder) THEN
                 W=CW(mod(KJ-1,2)+1)
               ELSE IF (KJ==0.OR.KJ==Korder) THEN
                 W=CW(mod(KI-1,2)+1)
               ELSE
                 W=WW(mod(KI-1,2)+1,mod(KJ-1,2)+1)
               END IF
              Vect_ne_1=(z1*(0.25*xi - 0.25) - 1.0*z2*(0.25*xi + 0.25) +
     & z3*(0.25*xi + 0.25) - 1.0*z4*(0.25*xi - 0.25))*(0.25*y1*(
     &eta - 1.0) - 0.25*y2*(eta - 1.0) + 0.25*y3*(eta + 1.0) - 0
     &.25*y4*(eta + 1.0)) - 1.0*(y1*(0.25*xi - 0.25) - 1.0*y2*(0
     &.25*xi + 0.25) + y3*(0.25*xi + 0.25) - 1.0*y4*(0.25*xi - 0
     &.25))*(0.25*z1*(eta - 1.0) - 0.25*z2*(eta - 1.0) + 0.25*z3
     &*(eta + 1.0) - 0.25*z4*(eta + 1.0))
              Vect_ne_2=(x1*(0.25*xi - 0.25) - 1.0*x2*(0.25*xi + 0.25) +
     & x3*(0.25*xi + 0.25) - 1.0*x4*(0.25*xi - 0.25))*(0.25*z1*(
```

```
     &eta - 1.0) - 0.25*z2*(eta - 1.0) + 0.25*z3*(eta + 1.0) - 0
     &.25*z4*(eta + 1.0)) - 1.0*(z1*(0.25*xi - 0.25) - 1.0*z2*(0
     &.25*xi + 0.25) + z3*(0.25*xi + 0.25) - 1.0*z4*(0.25*xi - 0
     &.25))*(0.25*x1*(eta - 1.0) - 0.25*x2*(eta - 1.0) + 0.25*x3
     &*(eta + 1.0) - 0.25*x4*(eta + 1.0))
            Vect_ne_3=(y1*(0.25*xi - 0.25) - 1.0*y2*(0.25*xi + 0.25) +
     & y3*(0.25*xi + 0.25) - 1.0*y4*(0.25*xi - 0.25))*(0.25*x1*(
     &eta - 1.0) - 0.25*x2*(eta - 1.0) + 0.25*x3*(eta + 1.0) - 0
     &.25*x4*(eta + 1.0)) - 1.0*(x1*(0.25*xi - 0.25) - 1.0*x2*(0
     &.25*xi + 0.25) + x3*(0.25*xi + 0.25) - 1.0*x4*(0.25*xi - 0
     &.25))*(0.25*y1*(eta - 1.0) - 0.25*y2*(eta - 1.0) + 0.25*y3
     &*(eta + 1.0) - 0.25*y4*(eta + 1.0))
            dx_xi=0.25*x1*(eta - 1.0) - 0.25*x2*(eta - 1.0) + 0.25*x3*
     &(eta + 1.0) - 0.25*x4*(eta + 1.0)
            dx_eta=x1*(0.25*xi - 0.25) - 1.0*x2*(0.25*xi + 0.25) + x3*
     &(0.25*xi + 0.25) - 1.0*x4*(0.25*xi - 0.25)
            dy_xi=0.25*y1*(eta - 1.0) - 0.25*y2*(eta - 1.0) + 0.25*y3*
     &(eta + 1.0) - 0.25*y4*(eta + 1.0)
            dy_eta=y1*(0.25*xi - 0.25) - 1.0*y2*(0.25*xi + 0.25) + y3*
     &(0.25*xi + 0.25) - 1.0*y4*(0.25*xi - 0.25)
            dz_xi=0.25*z1*(eta - 1.0) - 0.25*z2*(eta - 1.0) + 0.25*z3*
     &(eta + 1.0) - 0.25*z4*(eta + 1.0)
            dz_eta=z1*(0.25*xi - 0.25) - 1.0*z2*(0.25*xi + 0.25) + z3*
     &(0.25*xi + 0.25) - 1.0*z4*(0.25*xi - 0.25)
            dphi_xi=(/dx_xi, dy_xi, dz_xi/)
            dphi_eta=(/dx_eta, dy_eta, dz_eta/)
            Vect_ne=(/Vect_ne_1, Vect_ne_2, Vect_ne_3/)
C
            PHI1_xi=s(Kbeta)*dphi_xi(Kalpha)-s(Kalpha)*dphi_xi(Kbeta)
            PHI1_eta=s(Kbeta)*dphi_eta(Kalpha)-s(Kalpha)*dphi_eta(Kbeta)
            v_N4_xi=s(Kk)*PHI1_xi
            v_N4_eta=s(Kk)*PHI1_eta
            v_NN4=p2*(0.25*XI_B*(ETA_B*eta + 1.0)*v_N4_eta-ETA_B*(0.25
     &*XI_B*xi + 0.25)*v_N4_xi)
C
            v_NN=v_NN4
C
            rK=rK+W*(ETA_A*eta + 1.0)*(XI_A*xi/4.0 + 1.0/4.0)*v_NN
            END DO
          END DO
          AMATRX(K1,K2)=-4.0/9.0/Korder/Korder*rK
        END DO
       END DO
C
       RETURN
       END
```

D.3 Generic Input File

The option sim=NO in the frequency step does not provide accurate results. It is important to remove this option in the input file.

```
*Heading
** Job name: Plate_SP Model name: Model-1
** Generated by: Abaqus/CAE 2016
*Preprint, echo=NO, model=NO, history=NO, contact=NO
**
** PARTS
**
*Part, name=Load_Elements
*Node
      1,       0.1061,       0.1061,           0.
...
   2601,      -0.1061,      -0.1061,           0.
*USER ELEMENT, NODES=4, UNSYMM, TYPE=U1, I PROPERTIES=0,PROPERTIES=3
1, 2, 3
*Element, type=U1
   1,    1,    2,   53,   52
...
2500, 2549, 2550, 2601, 2600
*Nset, nset=Set-4, generate
    1,  2601,     1
*Elset, elset=Set-4, generate
    1,  2500,     1
**
*UEL PROPERTY, ELSET=Set-4
-50.0, 0.7071, 0.0
*End Part
**
*Part, name=Mechanical_Elements
*Node
      1,      -0.1061,      -0.1061,  9.99999975e-05
...
   5202,       0.1061,       0.1061,           0.
*Element, type=SC8R
   1,  154,  155,   53,   52,  103,  104,    2,    1
...
2500, 5201, 5202, 5100, 5099, 5150, 5151, 5049, 5048
*Nset, nset=Set-3, generate
    1,  5202,     1
*Elset, elset=Set-3, generate
    1,  2500,     1
** Section: Section-1
*Shell Section, elset=Set-3, material=Kapton
```

```
0.0001, 5
*End Part
**
**
** ASSEMBLY
**
*Assembly, name=Assembly
**
*Instance, name=Mechanical_1, part=Mechanical_Elements
          0.,           0.,      -0.0001
*End Instance
**
*Instance, name=Load-1, part=Load_Elements
*End Instance
**
*Nset, nset=Set-1, instance=Mechanical_1
    1,    2,    3,    4,    5,    6,    7,    8,    9,   10,   11,   12,   13,   14,   15,   16
...
 5187, 5188, 5189, 5190, 5191, 5192, 5193, 5194, 5195, 5196, 5197, 5198, 5199, 5200, 5201, 5202
*Elset, elset=Set-1, instance=Mechanical_1
    1,    2,    3,    4,    5,    6,    7,    8,    9,   10,   11,   12,   13,   14,   15,   16
...
 2497, 2498, 2499, 2500
*Nset, nset=m_Set-3, instance=Mechanical_1
    1,    2,    3,    4,    5,    6,    7,    8,    9,   10,   11,   12,   13,   14,   15,   16
...
 5143, 5144, 5145, 5146, 5147, 5148, 5149, 5150, 5151
*Elset, elset=m_Set-3, instance=Mechanical_1, generate
    1,  2500,     1
*Nset, nset=s_Set-3, instance=Load-1, generate
    1,  2601,     1
*Elset, elset=s_Set-3, instance=Load-1, generate
    1,  2500,     1
*Surface, type=NODE, name=m_Set-3_CNS_, internal
m_Set-3, 1.
*Surface, type=NODE, name=s_Set-3_CNS_, internal
s_Set-3, 1.
** Constraint: Constraint-1
*Tie, name=Constraint-1, adjust=no, no rotation, no thickness
s_Set-3_CNS_, m_Set-3_CNS_
*End Assembly
**
** MATERIALS
**
*Material, name=Kapton
*Density
```

```
1420.,
*Elastic
 2.5e+09, 0.34
** ----------------------------------------------------------------
**
** STEP: Spin
**
*Step, name=Spin, nlgeom=YES
*Static
1., 1., 1e-05, 1.
**
** BOUNDARY CONDITIONS
**
** Name: BC-1 Type: Symmetry/Antisymmetry/Encastre
*Boundary
Set-1, ENCASTRE
**
** LOADS
**
** Name: Centrifugal   Type: Rotational body force
*Dload
Mechanical_1.Set-3, CENTRIF, 2741.56,0.,0.,0.,0.,0.,1.
**
** OUTPUT REQUESTS
**
*Restart, write, frequency=0
**
** FIELD OUTPUT: F-Output-3
**
*Output, field, variable=PRESELECT
**
** HISTORY OUTPUT: H-Output-1
**
*Output, history, variable=PRESELECT
*End Step
** ----------------------------------------------------------------
**
** STEP: Frequency
**
*Step, name=Frequency, nlgeom=NO, perturbation
*Frequency, eigensolver=Lanczos, acoustic coupling=on, normalization=displacement
50, , , , ,
**
** OUTPUT REQUESTS
**
*Restart, write, frequency=0
```

```
**
** FIELD OUTPUT: F-Output-1
**
*Output, field, variable=PRESELECT
*End Step
** ----------------------------------------------------------------
**
** STEP: ComplexFrequency
**
*Step, name=ComplexFrequency, nlgeom=NO, perturbation, unsymm=YES
*Complex Frequency, friction damping=NO
10, , ,
**
** OUTPUT REQUESTS
**
**
** FIELD OUTPUT: F-Output-2
**
*Output, field, variable=PRESELECT
*End Step
```